NTNU

Norwegian University of
Science and Technology

Spatial Variation in the Overburden R Factor at the Ekofisk Field from 4D Seismic Analysis and Geomechanical Modelling

Marie Wik Skadberg

Petroleum Geoscience and Engineering
Submission date: June 2017
Supervisor: Kenneth Duffaut, IGP
Co-supervisor: Martin Landrø, IGP

Norwegian University of Science and Technology
Department of Geoscience and Petroleum

Abstract

4D seismic analysis of the overburden is essential in well planning and risk analysis. The dilation factor (R) links the changes in velocities and thicknesses causing time shifts. The focus of this thesis has been determination of both vertical and lateral variation in the overburden R factor across the Ekofisk Field in the North Sea. The R factor has been studied above depleting and repressurized regions using 4D seismic data from 2011 to 2014 and 1D geomechanical modelling.

Superposition of Geertsma's nucleus of strain model proved to simulate the displacement changes in the overburden of depleted regions, but not repressurized regions. Synthetic time shifts were generated from the geomechanical model and further compared with observed time shifts to establish the depth-dependent R factor. This revealed a strong vertical variation in the R factor in the depleting zone, with values decreasing with depth from about $R = 14$ in the shallow overburden ($\approx 750m$) towards $R = 2$ at the top reservoir ($\approx 3000m$). The depth-dependency of R appears robust from evaluation of alternative models for overburden strain.

In addition to the vertical change in the R factor, a clear lateral variation was observed. A constant R factor in the vertical direction was assumed, and the focus was on the contrasts in R between depleted and repressurized regions. Two approaches estimated the R factor based on 4D; one using only the time shifts at top reservoir, the other using the depth-dependent time shift. The total overburden thickness change was implemented to confirm the results from both methods. This was estimated from reservoir compaction and sea floor subsidence from bathymetry data. The results from the approaches were consistent; R was larger in the overburden above the injection zones, where R was 4 to 8, while between $2 - 3$ in the depletion zone. The magnitude of R in the injection zones corresponded to the level of repressurization. The lateral variation is believed to be caused by localized reservoir compaction at the Ekofisk Field, which is triggered by production-induced activity across the field.

Production-induced changes in velocities and vertical thicknesses were calculated from 4D time shifts using both constant and depth-dependent R factor. The estimation of thickness change was very sensitive to which R factor was applied, but it was insignificant when estimating velocity change.

Sammendrag

Seismisk 4D analyse av overburden er et grunnleggende verktøy i brønnplanlegging og risikoanalyse. Dilasjonsfaktoren (R) skiller mellom 4D tidsskift som skyldes endringer i hastigheter og tykkelse. Hovedmålene i denne oppgaven har vært å estimere vertikal og horisontal variasjon i overburden R faktor på Ekofiskfeltet i Nordsjøen. R har blitt undersøkt i områder som gjennomgår depletering og injeksjon ved bruk av 4D seismikk fra 2011 til 2014 og 1D geomekanisk modellering.

Superposisjonering av Geertsma's forenklede modell ble brukt for å simulere overburden over depleteringsområdene, men dette var ikke tilstrekkelig over injeksjonsområdene. Syntetiske tidsskift ble generert fra den geomekaniske modellen og sammenlignet med de observerte tidsskiftene for å etablere den dybde-avhengige R faktoren. Dette avslørte en sterk variasjon i R over depleteringsområdene, hvor verdiene minket i dybde fra rundt $R = 14$ i grunne deler av overburden ($\approx 750m$) til $R = 2$ på toppen av reservoaret ($\approx 3000m$). Dybdeavhengigheten virker robust når alternative modeller for tøyninger i overburden har blitt studert.

I tillegg til den vertikale variasjonen i R, ble det også observert en tydelig lateral variasjon. Her ble en konstant R i vertikal retning antatt, og fokuset var på kontraster mellom depleterte og trykkoppbyggede områder. To metoder er brukt for å estimere R med utgangspunkt i 4D; en bruker kun tidsskiftet på top reservoar, mens den andre bruker tidsskiftskurven i dyp. Begge metodene var begrenset av den totale tykkelsesendringen av overburden, som ble estimert fra reservoarkompaksjon og nedsynkning av havbunnen. Sistnevnte er etablert fra bathymetry data. Resultatene fra metodene er samsvarende i at R er større over injeksjonssområder ($R = 4 - 8$) enn depleteringsområder ($R = 2 - 3$). Verdien på R over injeksjonsområdene korrelerer med nivået på trykkoppbygningen i disse regionene. Den laterale variasjonen i R er sannsynligvis forårsaket av lokalisert reservoarkompaksjon på Ekofiskfeltet, noe som skyldes produksjonsindusert aktivitet på feltet.

Produksjons-induserte endringer i hastighet og tykkelse ble estimert fra 4D tidsskift ved å bruke både konstant og dybde-avhengig R faktor. Estimatene for tykkelsesendring fra 4D tidsskift var svært sensitive til bruk av konstant eller dybdeavhengig R, men for beregning av hastighetsendringer var det vilkårlig.

Acknowledgements

First and foremost, I would like to thank my dedicated supervisor Kenneth Duffaut at NTNU. Furthermore, I am very thankful for my brilliant supervisor at ConocoPhillips Norway; Sirikarn Narongsirikul, whom I have stolen plenty of time and advice from. I would like to thank ConocoPhillips Norway for data access and a good collaboration during my Master's Thesis. Especially Per Gunnar Folstad and Tim Austin for arranging the cooperation, and for fruitful discussions when facing new problems. I want to acknowledge SINTEF Petroleum AS, Formation Physics Laboratory for core data and discussion, and NPD for well data access. Andreas Bauer at SINTEF and Martin Landrø at NTNU; for important input. I also send my gratitude to Rune Holt at NTNU, who selflessly shares his extensive knowledge to discuss results and/or crazy theories.

Thank you to my family and friends, especially my parents and siblings, for encouragement and support. A special thanks to Simon.

The long days and hard work on this Master's Thesis have been motivated by my great fellow students at NTNU and the excellent people at ConocoPhillips Norway.

Table of Contents

List of Tables

List of Figures

Chapter 1

Introduction

1.1 Background

Seismic time-lapse data (4D) has been a fundamental tool in reservoir monitoring on the Norwegian Continental Shelf the last two decades. 4D seismic was analyzed at the Gullfaks field in order to detect undrained oil pockets already in 1995, (Landrø, 2010). The fourth dimension in 4D refers to calendar time; as usually two or three seismic surveys are repeated over time. Production-related changes in and around the reservoir can be recognized from studying the differences in reflectivity and/or traveltime between these seismic surveys. The cumulative change in two-way traveltime is referred to as a time shift. 4D has opened for new possibilities to study effects of fluid saturation in the reservoir from seismic data, (Landrø and Strønen, 2003), and to optimize well placement, (Byerley et al., 2006). It is a well established tool for understanding the reservoir, but monitoring the overburden of depleting reservoirs using 4D is more in focus than ever. There are several reasons for this. Although no fluid substitution is believed to take place in the overburden, time shifts can be used to recognize out-of-zone injection, fluid leakage, compaction, expansion and stress changes. The latter may lead to well collapses and faulting or fault reactivation, (Barkved et al., 2003). In other words; no changes in amplitude are expected in the overburden, but differences in traveltime can be caused by geomechanical changes. Later studies also imply that 4D data in the overburden can be inverted to reveal changes in effective pressure in the reservoir (Garcia and MacBeth, 2013). Moreover, that overburden time shifts might be interpreted and applied in field management similar to ”conventional” 4D. This is especially relevant in chalk fields, where the 4D interpretation within the reservoir is complicated

by compaction from both chemical reactions and pressure changes, (Kenter et al., 2004; Røste and Ke, 2017).

Production of hydrocarbons leads to changes in pore pressure, which induce stress changes in and around the reservoir. This causes compaction of the reservoir and corresponding expansion of the overburden and change in velocities, (Geertsma, 1973). All reservoirs undergoing a pressure depletion are expected to compact to a certain degree, (Røste et al., 2015). An essential problem in quantitative 4D analysis has been to separate the effects from changes in thickness and velocities in production-induced time shifts, (Landrø and Stammeijer, 2004). Recognizing the induced magnitude of changes in velocity and thicknesses is important in understanding overburden and performing well planning and risk analysis. Additionally, it is necessary to accurately depth-convert seismic data and thereby establish compaction of the reservoir, (Guilbot and Smith, 2002). To solve this, the R factor has been introduced by (Hatchell and Bourne, 2005) and (Røste et al., 2005). (Hatchell and Bourne, 2005) found a linear relationship between changes in relative thicknesses and velocities by comparing 4D data with geomechanical models from several fields worldwide. The dimensionless parameter correlating relative changes in velocity and thickness was introduced as the R factor. Simultaneously, (Røste et al., 2005) introduced the dilation factor α by studying offset-dependent time shifts. It was originally introduced as a parameter dependent on rock properties, but had the exact same definition as presented in (Hatchell and Bourne, 2005), excluding a minus sign; $R = -\alpha$.

The R factor is an exceptionally useful parameter as it allows for determination of changes in velocity and thickness from 4D. Therefore it has been the focus of numerous studies since it was first proposed, see Table 1.1. It has usually been referred to as R or the R factor, which will be the convention throughout this report as well. Safe to say the resulting information on R is diverged. Data from 4D seismic, theoretical rock-physics models and laboratory experiments have all been implemented in order to determine the value and nature of R. Thus, it has proven to depend strongly on lithology, stress level and stress path, (Holt et al., 2008, 2016). In practice this means that R might vary both laterally and with depth in and around the reservoir. Inspired by (Bathija et al., 2009), a table demonstrating measured R values in different publications is given in Table 1.1 below. This table only includes estimates for shale, as the majority of the data studied in this project (namely overburden) is shale. From previous publications utilizing 4D data, the overburden R factor appears to be smaller at chalk fields (Valhall, Ekofisk) than at

sandstone reservoirs (Snorre, Heidrun, Statfjord), see Table 1.1.

Despite all the parameters affecting the R factor; the assumption of a constant R factor for the overburden is commonly embraced. It is generally accepted that by assuming a constant R for the overburden, the error in the calculation of velocity and thickness changes is negligible in practice, (Carcione et al., 2007; Bathija et al., 2009). Yet, a strongly depth-dependent R was required to match compaction data at the HP/HT reservoir Elgin in the North Sea. R proved to be very large and layer-dependent, (Hawkins, 2008). At the Snorre, Heidrun and Statfjord fields, the depth-dependent trend in R was recently established using geomechanical modelling and 4D seismic, (Røste and Ke, 2017). R was estimated to reach 100 in the shallow part, yet an average $R = 15$ seemed appropriate for the overburden, implying a strong variation in depth. The depth-dependency was proposed to correlate with lithological layers. There has been few estimations of the lateral variation of R in the overburden of a producing field. (Røste and Ke, 2017) found the lateral variation to be small at the Snorre, Heidrun and Stafjord fields. On the other hand, laboratory experiments estimate that stress path and the corresponding R changes strongly around the field, (Holt et al., 2016).

Table 1.1: Estimated R factors for shale from different publications, inspired by (Bathija et al., 2009). *Loading, in situ stress, **Unloading, in situ stress,***Constant mean stress path (depletion), ****Hydrostatic loading.

$\|\mathbf{R}\|$	**Method**	**Publication**
4 - 6	4D seismic (multiple fields)	(Hatchell and Bourne, 2005)
2.6	4D seismic (Valhall Field)	(Røste et al., 2005)
4 - 6	4D seismic (Ekofisk Field)	(Janssen et al., 2006)
4.4 - 5.4	Rock physics model (Asperity-deformation model)	(Carcione et al., 2007)
2 - 2.3	Rock physics model (Hertz-Mindlin model)	(Carcione et al., 2007)
6*, 13**	Ultastronic lab experiment	(Holt et al., 2008)
6.3 - 10.6	Ultrasonic lab experiment	(Bathija et al., 2009)
1.5-1.8***, 6-7****	Ultrasonic lab experiment	(Holt et al., 2009)
20	4D seismic (Snorre Field)	(Røste et al., 2015)
15	4D seismic (Snorre, Heidrun and Statfjord Fields)	(Røste and Ke, 2017)

1.2 Main Objectives

The main objectives of this thesis are the following;

i) Estimate the vertical variation in the R factor in parts of the overburden of the Ekofisk Field.

ii) Estimate the lateral variation in the constant R factor in the overburden of the Ekofisk Field, with special focus on contrasts between depleted and repressurized regions. A constant R in this report refers to a fixed R in the vertical direction.

iii) Understand the consequences of ignoring the depth-dependency of R and applying a constant R in the estimation of changes in velocities and thicknesses from 4D time shifts.

More specifically, it is a goal to provide a general overview of the R factor trend in the overburden of the Ekofisk Field, and provide insight to whether it is important to use the depth-dependent trend when estimating changes in thickness and velocity from 4D data. Understanding the vertical variation in R at the Ekofisk Field is motivated by an intention of improving field management by coupling geomechanical modelling and 4D. From a suitable R factor model it should in principal be possible to acquire reservoir compaction from 4D data. Additionally, areas with large stress and strain changes would be clear and consequently avoided during well planning. Data from the overburden of depleting zones and injection regions at the Ekofisk Field are studied in order to get an insight to the lateral variation in R. It is of importance to establish upper and lower limits of appropriate R factors at the Ekofisk Field, which will simplify the application of R to 4D data. Moreover, this will contribute to explain the complex effects taking place in the overburden of repressurization zones.

1.3 Approach

The approach of the thesis has been to study 4D seismic data from 2011 to 2014 from the Ekofisk Field and estimate strain from geomechanical modelling using Geertsma's nucleus of strain model. Three focus areas undergoing various degrees of injection and depletion are studied, and the time shift in depth is averaged between six to seven 4D seismic traces in these regions. Time strain is estimated from the time shifts to understand which parts of the overburden have been experiencing a slow-down or speed-up between 2011 and 2014. The displacement is modelled from Geertsma's nucleus of strain model in a grid in MATLAB, where each point represents a certain depth and distance in the overburden. Strain is estimated from the displacement. Sea floor subsidence and reservoir compaction, the latter from ConocoPhillips' reservoir model, are used as inputs alongside pore pressure depletion to reassure realistic simulations of strain distribution from Geertsma's nucleus of strain model. The overburden is complex, where effects from several sources intervene. In pursuance of a realistic model for strain, the geomechanical effects from three bordering reservoirs were simulated using the superposition principle of the displacement fields. Synthetic time shifts are estimated by using the modelled strain from Geertsma's nucleus of strain model. The synthetic time shifts are compared to the observed time shifts to estimate a suitable R in each interval, in other words a depth-dependent R. The constant R factor is estimated from two approaches. Both are based on the total thickness change of the overburden, which is estimated from sea floor subsidence from bathymetry data and reservoir compaction. One calculation uses the time shift at top reservoir, while the other method studies the time shift curve in depth. The resulting R is compared for both methods in depletion and repressurization zones to determine the lateral variation in R. An equation relating compaction at top reservoir and constant R is expressed, and applied to understand the how R varies laterally.

1.4 Structure of Thesis

The thesis is structured as follows;

- Chapter 2: description of the Ekofisk Field.
- Chapter 3: introduction to the theory necessary to employ the applied methodology and discuss the observations.
- Chapter 4: explanation of the methodology, including how data was obtained and flow charts clarifying each approach. The focus areas are introduced. Additionally, the input parameters in the geomechanical model is established and the field observations used to constrain the results from the simulations are presented.
- Chapter 5: presentation of the results of this study. Firstly, the time shift and time strain curve in depth are established. Secondly, the estimated subsidence of the sea floor is presented. The simulation from the geomechanical model is given, which is further used to estimate synthetic time shifts. The depth-dependent R is estimated from the latter. The constant R factor above the focus areas is presented and plots of R as a function of reservoir compaction above depletion zones and repressurized regions are given.
- Chapter 6: discussion of the results given in Chapter 5. An analysis of the nature of the R factor is conferred; what factors dominate R and is the estimation of the constant/depth-dependent trend trivial. The assumptions in the approach are critically viewed, with special focus on the limitations of the geomechanical model.
- Chapter 7: conclusion of the main observations.
- Chapter 8: suggestions to further work on this topic.

Chapter 2

Study Area

The data studied in this report is from the Ekofisk Field. The field was discovered in 1969, and is one of the largest oil discoveries on the Norwegian Continental Shelf. Waterflooding was successfully initiated in 1979 after oil production peaked in 1976, (Hermansen et al., 1997). Waterflooding is used efficiently to increase pore pressure and enhance the recovery factor of the field. The field is operated by ConocoPhillips and is located in the southern part of the North Sea, as marked in Figure 2.1. The field is suffering from high rates of sea floor subsidence; the maximum subsidence of the sea floor in the center of the field is close to 10 m since production started in 1971 to 2017. The compaction of top reservoir was estimated from 4D seismic and found to be up to 6 m between 1989 and 1999, (Guilbot and Smith, 2002). The producing formations are the Ekofisk and Tor formations, both soft chalk, (Sulak et al., 1991). The reservoir is an elongated anticline with the major axis going North-South covering around $48.56km^2$, (Hermansen et al., 1997). The top reservoir varies from 2895 m true vertical depth subsea (TVDSS) along the crest of the structure to around 3108 m TVDSS along the flanks, (Nagel, 1998). Top reservoir is the top of the Ekofisk formation, which is from the Paleocene period and is of Danian Age. The Tor formation underlies the Ekofisk formation and is of Maastrichtian Age in the Cretaceous period. In certain areas of the Ekofisk Field there is an impermeable barrier between the Ekofisk and Tor formation, referred to as the Ekofisk Tight Zone. An overall pay thickness larger than 300 m is common, (Sulak et al., 1991). The porosity of the reservoir is estimated to be high, see Table 2.1 below, but varies laterally and vertically. The effective permeability is increased because of natural fractures.

This project has focused more specifically on data from a small region undergoing a large

Table 2.1: Previous publications on porosity and permeability from the Ekofisk Field.

Porosity range	Effective permeability due to natural fractures, [mD]	Publication
0.25 - 0.48	<100	(Sulak et al., 1991)
0.30 - 0.48	Not given	(Hermansen et al., 1997)
0.30 - 0.45	<150	(Nagel, 1998)

pore pressure depletion, and two bordering regions being repressurized by injectors, see Figure 4.1. The depleting zone is one of the top producing regions of the Ekofisk Field, leading to high compaction rates and corresponding complications in the overburden related to stress and strain. Reservoir compaction and surface subsidence has previously lead to casing deformation, (Schwall et al., 1994). As a consequence, this region is of special interest. Moreover, several wells have recently collapsed in the overburden above the region leading to an increased interest in the overburden of the surrounding regions as well.

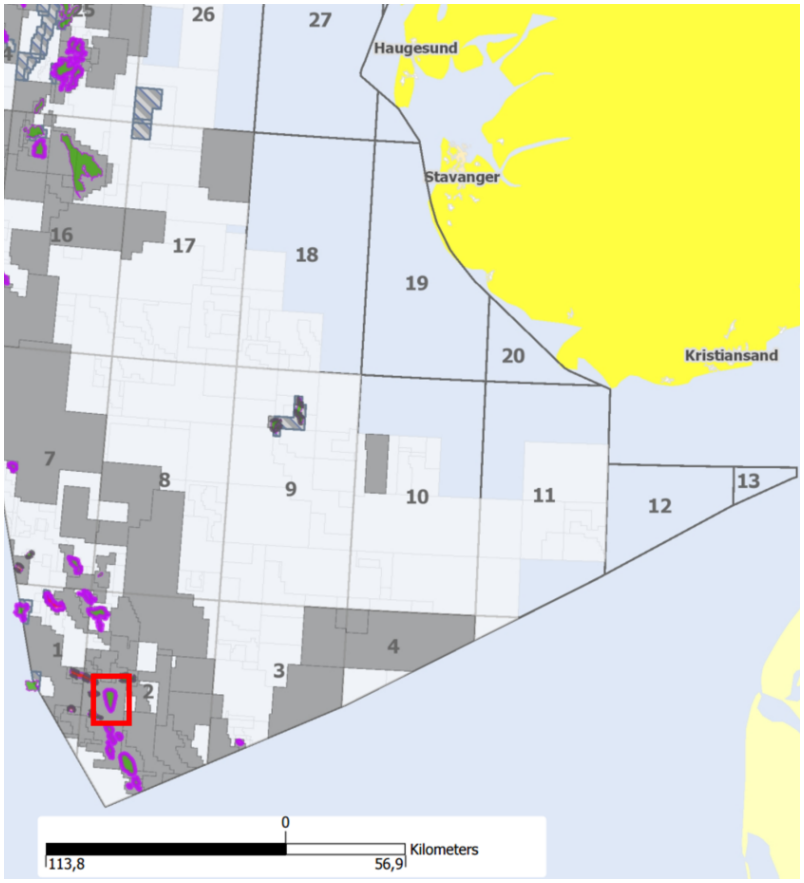

Figure 2.1: Map displaying the location of the Ekofisk Field; green mark with purple line within the red square, from factpages.npd.no.

Chapter 3

Theory

3.1 4D Seismic

4D seismic reveals changes in amplitude and traveltime between two or more seismic surveys. The seismic surveys studied in the 4D analysis are referred to as base and monitor. Time shifts (Δt) are differences in two-way traveltime (t) between the surveys, that is;

$$\Delta t = t_{monitor} - t_{base} \tag{3.1}$$

This implies that a longer traveltime in the monitor survey will give a positive time shift. However, base and monitor may be switched based on preference, therefore it is common to refer to 4D data with reference to ”speed-up” and ”slow-down”. The former implies that the traveltime has decreased between the two surveys, while the latter indicates that traveltime has increased. Case studies on 4D seismic implies that the method is robust with respect to noise, and that even old base surveys can be studied to gain valuable information, (Landrø et al., 1999). Within the reservoir, changes in amplitude are often related to fluid substitution, consequently 4D may be used to identify oil pockets, study water injection patterns or monitor injection of CO_2, (Arts et al., 2004). But as mentioned in Section 1.1; no amplitude differences are expected in the overburden as no fluid substitution is believed to take place. As a result, the criterion for examining 4D seismic in the overburden is a difference in traveltime between two seismic surveys. Two-way traveltime is a function of distance (x) and p-wave velocity (v_p), that is;

$$t = \frac{2x}{v_p} \tag{3.2}$$

In 4D analysis the distance refers to layer thickness (z). Thus, a shift in seismic traveltime is either caused by change in velocity (Δv_p) or thickness (Δz), and the observed time shifts are usually induced by both effects. In general, production-induced velocity changes implies changes in stress, pore pressure or fluid saturation, while a change in thickness indicates a stretch or compaction, (Røste et al., 2015). By partial differentiation of equation 3.2, one might separate the effects on time shift caused by changes in thickness and velocity within a layer, (Landrø and Stammeijer, 2004);

$$\left(\frac{\Delta t}{t} \approx \frac{\Delta z}{z} - \frac{\Delta v_p}{v_p} \right)_{layer} \tag{3.3}$$

Equation 3.3 implies that the normalized time shift ($\frac{\Delta t}{t}$) within a layer is approximated by a simple summation of relative change in thickness ($\frac{\Delta z}{z}$) and velocity ($\frac{\Delta v_p}{v_p}$). If an investigated section is divided into N layers, equation 3.3 can be applied to each layer i. It is assumed that the velocity in the layer, $v_{p,i}$ is constant laterally and in depth. For this assumption to be acceptable in practice, the layers have to be quite small.

Figure 3.1 demonstrates how equation 3.3 is applied to a layer. t_1, D_1, t_2 and D_2 represent traveltimes and depths to top horizon and base horizon for the layer in the first survey, respectively. t_1', D_1', t_2' and D_2' represent traveltimes and depths to top horizon and base horizon in the second survey, respectively. Δt_1 and Δt_2 are time shift at top and base horizon. $t_{int,i}$ is the two-way traveltime in this single interval (i) at first survey, and with reference to Figure 3.1 it is given as;

$$t_{int,i} = t_2 - t_1 \tag{3.4}$$

The interval time shift for the layer ($\Delta t_{int,i}$) is calculated from the time shifts at top and base horizon. Thus, the interval time shift is the change in traveltime for this specific layer:

$$\Delta t_{int,i} = \Delta t_2 - \Delta t_1 \tag{3.5}$$

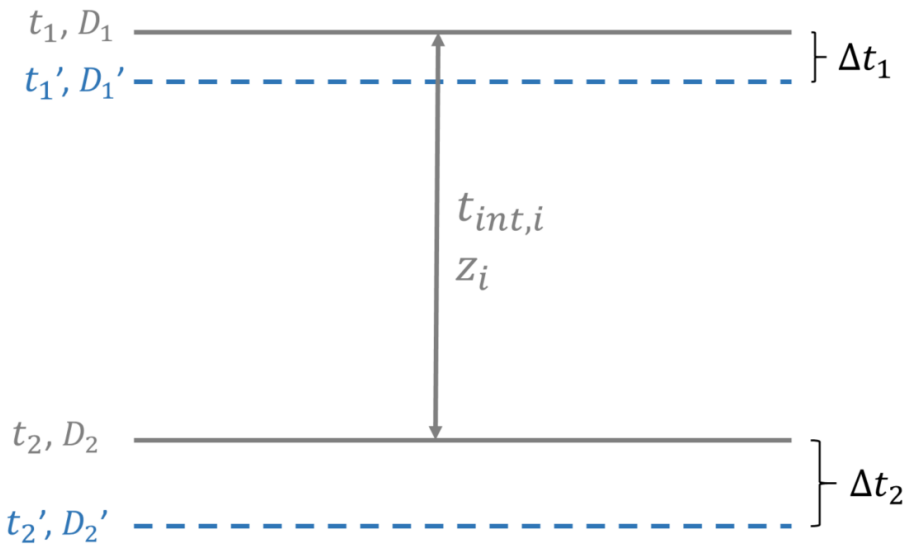

Figure 3.1: Sketch of a layer where equation 3.3 is applied. Solid grey lines are top and base horizon at first survey, dotted blue lines are top and base horizon at second survey. Δt_1 and Δt_2 are time shift at top and base horizon. $t_{int,i}$ is the two-way traveltime within the layer at first survey.

The change in thickness for the layer (Δz_i) is;

$$\Delta z_i = (D_2' - D_1') - (D_2 - D_1) \tag{3.6}$$

This implies that Δz_i is positive when the overburden is stretching, which normally happens as the reservoir is depleting. The most common convention in geomechanics is to have compressive strength and strain positive, (Davis and Selvadurai, 2005). However, in this case strain is expressed as the fractional change in layer thickness and will be positive when the layer is increasing in thickness. Vertical strain ($\varepsilon_{z,i}$) in the layer is expressed from the thickness change with respect to the original layer thickness during the base survey (z_i), that is;

$$\varepsilon_{z,i} = \frac{\Delta z_i}{D_2 - D_1} = \frac{\Delta z_i}{z_i} \tag{3.7}$$

It is important to understand that time shifts are cumulative. Consequently, time shifts observed at a certain depth might be caused by events much shallower. To gain more details on the time shifts one should study time strains. Time strains represent the change in traveltime and are estimated by differentiating time shifts with respect to traveltime, (Røste et al., 2015). The time strain can numerically be estimated from;

$$\frac{d(\Delta t)}{dt} \approx \frac{\Delta t_2 - \Delta t_1}{t} \tag{3.8}$$

For many reservoirs where compaction is limited, e. g. sandstone reservoirs, strains in the overburden are so small that they are assumed to have negligible influence on the time shift. Time strains are then related directly to changes in velocities, which may be compared to a geomechanical model to validate both the time shifts and the model, (Røste et al., 2015), (Røste and Ke, 2017). However, the strain cannot be neglected when the thickness change of the overburden is significant.

3.2 The R Factor

The R factor implies that fractional changes in velocities are proportional to fractional changes in path length. It is an empirical parameter that demonstrates the sensitivity of the rock with respect to vertical strain, (Røste and Ke, 2017). It is defined as, (Hatchell and Bourne, 2005; Røste et al., 2005);

$$R = -\frac{\frac{\Delta v_p}{v_p}}{\frac{\Delta z}{z}} \tag{3.9}$$

An important observation is that $\frac{\Delta z}{z}$ in equation 3.9 is positive for an increased path length, which is the same convention as applied in equation 3.3.. The R factor further simplifies equation 3.3 within a layer i;

$$\frac{\Delta t_{int,i}}{t_{int,i}} = (1 + R_i)\frac{\Delta z_i}{z_i} \tag{3.10}$$

Equation 3.10 implies that time shift and strain are proportional in an interval. By assuming a constant R_i for the overburden, it is suggested that the portion of the time shift caused by thickness change is the same throughout overburden. But if R is depth-dependent, time shifts in certain intervals of the overburden are caused primarily by thickness change, while other intervals are dominated by velocity change. Further, the time shift for one layer may be estimated from reorganizing equation 3.10 and applying equation 3.2:

$$\Delta t_{int,i} = (1 + R_i)\Big(\frac{\Delta z_i}{z_i}\Big)\Big(\frac{2z_i}{v_{p,i}}\Big) \tag{3.11}$$

Synthetic time shifts can be calculated from equation 3.11, where the fractional change in layer thickness ($\frac{\Delta z_i}{z_i}$) is estimated from a geomechanical model. Rewriting equation 3.11 allows

for an expression for R_i given the time shift, thickness change and interval velocity;

$$R_i = \frac{\Delta t_{int,i} v_{p,i}}{2\Delta z_i} - 1 \tag{3.12}$$

If the overburden is divided into N layers, the total thickness change of the overburden (Δz_{total}) should equal the sum of the thickness change for every layer i. The thickness change for each layer can be determined by rearranging equation 3.11 to solve for Δz in every layer;

$$\Delta z_{total} = \sum_{i=1}^{N} \Delta z_i = \sum_{i=1}^{N} \frac{\Delta t_{int,i} \cdot v_{p,i}}{2(1 + R_i)} \tag{3.13}$$

By using the definition of R in equation 3.9 to express the strain in terms of velocity and R, it is possible to estimate the change in velocity for each interval based on the time shift and R.

$$\Delta v_{p,i} = -\frac{\Delta t_{int,i} \cdot v_{p,i}^2}{2z_i\left(\frac{1}{R_i} + 1\right)} \tag{3.14}$$

The overburden normally consists of several layers of different lithologies. In laboratory experiments, the R factor has proven to be strongly dependent on lithology because of varying rock properties, (Holt et al., 2008; Bathija et al., 2009). The same result is found using rock-physics models, (Carcione et al., 2007). (Holt et al., 2008), (Bathija et al., 2009) and (Carcione et al., 2007) conclude that the absolute value of R normally is larger in sandstone than in shale. Additionally, R varies more in sandstone than in shale, in other words; R is more sensitive to stress in sandstone. This is because velocity is more sensitive to stress changes in sandstone. (Lo et al., 1986) measured velocities on samples from Berea sandstone; fine-grained and well-sorted, and Chicopee shale; fine-grained, arkosic micaceous shale. Velocities were measured perpendicular and parallel to the bedding planes, presented in Figure 3.2. It is clear from the plots that the velocity in sandstone, Figure 3.2a, is more sensitive to stress changes than velocity in shale, Figure 3.2b. It is caused by cracks opening in sandstones at lower stress, (Bathija et al., 2009). Velocities in (Lo et al., 1986) were measured along bedding planes, V_{p11}, perpendicular to bedding planes, V_{p33},and at an angle to the bedding planes, V_{p45}. Velocities in shale showed more variation depending on which direction it was measured in, which implies that shale is more anisotropic. From Figure 3.2 it is also evident that the velocities for both shale and sandstone are more sensitive when the stress is low. Therefore, understanding the reservoir pressure regime is vital when studying 4D seismic, (Wang, 2001), as the relation between

seismic velocities and stress is non-linear, see Figure 3.2.

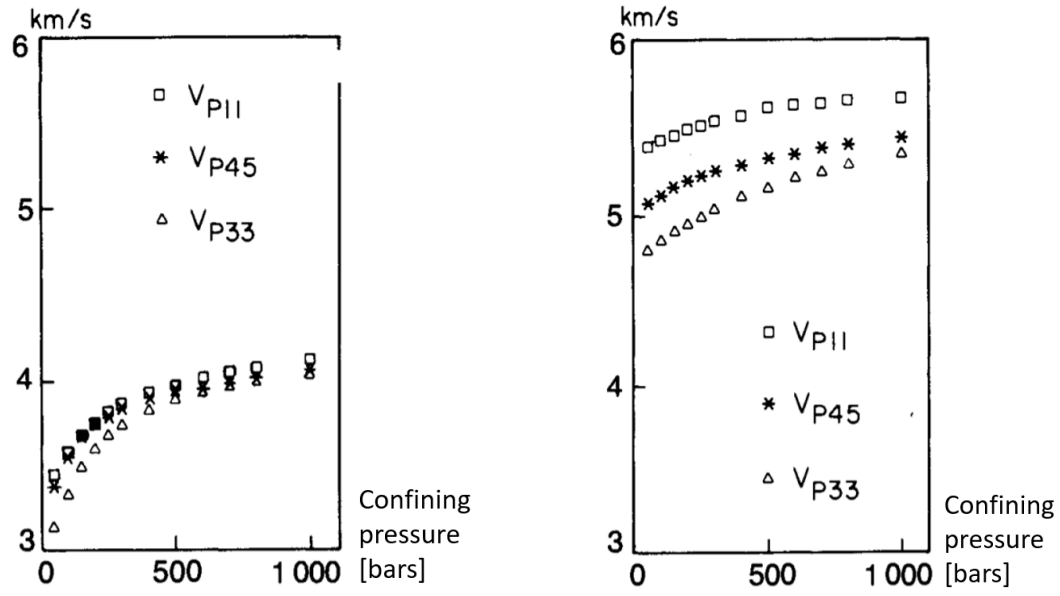

(a) Velocity for Berea sandstone.

(b) Velocity for Chicopee shale.

Figure 3.2: P-wave velocities for sandstone, 3.2a, and shale, 3.2b. Subscripts refer to velocity direction related to bedding planes; 11 is along bedding planes, 33 is perpendicular to bedding planes, 45 is at an angle to the bedding planes. Figure courtesy of (Lo et al., 1986)

Plots of strain for different rocks with decreasing hydrostatic pressure is given in Figure 3.3. The experiment was presented in (Bathija et al., 2009), where the plot is taken from. The test was performed on three sandstone samples with varying texture and grain sizes from fine to medium; referred to as Lyon, Berea and Foxhill. The shale was fine grained and laminated from the North Sea. The strain was measured during decreasing differential stress (unloading). From Figure 3.3 it is clear that the shale deforms more than the sandstones when subjected to decreasing pressure. The relationship between stress and strain is non-linear and the main sources for non-linearity and stress dependence are change in porosity with stress, the presence of sharp grain contacts and generation of cracks/fractures, (Holt et al., 2005).

To summarize; horizontal cracks or fractures, or weaknesses in grain contacts in vertical direction, complicates the relation of strain and velocity, (Holt et al., 2008), leading to a non-linear stress-velocity relationship. Accordingly, the definition of R where fractional changes in thickness and velocity are proportional is at best an approximation, (Røste and Ke, 2017). Nonetheless, for seismic applications it is convenient to relate time shifts to vertical strain ε_z.

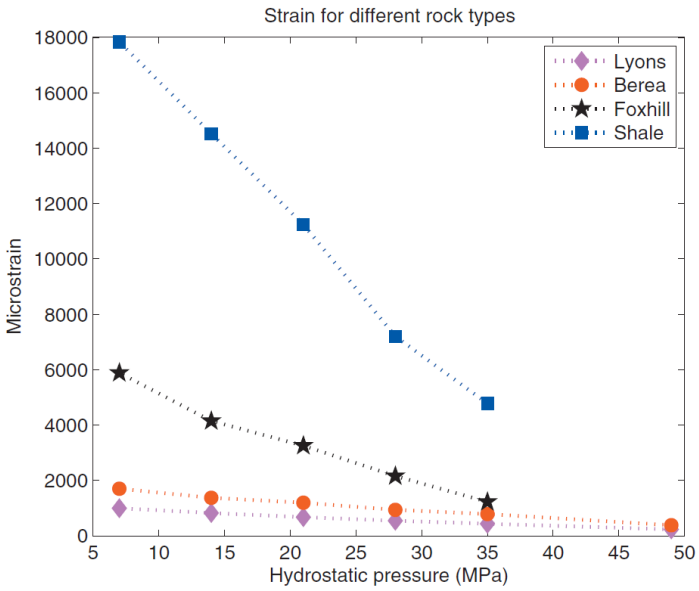

Figure 3.3: Strain for different rocks at decreasing hydrostatic stress, figure courtesy of (Bathija et al., 2009).

3.3 Geomechanics

When a rock is experiencing large enough stress, a failure will occur in the material. This implies that the shape of the rock will change permanently. Further, the ability for the rock to carry load will be reduced. The stress where failure occurs is referred to as the strength of the rock. The tensile strength, T_0, is a characteristic property of a rock and is a measure for how much the rock can be "stretched" before tensile failure occurs, see Figure 3.4a below. The tensile strength is usually very low for sedimentary rocks, typically a few MPa or less. During tensile failure a rock is typically split along fracture planes, and the largest cracks normally increase during further tensile stress, (Fjær et al., 2008). Compaction is the decrease in size of a formation, (Andersen, 1995). During compaction, stress increases in the opposite direction compared to a tensile failure, see Figure 3.4b. Compaction is the process where grains break and are pushed into the open pore space, leading to a closer packing of the rock. It happens more commonly in high porosity materials, where the structure is open and formed by grain skeleton. Failure may also occur by the grains being crushed or split, (Fjær et al., 2008).

Often there is no clear definition of failure for a material, as the transition to a material with decreased stiffness is gradual, yet the capacity to carry load is constant. Deformation of a rock during stress change can roughly be divided into three regions; elastic, plastic and brittle region, where the latter domain is where failure occurs. During elastic deformation the rock will return

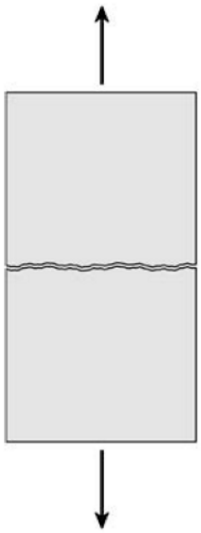

(a) Tensile failure.

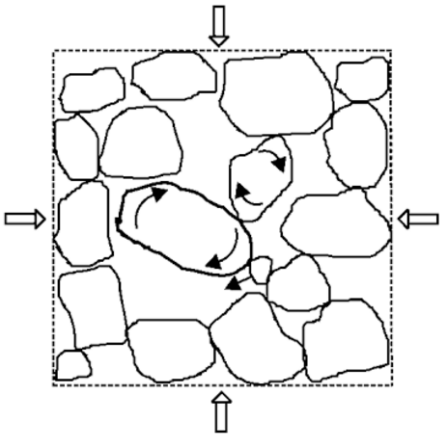

(b) Grain reorganization during compaction.

Figure 3.4: Illustrations of failure mechanisms caused by tensile stress and compaction, figure courtesy of (Fjær et al., 2008).

to its original state when stress is decreased. Elastic deformation dominates until yield point is reached. In the ductile region the deformation is permanent, but the rock is still able to carry load. In practice the ductile region may be very small. Deformation is increased in the brittle region and the rocks ability to carry load decreases drastically. For perfect modelling a rock, the post-yield phase of deformation should involve an inhomogeneous medium penetrated by cracks and faults. But since this model would be highly complicated, a commonly embraced idea is the theory of plasticity, which is mostly used for describing non-elastic deformation of metals. One important concept in the theory of plasticity is that the total strain resulting from a stress increase consists of an elastic part and a plastic part;

$$d\varepsilon_{ij} = d\varepsilon^e_{ij} + d\varepsilon^p_{ij} \tag{3.15}$$

Where $d\varepsilon^e_{ij}$ is the strain related to the elastic behaviour. This strain will re-inverse when the stress is released, while $d\varepsilon^p_{ij}$ is the permanent change caused by plastic deformation, (Fjær et al., 2008).

Thus, whether production-induced deformation in the overburden is elastic of plastic depends on the rock properties (the rock strength) and the magnitude of the production-induced stress changes.

3.3.1 Stress Arching

The R factor is expected to vary laterally at a field because the stress field changes, (Holt et al., 2005). Due to internal driving forces and external constraints, anisotropic changes in total stress may be induced. This phenomena is referred to as arching, (Mulders, 2003). A stress arch is generated as the overburden weight is supported by the sideburden rather than by the compacting reservoir, (Wang et al., 2015). Figure 3.5, inspired by (Wang et al., 2015), demonstrates the deformation processes in the overburden when a stress arch is formed. Directly above the depleting region, vertical stress will be released and the rocks will be stretched. In the overburden above the edge of the reservoir the weight of the overburden is partially shifted to the sideburden through the stress arch, resulting in additional friction force between the layers and increased shear deformation. The stress arch is also recognized by an increased vertical stress in the sideburden. Arching effects are enhanced in small and soft reservoirs, (Soltanzadeh et al., 2009). In short; the overburden right above the reservoir is generally stretching, while the overburden outside the reservoir boundary is compacting, (Geertsma, 1973). From Figure 3.5 it should be noted that the stress geometry changes drastic laterally. As a consequence the strain and velocity, and the resulting R factor, probably varies around the field as well.

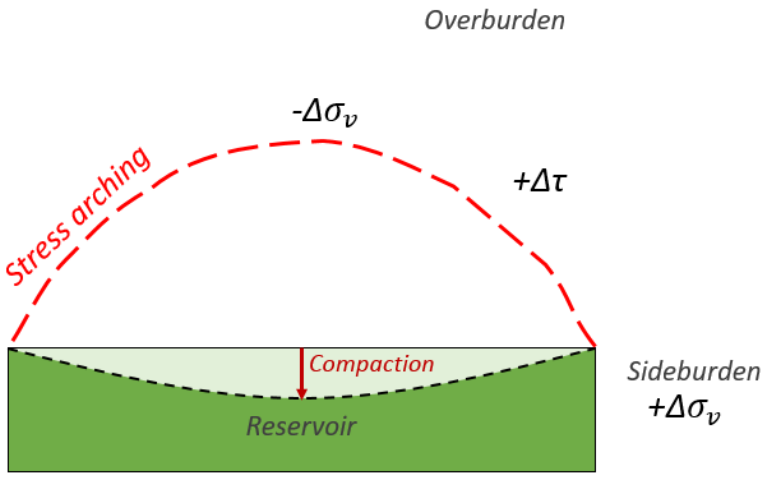

Figure 3.5: Schematic diagram of stress arching during production, inspired by (Wang et al., 2015). Vertical stress is reduced directly above the reservoir. In the overburden above the edge of the depleting reservoir shear deformation occurs. In the sideburden vertical stress is increased and rocks might compact.

3.3.2 Compaction and Subsidence

Compaction is simply large-scale manifestation of strain; a fractional change in the size of a body. This implies that the reservoir thickness is of importance for the magnitude of the compaction. In practice, production-induced compaction is how much the reservoir has shrunk vertically. Subsidence is a consequence of compaction, because the overburden follows when the underlying sediment drops. Usually the effects spread, leading to a subsidence bowl that is wider, but shallower, than the compaction area. The subsidence bowl tends to be symmetric despite highly localized compaction rates, because of the averaging effect of the spreading in the overburden, (Andersen, 1995). Figure 3.6 shows a situation where both the reservoir is compacting and the sea floor is subsiding.

Subsidence above a compacting reservoir is a result of the interaction between the reservoir and its elastic surroundings. Monitoring subsidence has gained more focus as it is valuable input to the geomechanical modelling of the overburden, in addition to confirming platform safety. Typical measurements of subsidence offshore is through the use of bathymetry surveys and GPS data. The former method applies an echo sounder to determine the water depth, this is an accurate measure of subsidence as long as the survey is wide enough to cover areas where the subsidence is estimated to be 0 to apply as a zero reference point. The procedure of using GPS satellite measured data is fully integrated at several fields, including the Ekofisk Field. The great advantage of GPS measurements is that it can measure subsidence continuously and may be combined with bathymetry data, (Mes et al., 1995).

The ratio of compaction and subsidence is dependent on the reservoir parameters, the size of the reservoir and the reservoir depth, where large reservoirs may cause corresponding high subsidence rates, (Geertsma, 1973). Certain studies assume the relation between compaction and subsidence to be constant, (Janssen et al., 2006), although this does not seem appropriate as the subsidence bowl is independent of localized compaction, (Andersen, 1995). The total thickness change of the overburden (Δz_{total}) due to compaction and subsidence is found from subsidence of the sea floor, S, and compaction of the reservoir, C:

$$\Delta z_{total} = -(C - S) \tag{3.16}$$

The minus sign in equation 3.16 is included because positive direction is set to be upwards in the calculations and simulations. Indicating that a positive reservoir compaction represents

an uplift of the reservoir. Substantial production-induced thickness change in the overburden might damage wells and lead to well collapses, especially in combination with stress arching.

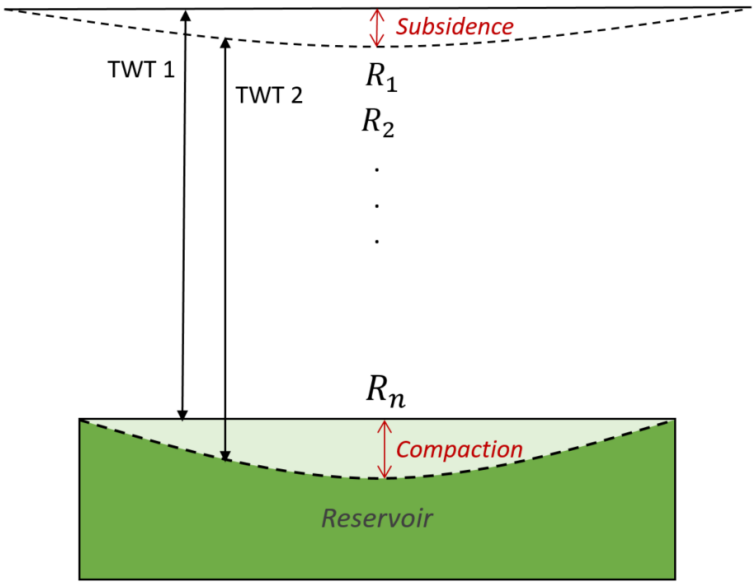

Figure 3.6: Schematic figure of depletion-induced reservoir compaction and corresponding sea floor subsidence. Solid lines are sea floor and top reservoir at the time of the first survey, dashed lines are sea floor and top reservoir at time of the second survey. TWT 1 is two-way traveltime at base survey, TWT 2 is two-way traveltime at monitor survey. R is estimated at different depths.

3.3.3 Geertsma's Nucleus of Strain Model

Production and injection in the reservoir cause changes in pore pressure, this alters the stress and strain field in and around the reservoir. A simplified model of how compaction of the reservoir leads to subsidence of the sea floor, in other words; how deformation propagates through overburden, is given by (Geertsma, 1973). The reservoir is treated as an isolated volume compacting in a half-space with a fraction-free surface, triggered by a changing pore pressure. The effects of the compacting unit on its surroundings is calculated using superposition. Some important simplifications in this analytical model are the following assumptions;

- Linear stress-strain relations.
- Uniform and homogeneous properties through the entire model, including no contrast in elastic properties between the reservoir and the surroundings.

The assumptions of linearly elastic and isotropic rock indicates that conditions in the overburden are close to constant mean stress or constant volume. It is a clear limitation that the

model is based on constant elastic properties through the reservoir and overburden. However, there exists analytic solutions to Geertsma's nucleus of strain model for a disk-shaped reservoir that give a general insight to the compaction and subsidence phenomena, (Fjær et al., 2008). A set of strain nuclei is situated at the depth $z = D$, implying that compaction is localized at this point. This introduces a small and negligible error. The parameters necessary to model the vertical displacement field around a compacting disk-shaped reservoir from (Geertsma, 1973) is presented in Table 3.1 below.

Table 3.1: Parameters in Geertsma's nucleus of strain model of the displacement field around a compacting disk-shaped reservoir, equation 3.19.

Parameter	**Description**	**SI unit**
D	Reservoir depth	m
z	Depth below sea floor	m
R	Reservoir radius	m
h	Reservoir height (pay thickness)	m
Δp_f	Pore pressure change	Pa
C_m	Uniaxial compressibility modulus	Pa^{-1}
α	Biot's coefficient	Dimensionless
ν	Poisson's ratio	Dimensionless
E	Young's modulus	Pa

The uniaxial compressibility, C_m, relates to different moduli of the framework to the rock; for instance Young's modulus (E_{fr}) and Poisson's ratio (ν_{fr}). It is the inverse of the uniaxial compaction modulus, H_{fr}:

$$C_m = \frac{(1+\nu_{fr})(1-2\nu_{fr})}{E_{fr}(1-\nu_{fr})} = \frac{1}{H_{fr}} \tag{3.17}$$

The vertical displacement along the center line of a disk-shaped reservoir is then expressed as an analytic equation in equation 3.18, which is based on the theory introduced in (Geertsma, 1973) presented in (Fjær et al., 2008);

$$u_z = -\frac{C_m h \alpha \Delta p_f}{2}\left(3-4\nu+\frac{D-z}{|D-z|}-\frac{D-z}{\sqrt{R^2+(D-z)^2}}-\frac{(D+z)(3-4\nu)}{\sqrt{R^2+(D+z)^2}}+\frac{2R^2 z}{(R^2+(D+z)^2)^{3/2}}\right) \tag{3.18}$$

In equation 3.18 it is clear that the magnitude of the displacement field is proportional to C_m, h, α and Δp_f, while the distribution of the displacement is a function of ν, D and R. Geertsma's formula for the vertical displacement field outside a disk-shaped reservoir is, (Fjær et al., 2008):

$$u_z = \frac{C_m R h \alpha \Delta p_f}{2}\left[\frac{z-D}{|z-D|}I_3(|z-D|) - (3-4\nu)I_3(z+D) - 2zI_4(z+D)\right] \tag{3.19}$$

$I_3(q)$ and $I_4(q)$ are given below for $q = |z-D|$ and $q = z+D$:

$$I_3(q) = -\frac{q\sqrt{m}K(m)}{2\pi R\sqrt{rR}} + \big(U(r-R) - U(R-r)\big)\frac{\Lambda_0(\beta|m)}{2R} + \frac{1}{R}U(R-r) \tag{3.20}$$

$$I_4(q) = \frac{m^{3/2}(R^2-r^2-q^2)E(m)}{8\pi(rR)^{3/2}R(1-m)} + \frac{\sqrt{m}K(m)}{2\pi R\sqrt{rR}} \tag{3.21}$$

Where m and β are:

$$m = \frac{4Rr}{q^2+(r+R)^2} \tag{3.22}$$

$$\sin\beta = \frac{q}{\sqrt{q^2+(R-r)^2}} \tag{3.23}$$

$F(\alpha|m)$ and $E(\alpha|m)$ are elliptic integrals of the first and second kind of the parameter m. And $K(m) = F(\frac{\pi}{2}|m)$ and $E(m) = E(\frac{\pi}{2}|m)$ are complete elliptic integrals of the first and second kind. U is the unit step function, $U(x \geq 0) = 1, U(x < 0) = 0$. $\Lambda_0(\beta|m)$ is called Heuman's lambda function, $\Lambda_0(\frac{\pi}{2}|m) = 1$.

3.3.4 The Principle of Superposition

The superposition principle is a basic theorem of linear differential equations, (Berg and MacGregor, 1969). The theorem states that for all linear systems the response to all actions is the sum of the response for each action alone. This principle may be utilized to simplify the modelling of the displacement field around several adjacent sources of compaction. The total displacement field in the vertical direction for three reservoirs can then be expressed by equation 3.24, where $u_{z,n}$ is the displacement field for reservoir n.

$$u_{z,total} = u_{z,1} + u_{z,2} + ... + u_{z,n} \tag{3.24}$$

3.4 Elastic Properties for Chalk

Chalk is composed of skeletons of algae called coccospheres. Matrix permeability is typically quite low, between Micro - and milliDarcy. In North Sea chalk reservoirs the formations are naturally fractured, leading to permeability in the 100 milliDarcy range. The mechanical behaviour of chalk depends primarily on the porosity and secondarily on silica content, (Fjær et al., 2008). Further, higher silica content increases Young's modulus and the yield stress for chalk, (Andersen, 1995).

As demonstrated in Table 3.1, the elastic properties required in Geertsma's nucleus of strain model are uniaxial compressibility modulus, Young's modulus, Poisson's ratio and Biot's coefficient. Properties of North Sea chalk has been widely studied, and the conclusions are diverse depending on method and sample origin. (Olsen et al., 2008) studied dynamic and static Young's moduli for both dry and water-saturated chalk from the North Sea based on laboratory tests. The samples were from reservoir rocks of the Nana oil well in the Danish part of the North Sea and from the outcrop at Stevns in Denmark. It was observed that the dynamic moduli was 2-5 times larger than the static moduli for a water-saturated sample. For a water-saturated chalk the static Young's moduli varied between 2.8 GPa to 9.6 GPa for the samples with no visible fractures. An extensive work on rock mechanics for chalk was presented by (Havmøller and Foged, 1996). They created a database consisting of 664 data sets of reservoir chalk and 140 data sets of outcrop chalk to establish correlations between mechanical properties and porosity, (Fjær et al., 2008). 197 of these data sets are from the Ekofisk Field. The overall trend for the

elastic Young's moduli in chalk was suggested as;

$$E = 22.5e^{-11.2\phi} \tag{3.25}$$

E is given in GPa and ϕ is given as a fraction. The trend for uniaxial compaction modulus from (Havmøller and Foged, 1996) can be summarized by the following equation:

$$H = 13.6e^{-9.29\phi} \tag{3.26}$$

Where H is in GPa and ϕ is a fraction. Values for Young's modulus and uniaxial compaction modulus are quite low for chalk. The elastic parameter Poisson's ratio is defined as lateral expansion relative to longitudinal contraction, (Fjær et al., 2008):

$$\nu = -\frac{\varepsilon_y}{\varepsilon_x} \tag{3.27}$$

Poisson's ratio is typically in the range 0.15-0.25 for rocks, but for weak and highly porous rocks it may approach zero or become negative, (Fjær et al., 2008). (Havmøller and Foged, 1996) found no clear correlation between ν and porosity. The range was from 0.05 to 0.35, with a mean value of 0.21 for all chalk samples.

(Teufel and Warpinski, 1990) concludes that the Biot coefficent decreases from about 1 for high porosity chalk to around 0.8 for 15% porosity chalk, (Andersen, 1995). (Engstrøm, 1992) established the following correlation between Biot coefficient and porosity for all types of chalk:

$$\alpha = 1 - \frac{e^{-11.2\phi}}{1 - 0.548\phi} \tag{3.28}$$

Chapter 4

Methods

4.1 4D Seismic

In 2010 permanent seismic cables were installed at the seabed of the Ekofisk Field and the following seismic gatherings are referred to as Life of Field Seismic (LoFS) data. It is desirable to study LoFS data rather than streamer data as the quality is better and more consistent; the permanent installation removes many sources of random noise (excluding rig activity) and minimizes the differences between the surveys, which leads to increased repeatability, (Kommedal et al., 2004; Landrø, 2010). However, the LoFS data from 2010 was not a success and is rarely used, therefore LoFS2 from 2011 is examined instead and used as a base survey for the 4D seismic in this project. Since 2011-2014 correlate well to bathymetry surveys, which is useful to estimate subsidence of the sea floor, it was concluded that LoFS8 from 2014 was a suitable monitor survey. Hence, this study has focused on LoFS2 and LoFS8 data. The time shifts are calculated from equation 3.1, where base and monitor are LoFS2 and LoFS8 from 2011 and 2014, respectively;

$$\Delta t = t_{LoFS8,2014} - t_{LoFS2,2011} \tag{4.1}$$

This implies that a positive time shift represents a slow-down and longer traveltime in monitor survey (2014), while a negative time shift is a speed-up and shorter traveltime in monitor survey.

4.1.1 Focus Areas

Figure 4.1 below is the time shift map from top reservoir at the Ekofisk Field from LoFS8-LoFS2 data. Throughout this report the scale is adjusted so that a positive time shift is blue, while a negative time shift is red. The blue line from NW-SE is the profile in Figure 4.2. Gas above the center of the Ekofisk Field results in poor seismic here. The affected area is referred to as the seismic obscured area and is marked by the yellow dotted line in Figure 4.1. The focus areas of this project are southwest, and are marked by three circles. The black circles represent repressurization zones and are referred to as injection zone 1 and injection zone 2, because there are many injectors in the region repressurizing the reservoir. Injection zone 1 and 2 are marked in Figure 4.1. From the time shift map it is clear that the amplitude is stronger in injection zone 1 than injection zone 2, see close-up of the time shift map of the focus areas in Figure 4.3. Both regions are covered by six black symbols, which represent pseudo wells that are used in this research and are explained in detail below. The area within the white circle represents the region that is undergoing a considerable depletion. It is referred to as the depletion zone in this report.

4.1.2 Data Extraction

To establish the time shift curve in depth, the overburden is divided into intervals where top and base horizons are picked based on strong and consistent reflectors. At these reflectors the time shift, depth and traveltime are measured. By having strong reflectors one minimizes the error of comparing wrong reflectors. The results were optimized by having intervals of approximately the same thickness. Figure 4.2 demonstrates the horizons that are picked and studied, except the uppermost black line that represents the water bottom. The overburden is divided into three primary groups based on lithology; the Nordland group, Hordaland group and Rogaland group. The black lowermost line is top reservoir and the line above is the Balder formation, representing the top of the Rogaland lithological group. Figure 4.2 is the cross-section marked as the blue line in Figure 4.1.

The approach to estimate the time shift curve in the overburden has been to introduce pseudo wells around each focus area. These are vertical imaginary wells. The time shifts are extracted as well logs along these profiles in order to see the time shift at different depths in the overburden. The time shift is also studied at each horizon in Figure 4.2 for every pseudo well. In

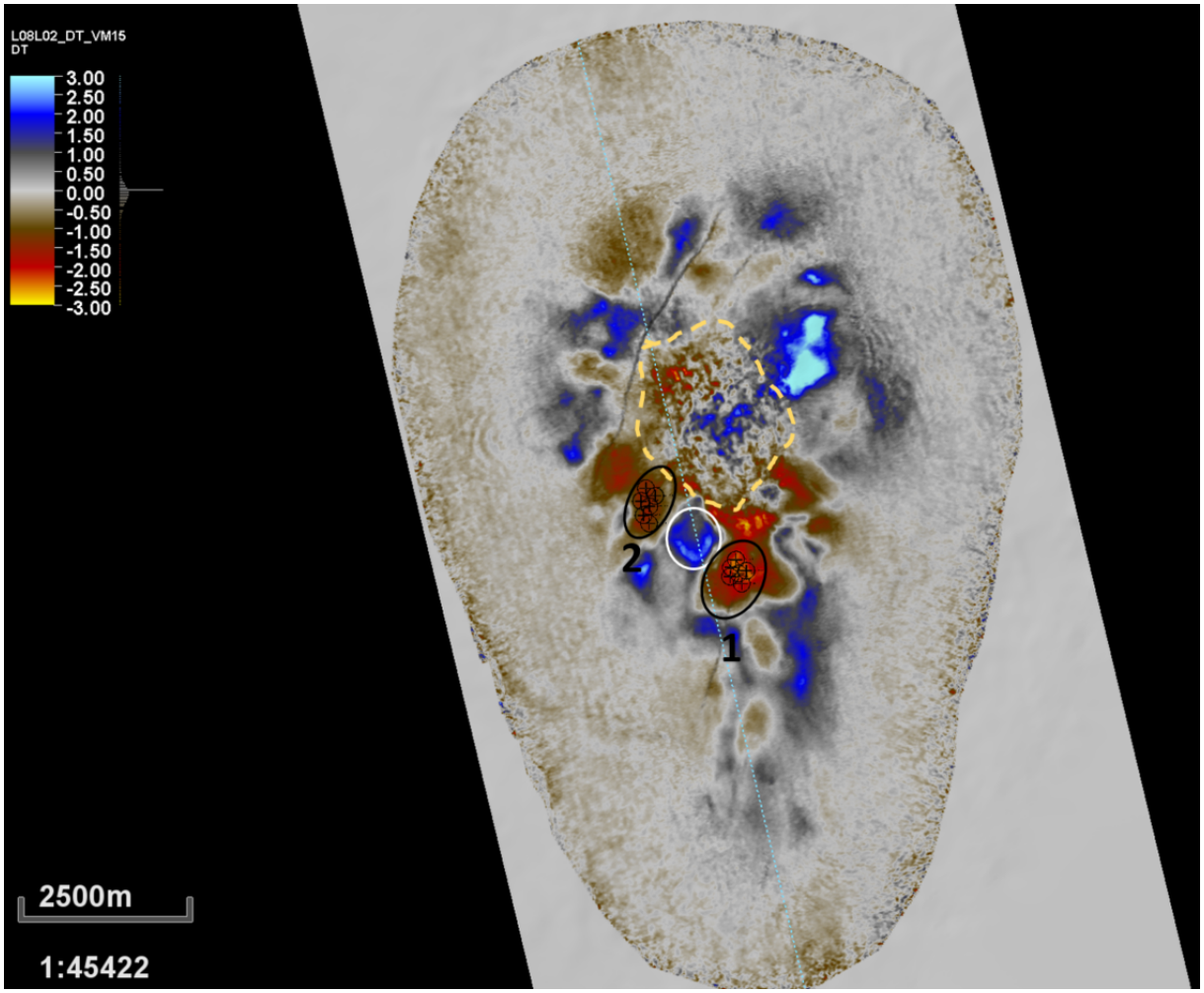

Figure 4.1: Time shift map of top reservoir from 2011 to 2014, scale from 3 ms to -3 ms. Black circles mark injection zone 1 and 2, while the white circle mark the depletion zone. Black symbols are pseudo wells in the injection zone. The yellow dotted line marks the seismic obscured area. Dashed blue line represents the cross section displayed in Figure 4.2.

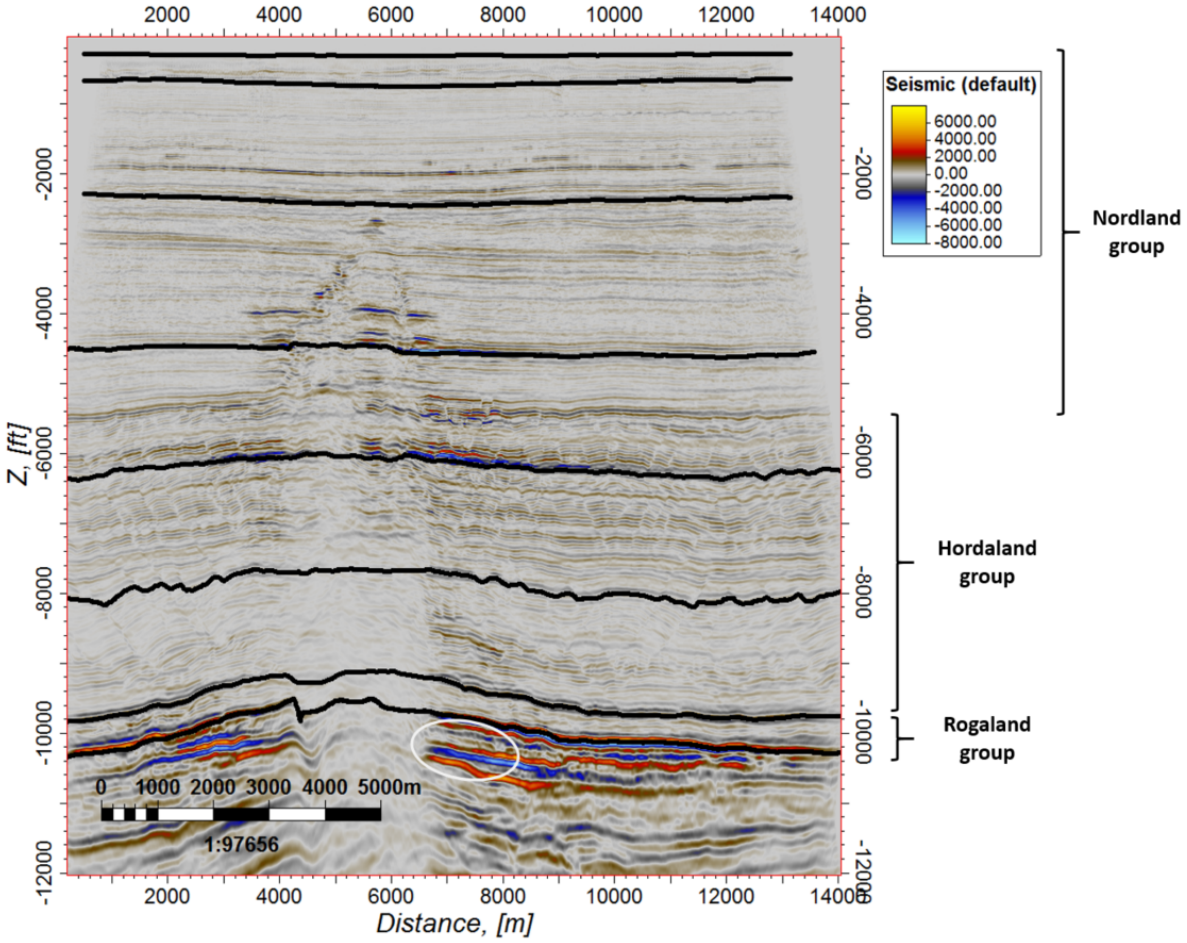

Figure 4.2: Seismic profile from inline 560 showing the horizons that are studied in the overburden (black lines). Inline 560 is the blue line in Figure 4.1.

total six pseudo wells were studied for injection zone 1 and 2 and seven for the depletion zone, which were all distributed laterally around each focus area to represent the time shift of the entire region. See Figure 4.3 for a close-up of the focus areas with the pseudo wells marked, the black symbols are the pseudo wells in the injection zones and the white symbols are the pseudo wells in the depletion zone. The pseudo wells also provide consistent points of measurement for estimation of subsidence and compaction. Further, the time shift was averaged between the wells to find one representative time shift value. It was ideal to place the wells around the focus area with some variance in the time shift value to get an idea of the average state of this area.

Using the depth-converted LoFS2 seismic; the depth to each horizon in Figure 4.2 was measured at each of the pseudo well locations. The representative depth of each horizon was then found from the average of the value for the wells. Hence, the time shifts and depths were measured at the same interfaces and are all averaged.

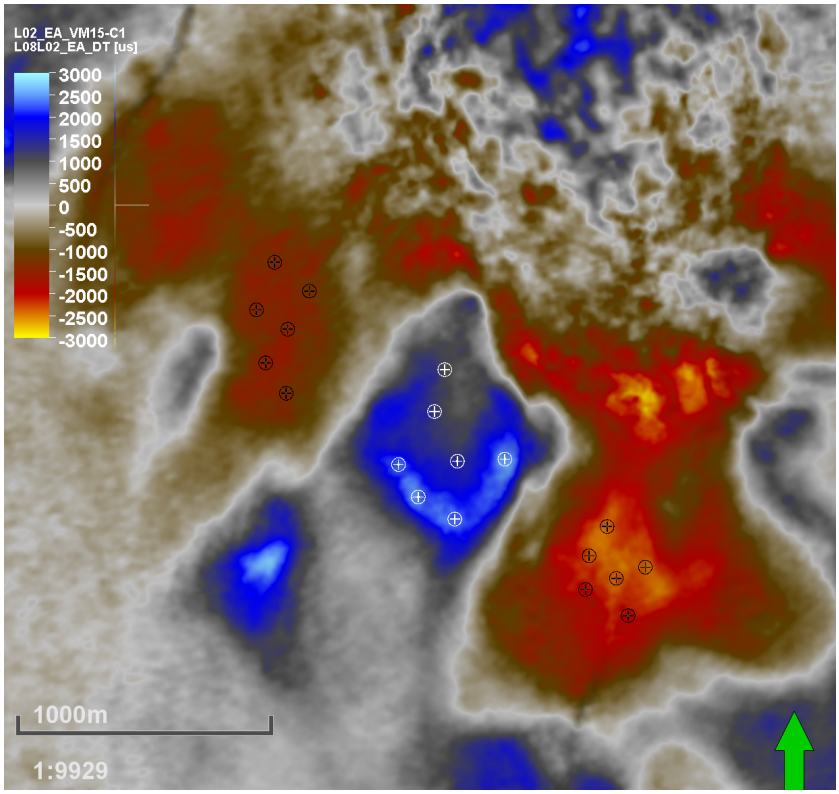

Figure 4.3: Close-up of the focus areas from time shift map from top reservoir, scale from 3 ms to -3 ms. White symbols are pseudo wells in the depleting zone, black symbols are pseudo wells in injection zones.

Velocity data in the overburden is from sonic logs from six exploration wells; 2/4-2, 2/4-3, 2/4-4, 2/4-5, 2/4-6 and 2/4-9. The five former are all drilled between 1969 and 1970, while 2/4-9 is drilled in 1973. These wells are chosen as the sonic log starts shallow and the wells have a fair spatial distribution. They are all drilled prior to the main production start in 1975 and are believed to represent the pre-production velocities of the overburden. The overall velocity for the overburden is averaged and smoothed between these six wells using MATLAB to estimate the velocity curve in depth.

4.2 Sea Floor Maps

ConocoPhillips regularly perform bathymetry surveys covering the sea floor around the Ekofisk Field. The surveys correlate well to the LoFS2 and LoFS8 gatherings, seeing that bathymetry was measured in April 2011 and August 2014. The resulting sea floor maps are shown in Figure 4.4 for 2011 and 2014, respectively. The black symbols are the pseudo wells in the injection zones, while the white symbols are the pseudo wells in the depletion zone. The color map scale

is the same for both maps, -225 ft to -265 ft, and it is given with reference to a zero point on the sea floor further away from the field. An important observation is that the bathymetry survey from 2014 is much narrower than the 2011 survey, this is discussed in Section 5.2 and Section A.5. In order to estimate the sea floor subsidence for this period, a sea floor subsidence map is created by subtracting the sea floor map in 2014 from the sea floor map in 2011. The representative subsidence value for the focus areas is then estimated by measuring the subsidence at the locations of each of the pseudo wells to further average the value between the locations.

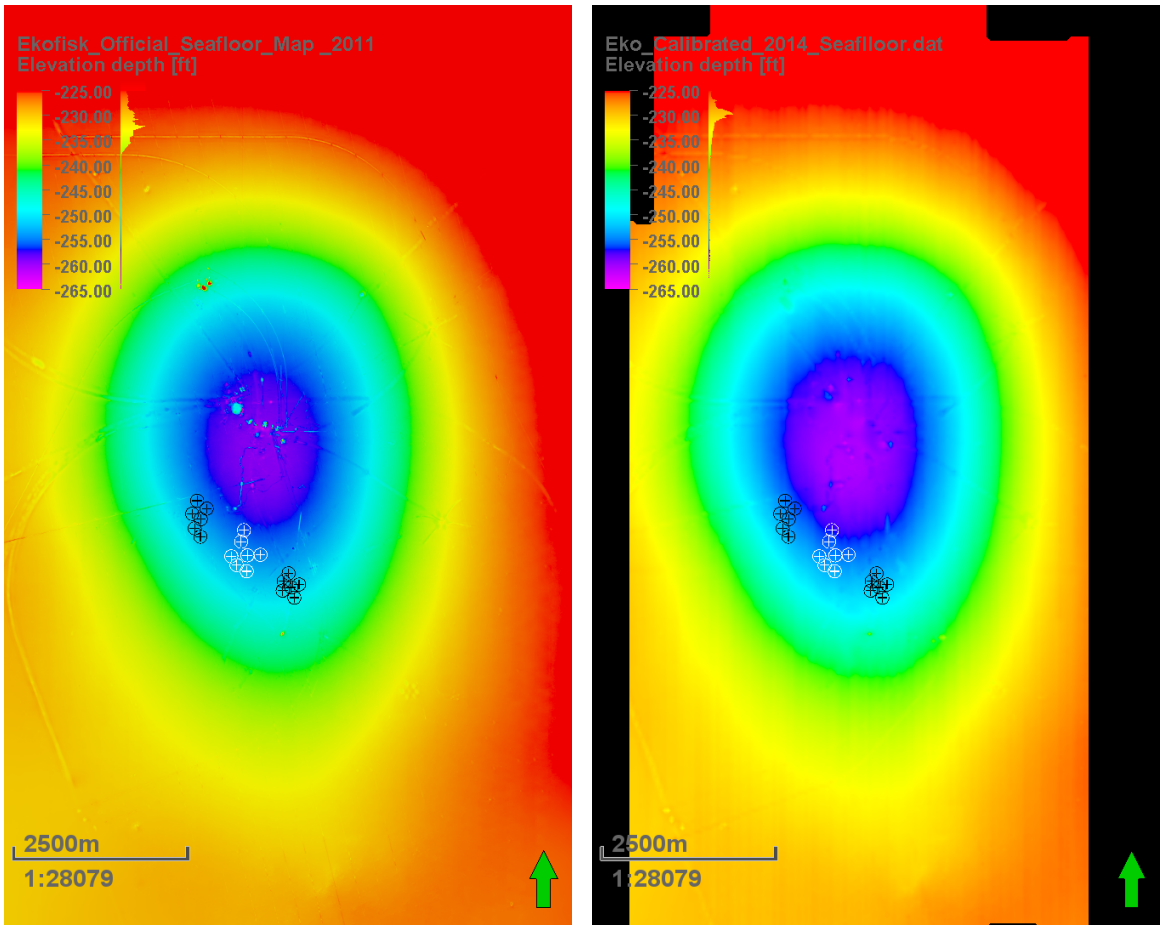

(a) 2011 Sea floor map **(b)** 2014 Sea floor map

Figure 4.4: Sea floor map for 2011 and 2014, respectively. Same scale; -220 ft to -265 ft. Black marks are the pseudo wells in the injection zone, white symbols are the pseudo wells in the depletion zone.

4.3 Reservoir Compaction

From equation 3.16 one can estimate the total stretch of the overburden from compaction of the reservoir and subsidence of the sea floor. However, there is no monitoring well around the focus areas, therefore the compaction is not well established. For that reason, both the compaction and the distribution of thickness change is modelled using Geertsma's nucleus of strain model in the focus areas in this project. Moreover, the resulting compaction from Geertsma is compared to the reservoir model for compaction applied by ConocoPhillips to discuss whether the compaction from Geertsma's nucleus of strain model is realistic. The compaction of top reservoir from ConocoPhillips' reservoir model is seen in Figure 4.5 for a region around the focus areas, the scale is in feet. The compaction in ConocoPhillips' reservoir model is presented as positive for increased compaction, but for the calculations in this project positive compaction implies reservoir uplift. Red symbols are pseudo wells in the depletion zone, while yellow symbols are pseudo wells in the injection zone. However, since the compaction is modeled and not measured directly there is uncertainty related to the value.

From Figure 4.5 it is obvious that the compaction is very heterogeneous, varying from 0 to 3.65 m just within the depletion zone. Moreover, the model implies that the top reservoir cannot be lifted; reservoir compaction cannot be negative. The monitoring well C-11 is placed in the center of the field. This well is used to regularly monitor the compaction of the top of the reservoir using radioactive marker bullets, (Janssen et al., 2006). For an arbitrary three-year period between 2010 and 2015, C-11 registered a compaction of around 0.5 m, which is clearly smaller than the compaction estimated in Figure 4.5 in parts of the depletion zone. However, from Figure 4.5 it is obvious that compaction is very localized. Furthermore, different production rates at the time interval in question makes it unfit for a direct comparison. Data from C-11 shows that large-scale compaction is possible; in a three-year interval (from 1995 to 1998) a compaction of 2.5 m was measured.

From equation 3.10 it is suggested that the thickness change distribution should be similar to the time shift curve. This should be taken into account when critically studying the results from the simulations using Geertsma's nucleus of strain model.

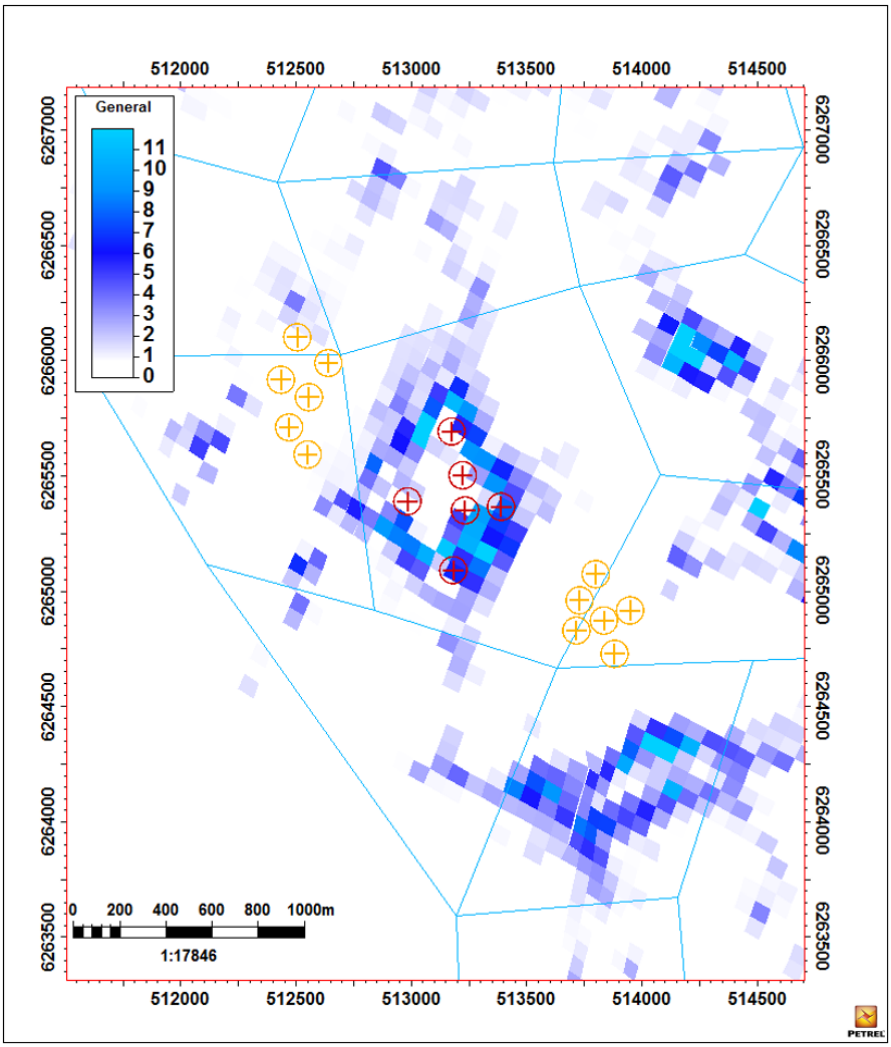

Figure 4.5: Reservoir compaction from ConocoPhillips' reservoir model. Scale is in feet.

4.4 Implementation of Geertsma's Nucleus of Strain Model

Equation 3.19 is applied to model the displacement field around one depleting reservoir in MATLAB. The displacement is estimated at each point in a grid, where the number of rows is determined by how thick the intervals in depth are, referred to as the layer thickness z. The number of columns is determined by the horizontal distance between each measured point, r_{int}. The grid is sketched in Figure 4.6. Table 4.1 displays the value for horizontal and vertical step size have been used in the simulations.

Table 4.1: Size of step between each grid cell in vertical and horizontal direction.

Parameter in model	Step size, [m]
z	10
r_{int}	30

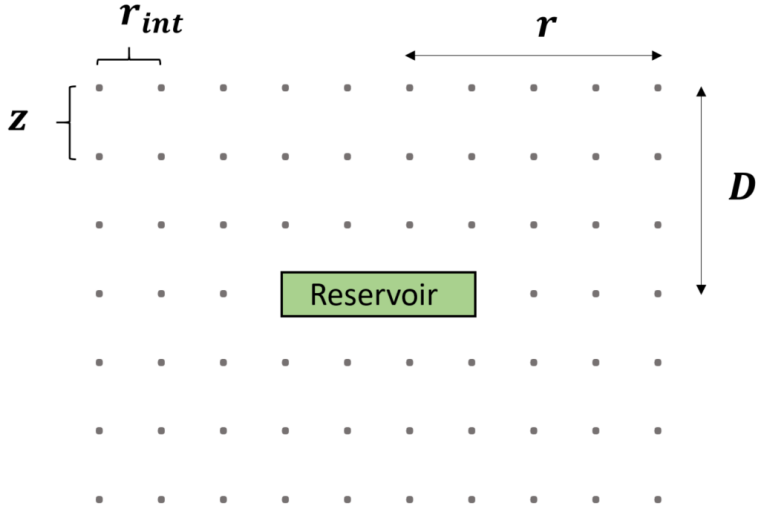

Figure 4.6: Schematic illustration of grid where the displacement is estimated at each grid point. The vertical and horizontal distance between the grid points are z and r_{int}. r is the radius of the displacement field, and D is the depth to the center of the reservoir.

From well logs and depth-converted seismic the average depth to the top reservoir is estimated to be around $D_{TopRes} = 3000m$ for all three focus areas. Moreover, the pay thickness is set to $h = 300m$, (Sulak et al., 1991). For the Geertsma model, this means that the center of the reservoir is located at:

$$D = D_{TopRes} + 0.5 \cdot h = 3150m \tag{4.2}$$

The strain is estimated from the displacement field. In pursuance of a realistic model it is also necessary to evaluate the results from the model using modelled reservoir compaction and measured sea floor subsidence. The analytic Geertsma solution, equation 3.18, was used to estimate the compaction, subsidence, displacement and strain along the center-line above a disk-shaped reservoir. The analytic solution of Geertsma's equations was tested for several combinations of different pore pressure changes and reservoir radii, in order to get a better understanding of the compaction/subsidence relation in general.

Based on the presentation of the Ekofisk Field in Chapter 2, it is obvious that the reservoir is highly complex. Therefore, the reservoir parameters vary strongly both laterally and vertically. A Poisson's ratio of $\nu = 0.2$ is applied in the modelling, based on lab data on Ekofisk chalk from (Havmøller and Foged, 1996). From well logs and ConocoPhillips' reservoir model, porosity in the focus areas is around 35 %, which correlates well to the porosity range presented in Table 2.1. The elastic moduli estimated based on this porosity is given in Table 4.2. These values are used in the simulations.

Table 4.2: Reservoir parameters and elastic moduli used in the simulations of the Geertsma's nucleus of strain model. Calculated from given equations with 35 % porosity.

Equation	**Parameter**	**Unit**	**Value when ϕ = 0.35**
3.17	C_m	GPa^{-1}	1.899
3.25	E	GPa	0.446
3.26	H	GPa	0.527
3.28	α	-	0.975

4.4.1 Modelling the Ekofisk Field Using the Superposition Principle

The superposition principle was employed to make the results from Geertsma more representative of the real-life situation. Moreover, to evaluate the effects on subsidence, compaction and strain in the overburden of having several sources of stimuli at reservoir level. The approach was to model the displacement field from each reservoir using equation 3.19 and simply add them, following the superposition principle in equation 3.24. Two models of the Ekofisk Field have been made. Model 1 is sketched in Figure 4.7 and represents the Ekofisk Field as sketched in Figure 4.8, where reservoir 1 represents a large reservoir covering most of the field and two smaller reservoirs (2 and 3) are placed within it. Model 2 is presented in Section A.4.1 in the Appendix. Figure 4.7 demonstrates the displacement field around the three reservoirs from model 1, where the dotted line is the center-line through the reservoirs. The colors grey, red and blue represent reservoir 1, 2 and 3, respectively. The green regions represent the reservoir. Each reservoir has an independent reservoir radius, R_n, and pore pressure change, $\Delta p_{f,n}$. r_n is the radius of each the deformation field, and $r_1 = r_2 = r_3$. The other input parameters required in Geertsma's nucleus of strain model, see Table 3.1, are kept equal for all three reservoirs during the simulations.

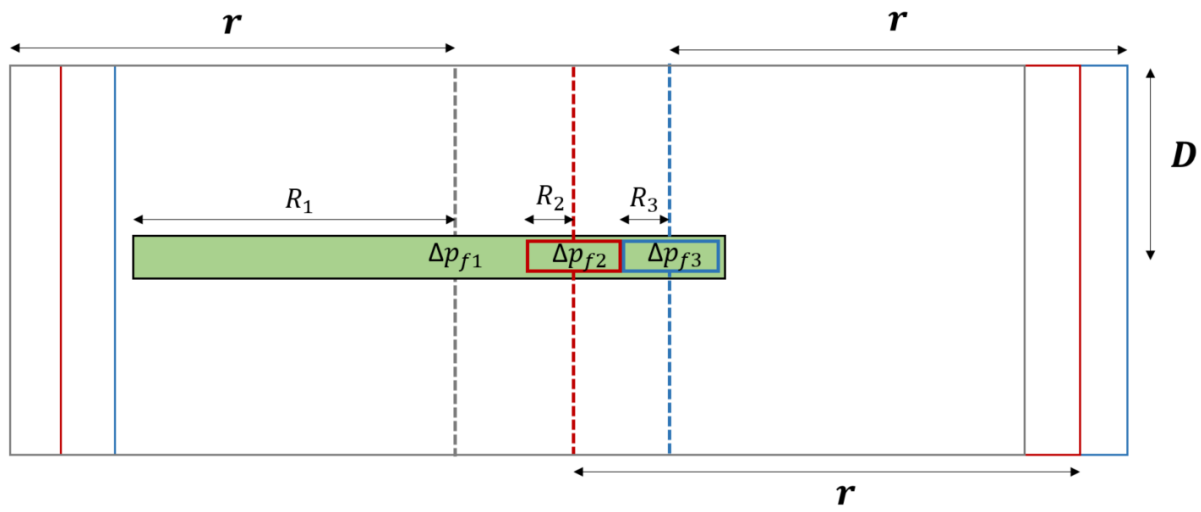

Figure 4.7: Sketch of the superposition principle being applied to the displacement fields from Geertsma's nucleus of strain model in model 1. The three reservoirs have individual reservoir radii; R_n and pore pressure depletion; $\Delta p_{f,n}$. The radius of the displacement field from each reservoir is r. D is the depth to the center of the reservoir. The dotted lines are the center-lines through each reservoir.

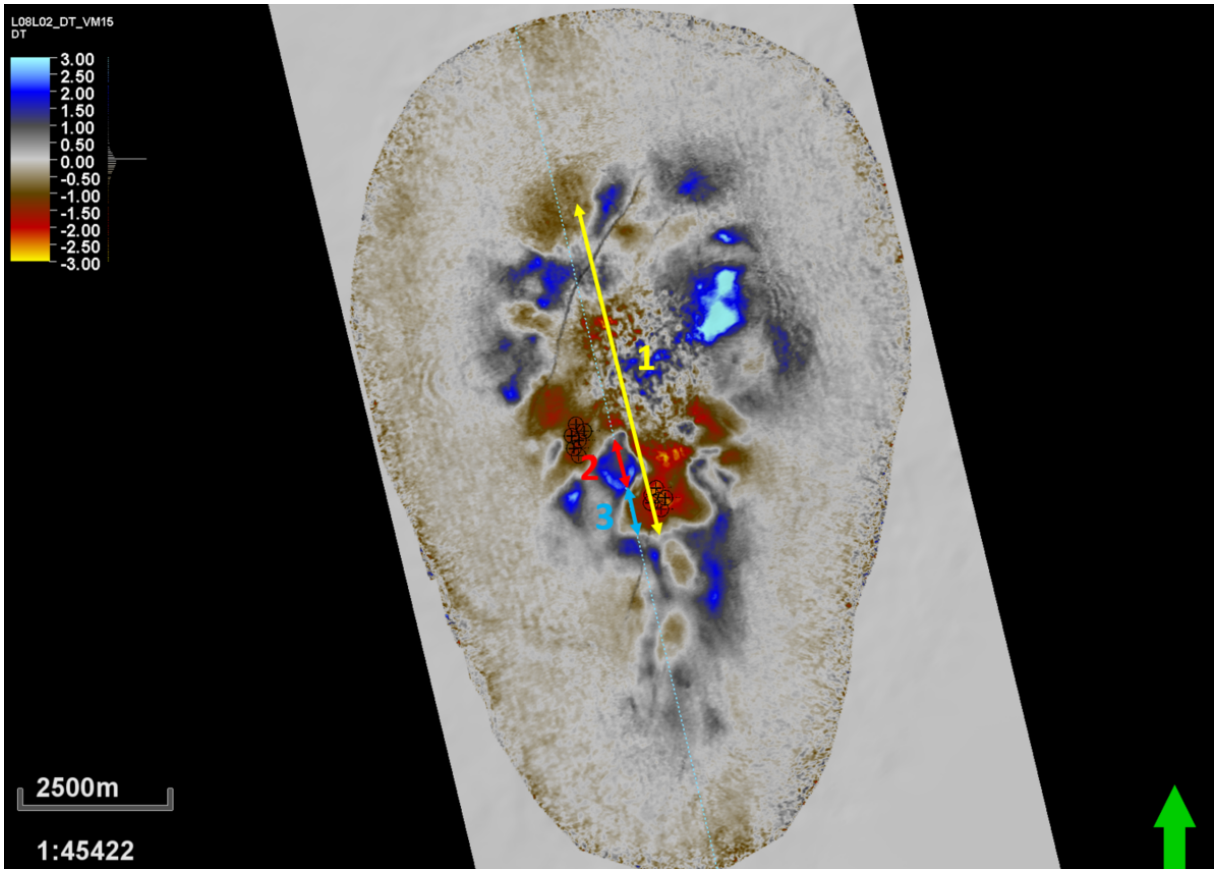

Figure 4.8: Illustration of how the Ekofisk Field is described by model 1; one large reservoir (reservoir 1) with two smaller reservoirs within it (reservoir 2 and 3) with independent pore pressure changes.

The radius of every reservoir in model 1 is based on the observed reservoir radius of the area 1, 2 and 3, which are marked in Figure 4.8. But the pore pressure change for each reservoir also needs to be established. The convention of having positive pore pressure change as depletion is used in Geertsma's nucleus of strain model in equations 3.18 and 3.19. Table 4.3 shows net volume produced and injected in the period between 2011 and 2014. The field has produced 108 291 845 bbl more fluid than the volume that has been injected. This implies that the overall pore pressure of the field should be dropping in this period, and that both compaction and subsidence should increase.

Table 4.3: Net fluid injected and produced from the Ekofisk Field in the period between 2011 and 2014.

Net fluid produced, [100 000 bbl]	**Net fluid injected, [100 000 bbl]**	**Difference, [100 000 bbl]**
5708.9	4625.9	1082.9

The in-house reservoir model applied by ConocoPhillips maps and models pore pressure. However, the Ekofisk Field is a very large and complex reservoir where the pore pressure change varies both in lateral and vertical direction. Therefore certain zones can show a significant pore pressure depletion, while other zones show no change at all. Although the reservoir model is based on some measured data such as pressure measured during drilling and at wells during shut-in, most of the data is modelled and may not be correct. Nonetheless, it does provide indications of maximum realistic pore pressure change.

It is important to note that all stress and strain is assumed elastic in Geertsma's nucleus of strain model. Furthermore, the model does not take gravity into account. This implies that a negative pore pressure change, which represents injection in this case, leads to the exact same displacement in the overburden as a positive pore pressure change, only in the opposite direction. Hence, the weight of the overburden is not considered and therefore the pore pressure changes in the injection zones applied in the Geertsma model should be far smaller than what is suggested by the reservoir model. It is more important that the displacement in the overburden is realistic than applying the exact observed pore pressure, although Δp_f needs to stay realistic. In practice it required multiple simulations to test different reservoir pore pressure to establish values that fit the observed sea floor subsidence. The final pore pressure change and radius for each reservoir used in the simulation is presented in Table 4.4. Reservoir 3 is undergoing an

injection and henceforth a positive pore pressure change. However, it should be noted that since reservoir 2 and 3 is situated within reservoir 1, the pore pressure change in reservoir 1 affects the displacement in and around reservoir 2 and 3. Hence, the pore pressure changes in reservoir 2 and 3 are in practice more negative than what is presented in Table 4.4.

Table 4.4: Radius and pore pressure change for each of the three reservoirs in the simulations of Geertsma's nucleus of strain model for model 1.

Reservoir	Radius, [m]	Pore pressure change, [MPa]
1	2800	1.5
2	300	3
3	300	-3

4.5 Synthetic Time Shifts and Depth-Dependent R Factor

From equation 3.11 synthetic time shifts are estimated based on the strain estimations from Geertsma's nucleus of strain model. MATLAB is used to find the average velocity in each interval in depth, since all equations using R is based on a constant velocity for each interval. The application of a constant velocity does imply some error, therefore it is beneficial to chose intervals where velocity is rather similar, in other words; smaller intervals. The synthetic time shift is compared with the observed time shift in each interval i;

$$\epsilon_i = |\Delta t_i - \Delta t_i^*| \tag{4.3}$$

Where Δt_i^* represents the synthetic time shift. The R factor that gives the smallest ϵ in each interval is presented as the optimal R in the given interval, resulting in a depth-dependent R. The workflow to estimate the depth-dependent R is demonstrated in the flow chart in Figure 4.9. Further, the synthetic time shift is estimated in each interval, and the cumulative time shift must be established by summing the time shifts for all intervals in the overburden. A large interval of R values were tested, but a range from 0 to 20 was found to fit the time shifts in this study. R factors were tested stepwise in increments of 1.

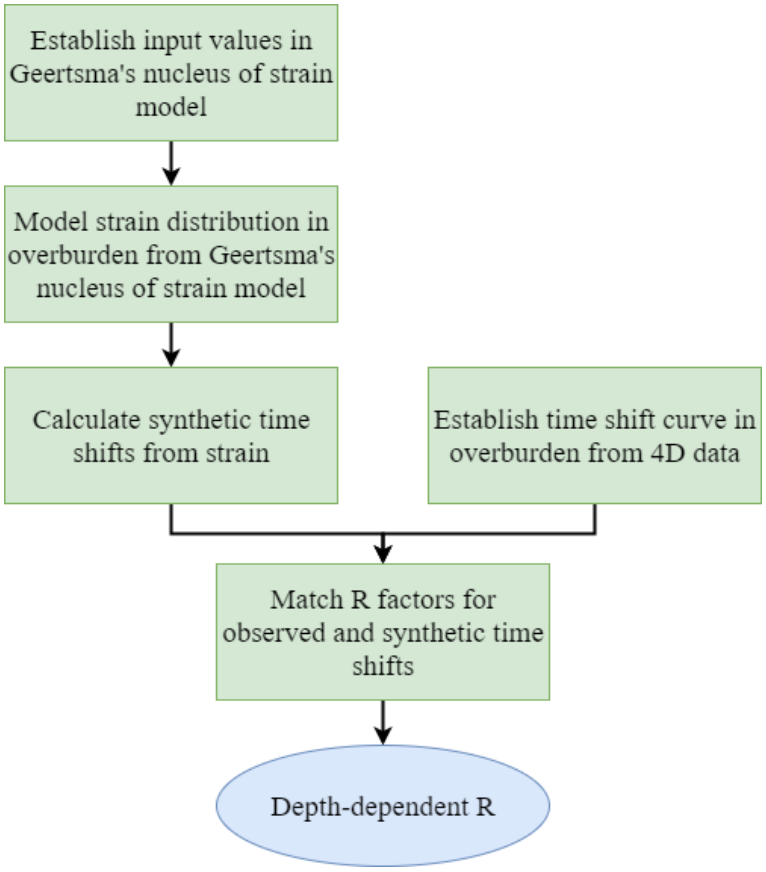

Figure 4.9: Workflow diagram for estimating the depth-dependent R factor from Geertsma's nucleus of strain model and 4D seismic.

4.6 Estimation of the Constant R Factor

Referring to section 1.2; a constant R in this report refers to an R that is constant in the vertical direction. This means that the constant R may vary laterally across a field. When estimatin the constant R factor, the overburden can be treated as one interval where equation 3.12 is applied to estimate R directly from the time shift, thickness change and velocity for the interval. By treating the overburden as one layer, the time shift at top reservoir represents the interval time shift. The thickness change applied in equation 3.12 is the total thickness change of the overburden, estimated from the compaction at top reservoir and subsidence of the sea floor by equation 3.16. However, the approach introduces some error with respect to estimation of the average P-wave velocity, since it has to be the average velocity of the entire overburden. Not to mention that the compaction at top reservoir is modelled and not measured. Consequently, this results in a constant R that is independent of the time shift curve in depth and only reliant on

the time shift at top reservoir and overburden thickness change.

Equation 3.13 indicates that the thickness change in each interval can be estimated from the interval time shift, R and the average interval velocity. Moreover, the sum of the thickness change for every interval in the overburden should equal the thickness change estimated from compaction and subsidence in equation 3.16. Consequently, it is possible to test a variety of R factors to see which fulfill equation 3.13. It should be noted that the R that is tested is constant in depth. The process is shown in the flow chart in Figure 4.10. First, the time shift curve in the overburden is established from 4D seismic. By testing a range of R; the thickness change is estimated for each layer ($\Delta z(interval)$ in Figure 4.10) using R, time shift and velocity. Then, by summing the thickness change for all layers $\left(\sum \Delta z(interval)\right)$, the sum should equal the total stretch of the overburden from equation 3.13 $\left(\sum \Delta z(total)\right)$. Hence, the R that fits this criterion might be a suitable constant R.

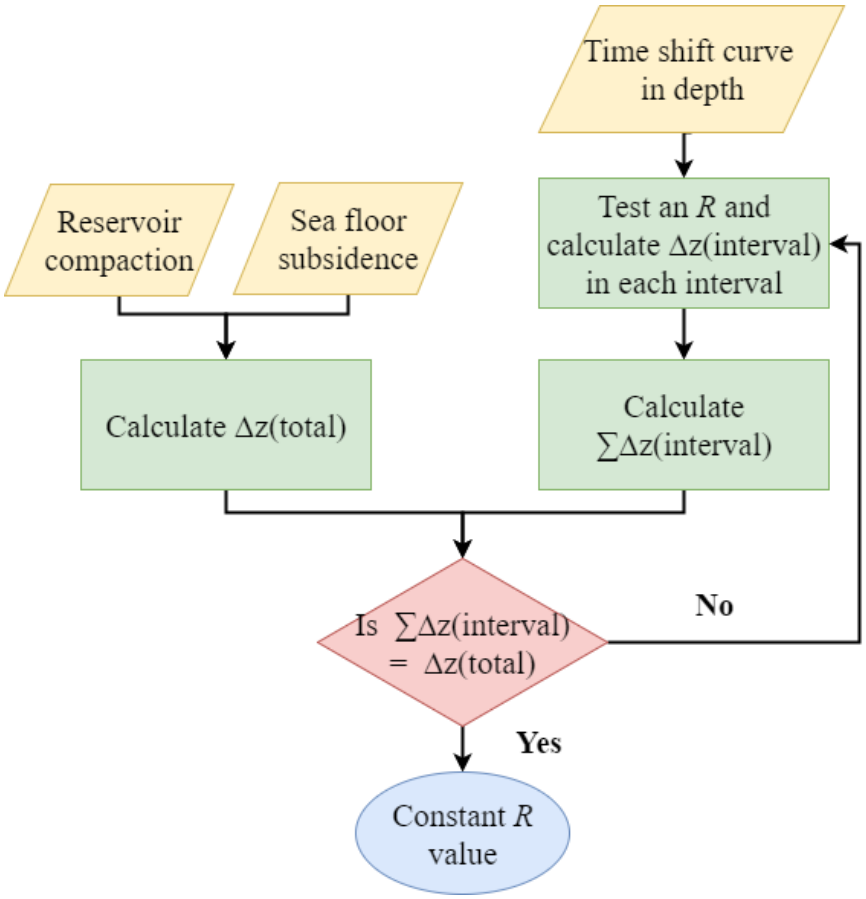

Figure 4.10: Workflow diagram for estimating the constant R factor from total overburden thickness change and 4D data, equation 3.13.

By estimating the thickness change for a variety of different R factors one can establish R as a function of thickness change. The function is dependent on the time shift curve, and will therefore vary for all focus areas. By combining equation 3.16 and equation 3.13, an expression for reservoir compaction as a function of R is established. Here, C is reservoir compaction and S is sea floor subsidence. Overburden is divided into N intervals, where i is each interval;

$$C(R) = -\left(\sum_{i=1}^{N} \frac{\Delta t_{int,i} \cdot v_{p,i}}{2(1 + R_i)} \right) + S \tag{4.4}$$

Chapter 5

Results

5.1 Overburden Time Shifts

From the correlation between time shift and production activity in 2011 to 2014, it is quite clear that the time shifts are related to production. Figure 5.1 displays the wells that were active between 2011 and 2014, the entire period or parts of it. The circular marks are colored by well type, where pink represents producers and orange speaks for injectors. The size is determined by the volume of fluid that is produced or injected. It is clear that there are many more active producers than injectors in this period. On the other hand, the injectors have in general injected a larger volume per well than the producers have produced. The two black circles in Figure 5.1 marks the focus areas for the negative time shift, and the white circle shows the focus area that has been depleted. There are nine producing wells within the white circle and at the boundary of it. This further confirms that the positive time shift is real and indeed represents a production-induced slow-down because of compaction and/or fluid substitution.

Figure 5.2 shows a cross section of the 4D seismic time shifts from inline 560, it crosses the field from NE-SW as marked on the map in Figure 4.1. The horizontal black lines are the horizons that have been studied, they were also displayed in Figure 4.2. The lowermost black line is the top reservoir and the uppermost black line represents the water bottom. The white circle marks the approximate location of the focus areas. Cross sections across the field show different signatures and time shift values for the overburden, therefore, Figure 5.2 is only representative of this specific inline and not the Ekofisk Field as a whole. Notice the drastic speed up present in most of the section shallower than 1000 ft. This is most likely an artifact of

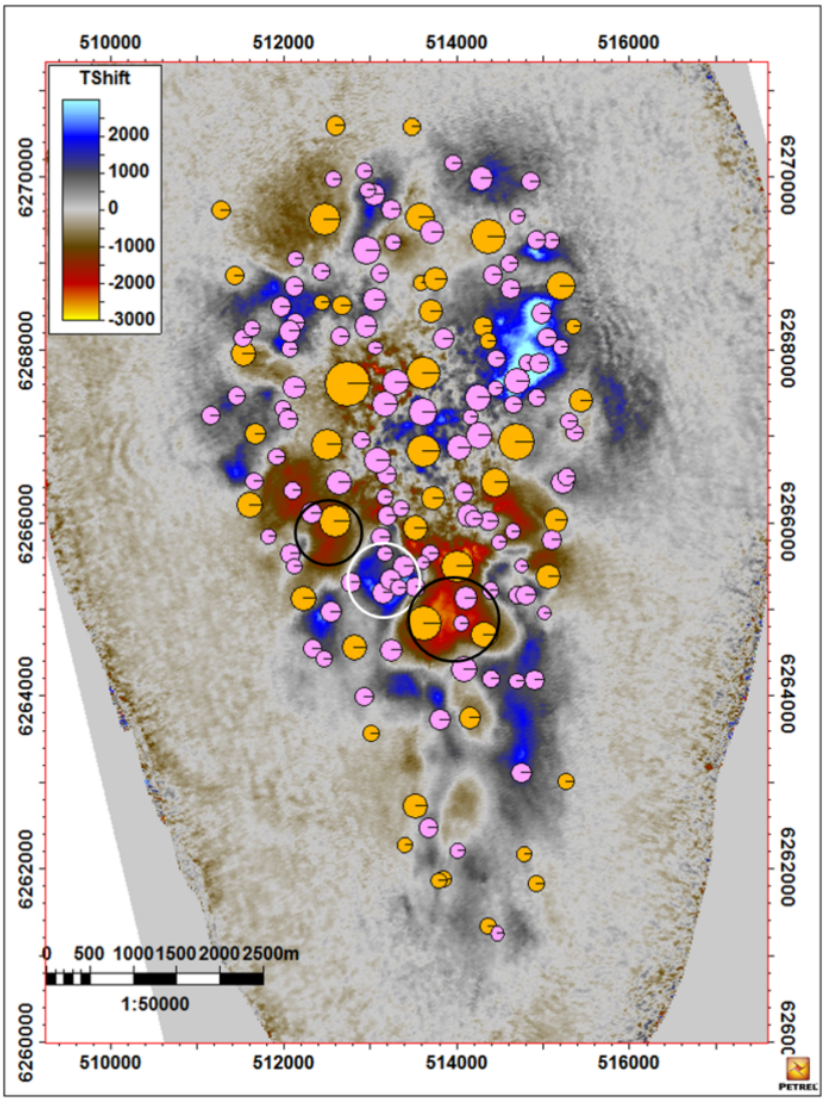

Figure 5.1: Wells active at Ekofisk Field in the period 2011 to 2014. Color by well type; orange are injectors, pink are producers. Size by the volume produced or injected. White circle is the depletion zone, the black circles mark the injection zones.

poor imaging, acquisition and processing; the surfaces are very shallow, leading to large offsets and fewer traces, this is further discussed in Section 6.1.

Further, the time shifts in the majority of overburden of this cross section are slightly negative. This is probably an effect of time shifts being cumulative, and the interval closest to the sea floor having a strong negative time shift. In the depletion zone, the time shift peaks around top reservoir (marked by the lowermost black line). Into the reservoir the time shifts in the depletion zone decrease in absolute value but are still positive, implying a speed-up in the reservoir. This is expected since the reservoir is believed to undergo compaction caused by depletion. The time shift in the injection zones therefore peak deeper into the reservoir, as they are becoming

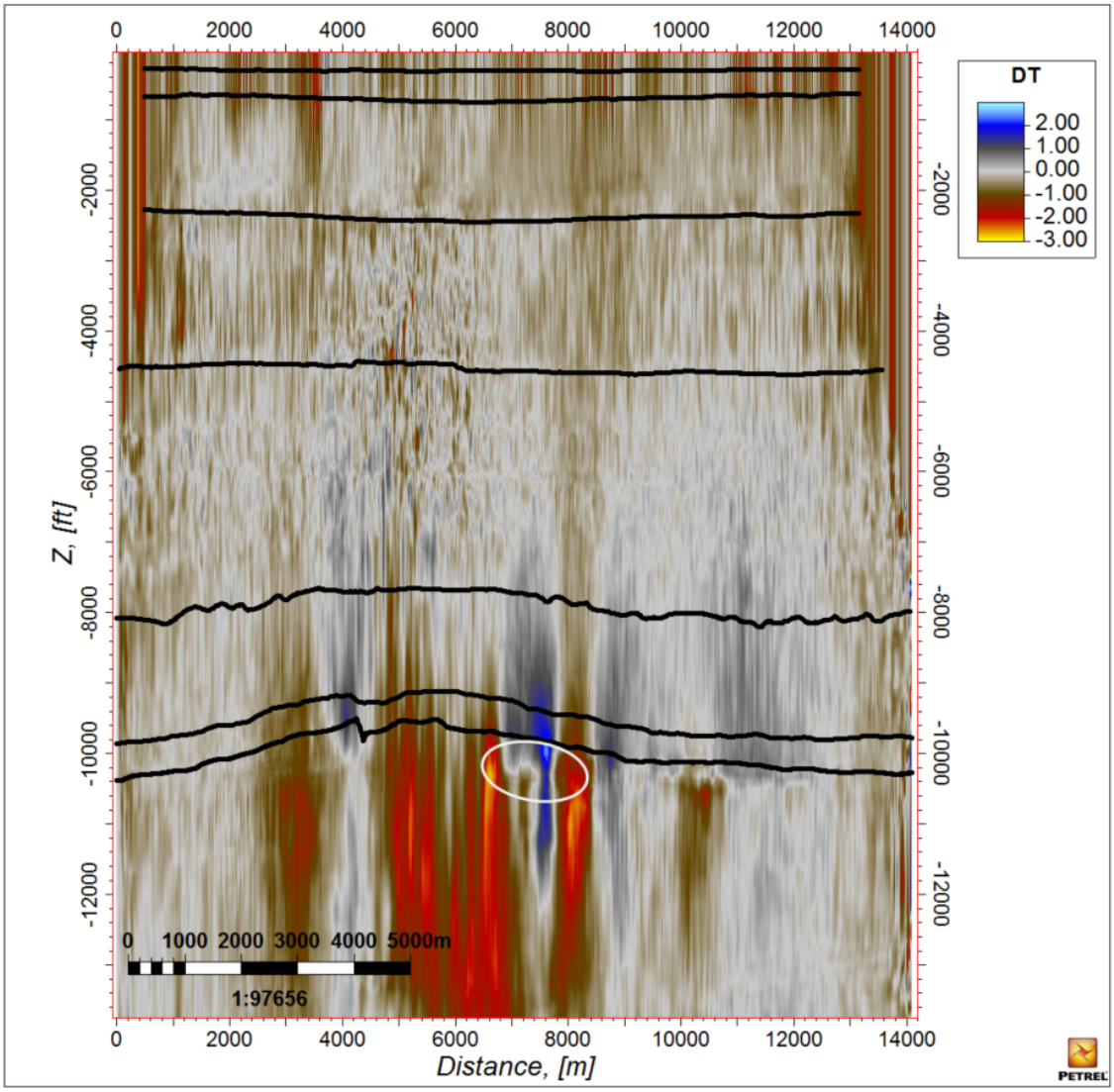

Figure 5.2: Cross-section of the time shift map along inline 560. The black horizontal lines are the studied horizons, the white circle marks the approximate location of the focus areas.

more and more negative.

Time shifts are averaged between all pseudo wells for every horizon at each focus area, marked in Figures 4.2 and 5.2. This is believed to make the resulting time shift curve quite robust. The time shift in depth for the three focus areas can be seen in Figure 5.3. The vertical scale is depth below sea floor, and the reservoir is located at 3000 m depth. The seismic shallower than the red horizontal line marked ”Seismic limit” is considered not to be trusted because of poor imaging.

The negative time shift leap directly below the sea floor of almost -0.4 ms applies for all three time shift curves, although the drop is smaller in injection zone 1. This negative peak in time shift close to the sa floor is also observed on the cross-section in Figure 5.2. The main

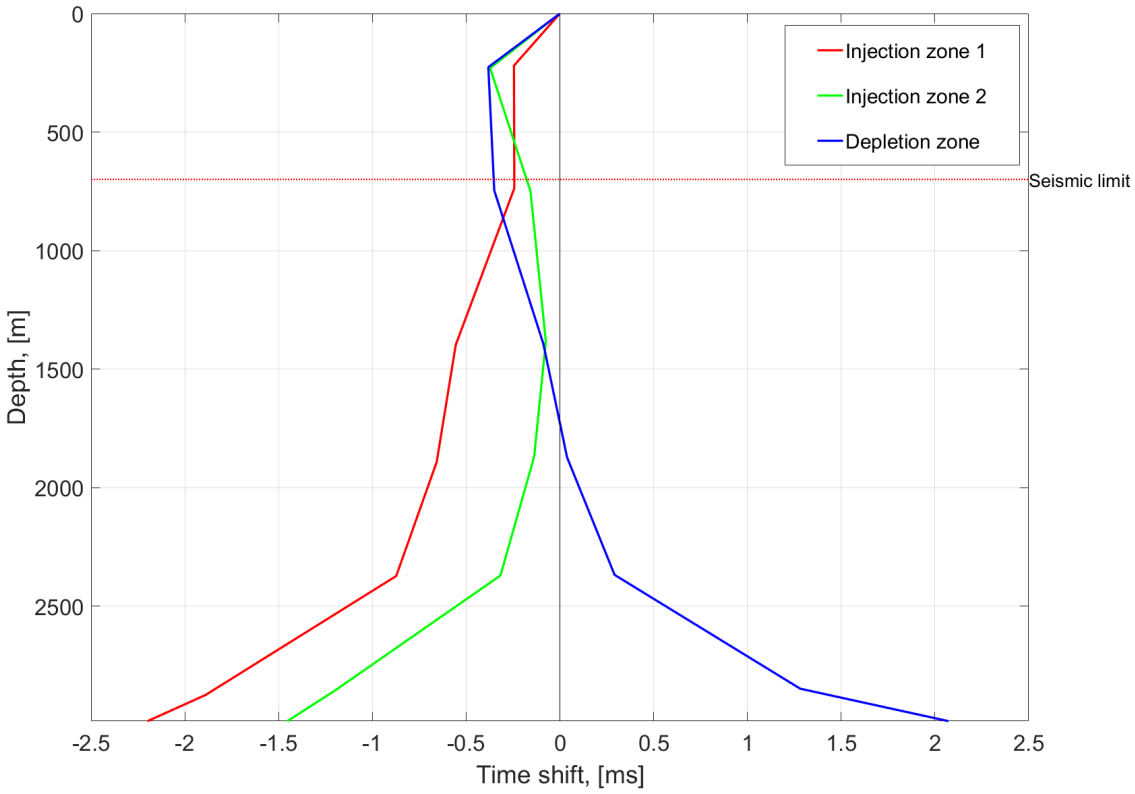

Figure 5.3: Time shift in depth for injection zone 1, injection zone 2 and the depletion zone in colors red, green and blue, respectively. The red line "Seismic limit" marks the depths that are too shallow to trust the seismic because of poor seismic.

explanations will be discussed further in Section 6.1. From 226 m and deeper the time shift curve for the depletion zone is continuously getting more positive. This implies that if the negative time shift leap close to sea floor was not present, the time shift would all be positive and consistently increase in depth, as expected. An important observation is also that the time shift is noticeably small until around 2400 m, implying that the clear majority of the production-induced changes take place within approximately 600 m of the top reservoir. Injection zone 1 and the depletion zone have remarkably similar time shift curves, excluding the opposite sign. The time shifts in injection zone 1 and 2 have similar slopes and trends deeper than 1300 m. The time shift at top reservoir is presented in Table 5.1.

Time strain is estimated numerically for all three focus areas from equation 3.8 and is presented in Figure 5.4. The time strain curve in the depletion zone reveal that the majority of the slow-down comes from the last 600 m above the reservoir.

Table 5.1: Time shift at top reservoir at each of the focus areas.

Focus area	Time shift at top reservoir, [ms]
Depletion zone	2.07
Injection zone 1	-2.26
Injection zone 2	-1.48

The time strain curves in the injection zones demonstrates that the speed-up in the overburden here is not distributed in the same uniform trend as in the depletion zone. In injection zone 1 there is a speed-up in the shallow overburden, which decrease to zero and then increase again towards top reservoir. In practice this means that traveltime in the overburden of an injection zone does not change uniformly in depth. This indicates that the time shift effects in the injection zones are more complex than in the depletion zones. The time strain curves in injection zone 1 and 2 have quite similar trends.

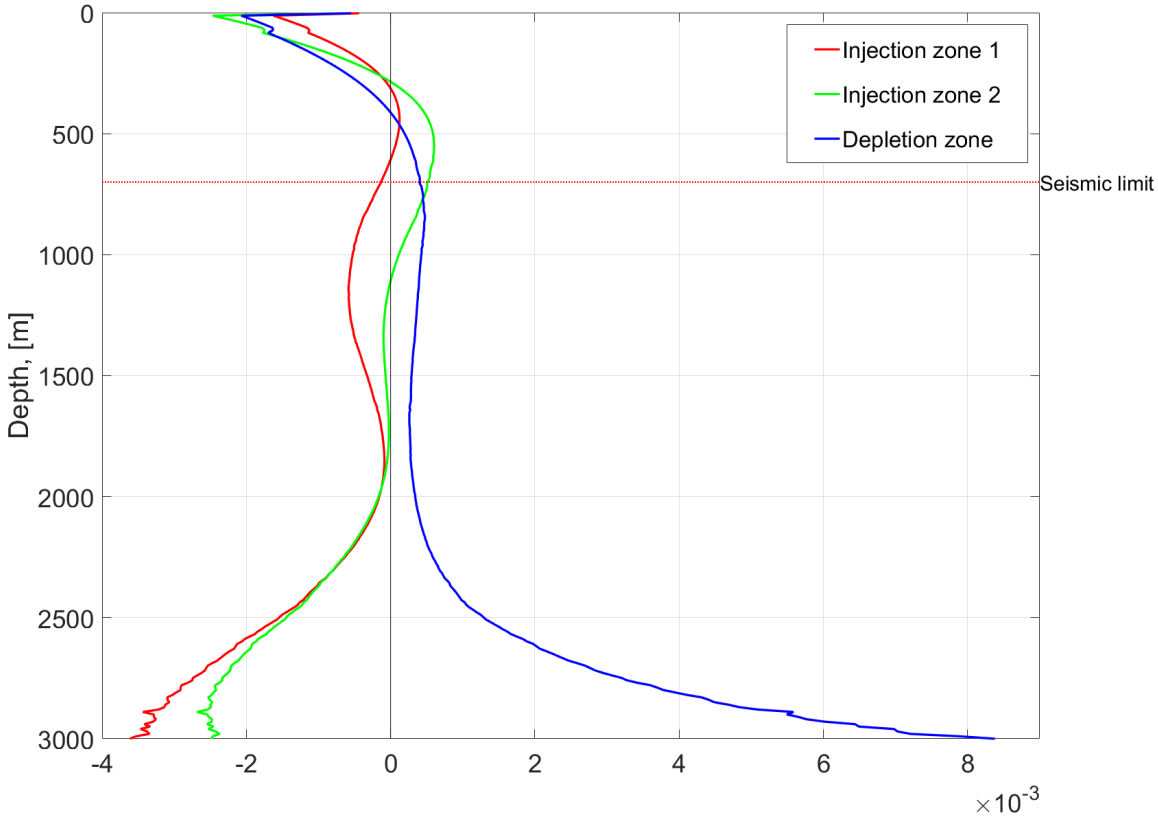

Figure 5.4: Time strain in depth for injection zone 1, injection zone 2 and the depletion zone in colors red, green and blue, respectively.

5.2 Sea Floor Subsidence

Figure 5.5 is the sea floor subsidence map generated by subtracting the 2014 sea floor map from the 2011 sea floor map, which were presented in Figure 4.4. Positive values on the map imply increased subsidence between 2011 and 2014. The pseudo wells in the injection zones are marked as black symbols in Figure 5.5, while the pseudo wells in the depletion area are marked as white symbols. Both the subsidence map (Figure 5.5) and sea floor maps (Figure 4.4) show a uniform subsidence bowl towards the center of the field. This is in contrast to the localized compaction that was observed at top reservoir. This is explained in (Andersen, 1995) by the averaging effect of the spreading in the overburden. However, this implies that the relationship between subsidence and compaction naturally varies across the field.

The subsidence is measured at each of the pseudo wells and further averaged to represent each of the focus areas. The average subsidence at the focus areas that are used further in the calculations are given in Table 5.2. The values are negative because positive direction is set to be upwards. The subsidence is slightly larger for the depletion zone than in the injection zones. However, the depletion zone and injection zone 2 are also closer to the center of the bowl, which is also a likely explanation to why the values are larger than in injection zone 1.

Table 5.2: Subsidence of the sea floor at each of the focus areas.

Focus area	Subsidence, [m]
Depletion zone	-0.33
Injection zone 1	-0.24
Injection zone 2	-0.29

In the depletion zone the subsidence was estimated to be 0.33 m. This rate is slightly lower than it was for the 2008 to 2011 period. This might be caused by the poor quality of the 2014 bathymetry; the weather was bad and the survey was too narrow to acquire enough data that could be used as reference points for zero subsidence, as pointed out in Section 4.2 referring to Figure 4.4a. Therefore, GPS data from the center of the Ekofisk Field below the hotel platform is studied in order to quality check the subsidence from the 2014 bathymetry data. The subsidence appeared reasonable from the analysis and will be used further in the report. The data and discussion are presented in Section A.5 in the Appendix.

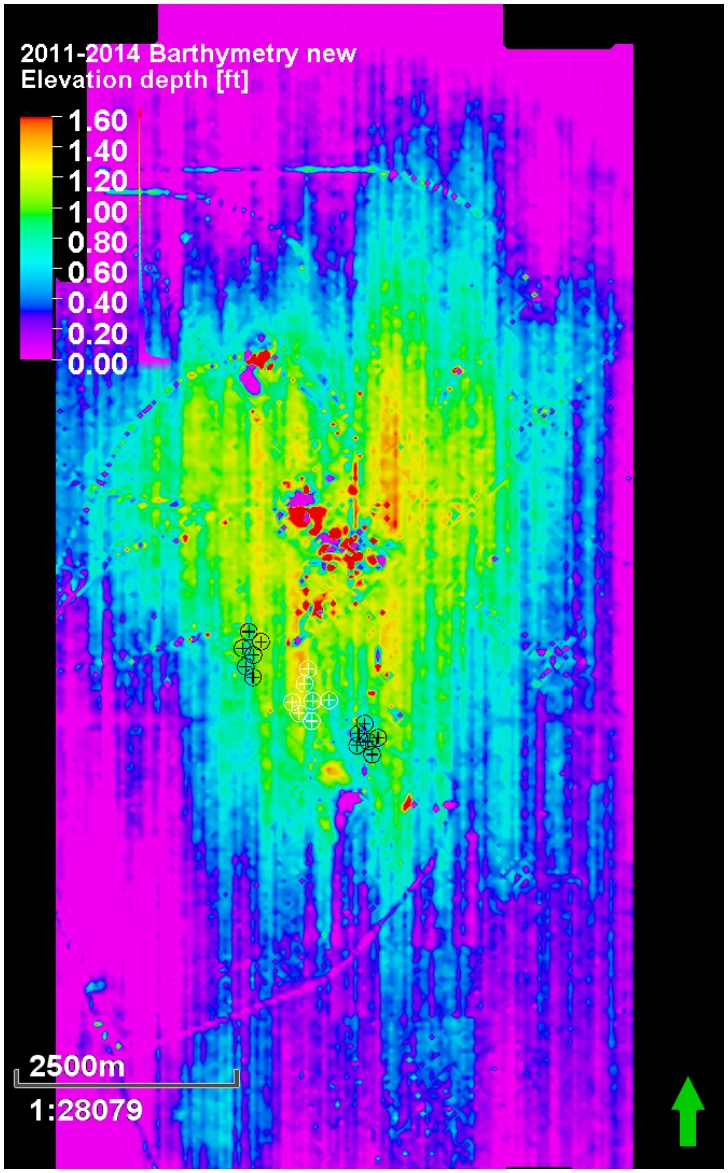

Figure 5.5: Subsidence map of the sea floor between 2011 and 2014. Black symbols are pseudo wells in injection zone 1 and 2. White symbols are pseudo wells in the depletion zone.

5.3 Overburden Velocity Trend

In order to estimate synthetic time shifts from equation 3.11, the velocity in the overburden was established from sonic logs of six exploration wells around the Ekofisk Field. Velocity measurements starts as shallow as 570 m deep, which is an advantage of using the exploration wells. Figure 5.6 shows the velocity curve in the overburden. The red line is the velocity at every 0.3048 m (every ft) calculated from the average of the six exploration wells. Further, the velocity was averaged within the interval determined by the step, z, which was every 10 m. The blue line is the average velocity in each interval. The velocity is especially fluctuating the last 100 m above the reservoir. The velocity drops drastically around 1300 m, this correlates to an overpressured zone that is clear from the averaged effective stress curve in the overburden demonstrated in Figure A.1 in Section A.3 in the Appendix.

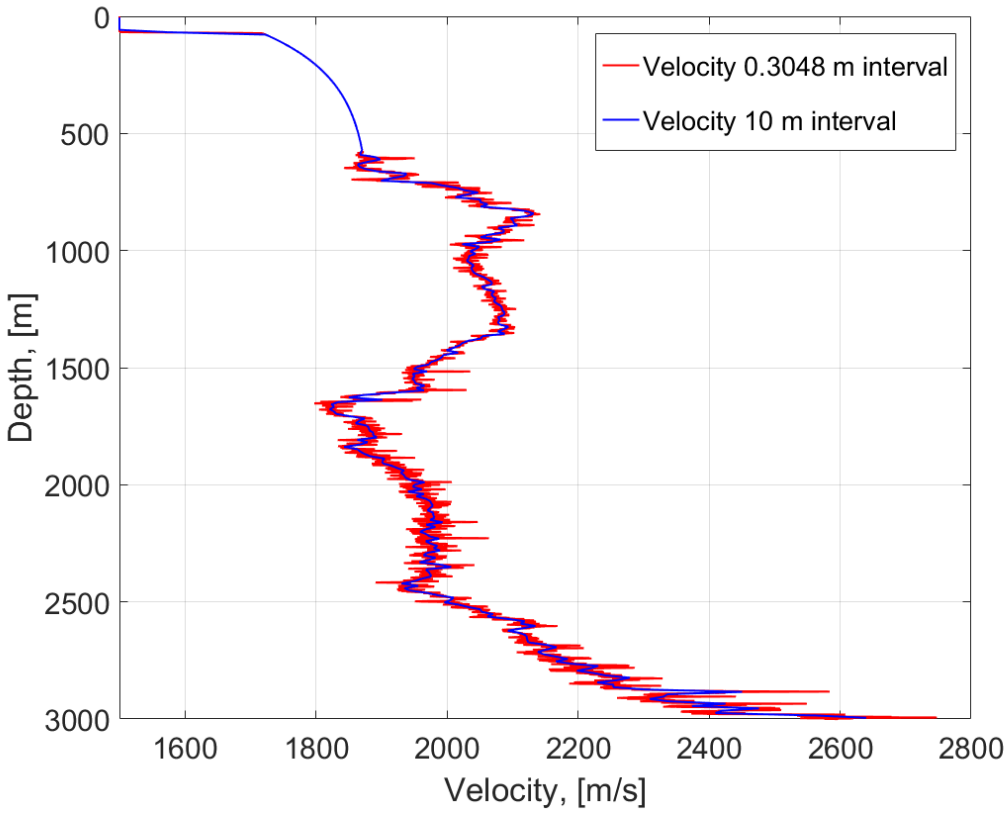

Figure 5.6: Velocity trend in the overburden. Red curve is the average velocity measured every ft (0.3048 m) and blue curve is the average velocity at every 10 m.

5.4 Geertsma's Nucleus of Strain Model for One Reservoir

The analytic solution to the displacement field along the center-line of a reservoir from Geertsma's model is given in equation 3.18. The equation is simulated for different reservoir radii and pore pressure changes to understand how this affects overburden strain. The input parameters in the simulations are presented in Table 5.3 and the elastic moduli for the simulation are presented in Table 4.2 for $\phi = 0.35$. The simulations are performed for a variety of different pore pressure changes and reservoir radii.

Table 5.3: Input parameters and values in the simulations of the analytic Geertsma equation, equation 3.18.

Parameter	Description	Value
D	Depth to top reservoir, [m]	3000
R	Reservoir radius, [m]	500, 1000, 1500, 2000, 2500
h	Reservoir height (pay thickness), [m]	300
Δp_f	Pore pressure change, [MPa]	1, 3, 5, 7, 9
ν	Poisson's ratio	0.2

Figures 5.7, 5.8 and 5.9 displays sea floor subsidence, compaction at top reservoir and thickness change of the overburden, respectively, plotted as a function of pore pressure change for different reservoir radii. The subsidence of the sea floor, Figure 5.7, is noticeably sensitive to reservoir radius. In other words; for the same magnitude of pore pressure change, the subsidence will manifest itself remarkably differently depending on reservoir size. Subsidence is very small regardless of pore pressure change for small reservoirs. But for larger reservoirs, the subsidence varies substantially with pore pressure change.

From the reservoir compaction in Figure 5.8, it is clear that compaction rate is not as sensitive to reservoir size as the subsidence is, although it does increase for larger pore pressure change and radius. This means that for two reservoirs with same pore pressure depletion but different reservoir radius; compaction at top reservoir might be similar, but there will be a distinct divergence in subsidence rates at the sea floor.

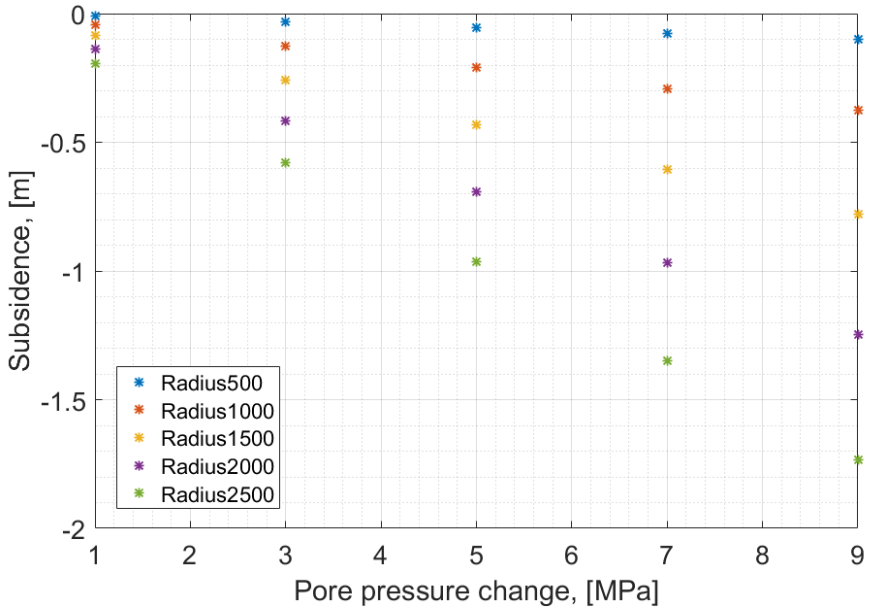

Figure 5.7: Subsidence of the sea floor above the center of a depleting disk-shaped reservoir, from equation 3.18.

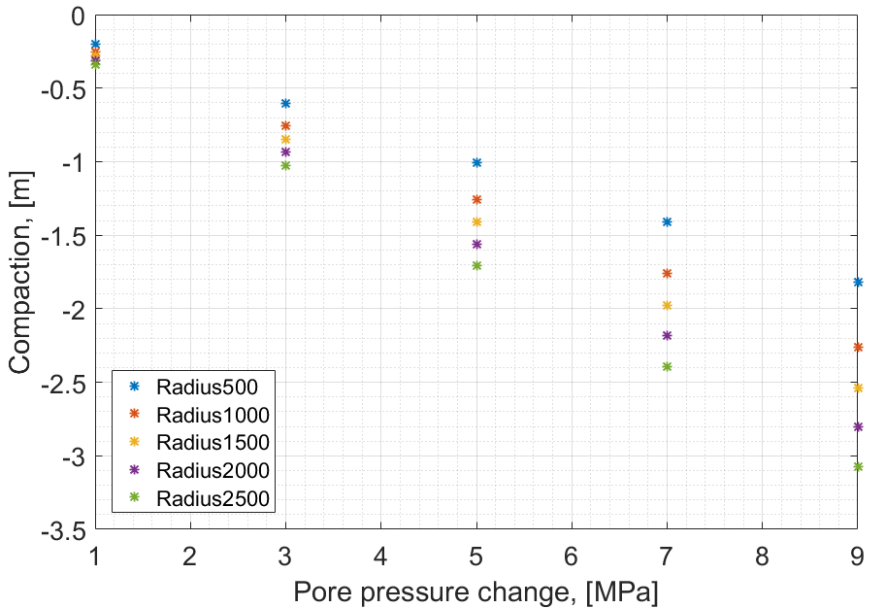

Figure 5.8: Compaction at top reservoir above the center of a depleting disk-shaped reservoir, from equation 3.18.

Figure 5.9 shows the thickness change of the overburden calculated from reservoir compaction and sea floor subsidence, from equation 3.16. While both compaction and subsidence rates were consistently increasing for larger reservoirs, the same is not observed for the thickness change of the overburden. For these exact input parameters, the thickness change at any pore pressure change is biggest for the reservoir with radius $R = 1000m$. This is dependent on the relation between reservoir radius and burial depth, R/D, as the ratio between maximum subsidence and compaction is determined by the ratio between reservoir depth and reservoir radius, (Geertsma, 1973). Naturally subsidence is larger for shallower reservoirs, as the reservoir is less shielded by overburden rocks, but compaction is not as sensitive. Consequently, the total thickness change of the overburden is larger for shallower buried reservoirs.

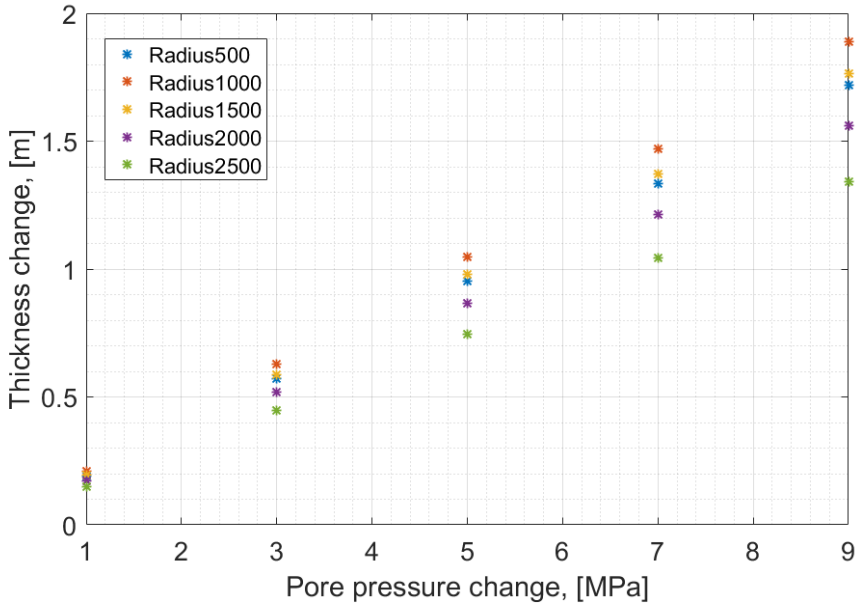

Figure 5.9: Thickness change of the overburden above the center of a depleting disk-shaped reservoir, from subsidence of the sea floor and compaction at top reservoir using equation 3.18.

The displacement and strain are extracted along the center-line of a depleting reservoir while the radius is kept constant at $R = 500m$, and the magnitude of the pore pressure change varies. This is given below in Figures 5.10 and 5.11, respectively. Figure 5.10 shows the displacement in the overburden, reservoir and overburden. Figure 5.11 displays the strain in the overburden. From both plots it is obvious that the displacement and strain change linearly with pore pressure change. Hence, an increased pore pressure depletion in a reservoir will not change the distribution of displacement or strain in the overburden, only the magnitude of it.

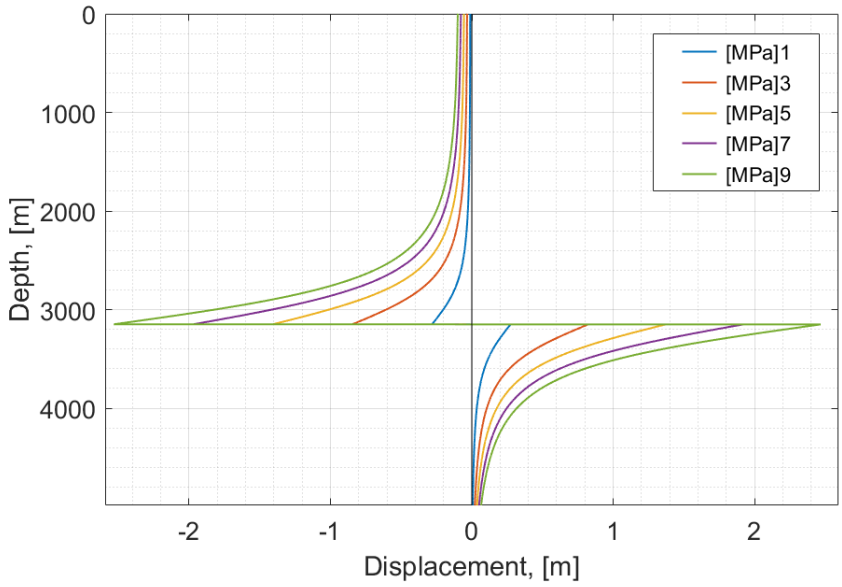

Figure 5.10: Displacement along the center-line of a depleting reservoir for a constant reservoir radius of 500 m and varying pore pressure change. Top reservoir is at 3000 m.

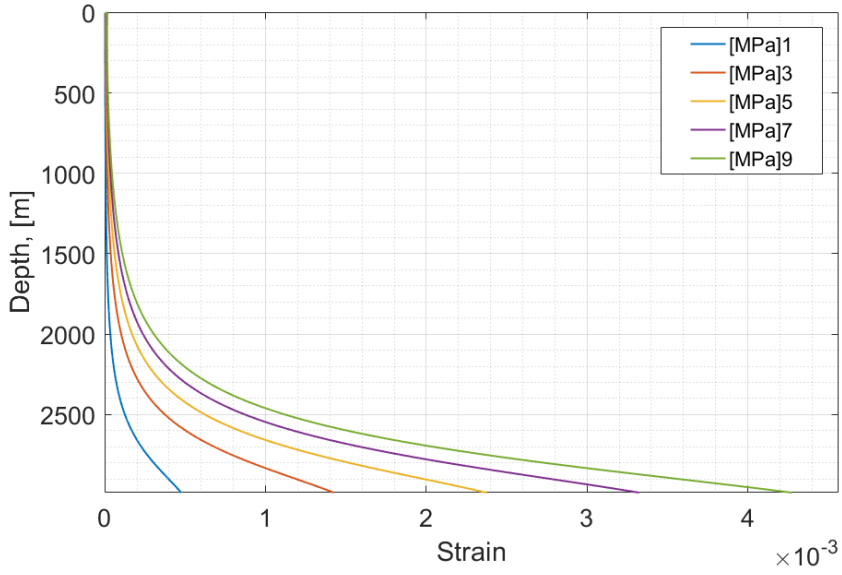

Figure 5.11: Strain along the center-line of a depleting reservoir for a constant reservoir radius of 500 m and varying pore pressure change. Top reservoir is at 3000 m.

Displacement and strain for constant pore pressure depletion of 5 MPa with varying reservoir radius are shown in Figures 5.12 and 5.13, respectively. Figure 5.12 shows vertical displacement in overburden, reservoir and underburden. The distribution of displacement varies with reservoir radius; for smaller radii the displacement is concentrated close above the reservoir, while for larger reservoirs the displacement is distributed more evenly. The magnitude of

displacement is also larger for larger reservoir radii. The same is observed for the strain in the overburden, Figure 5.13, where the strain is more evenly distributed for larger reservoir radii. This indicates that if Geertsma's nucleus of strain model is applied to estimate strain distribution in the overburden, it is essential to apply an appropriate reservoir radius.

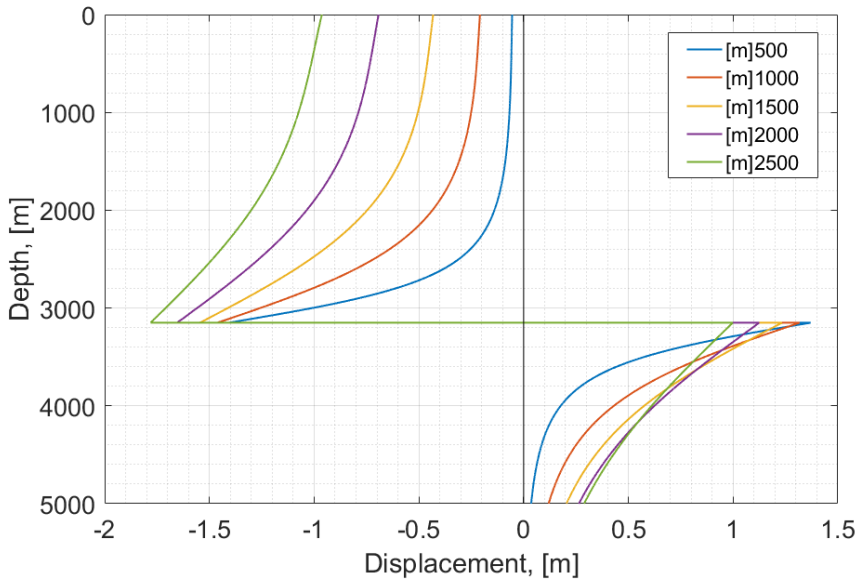

Figure 5.12: Displacement along the center-line of a depleting reservoir for a constant pore pressure depletion of 5 MPa and varying reservoir radii. Top reservoir is at 3000 m.

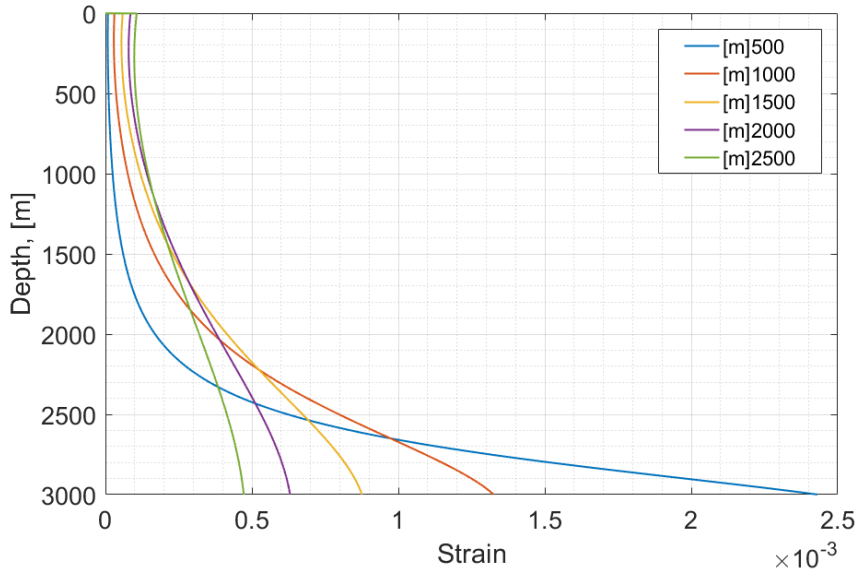

Figure 5.13: Strain along the center-line of a depleting reservoir for a constant pore pressure change of 5 MPa and varying radii. Top reservoir is at 3000 m.

5.5 Depth-Dependent R Factor

5.5.1 Superposition of Geertsma's Nucleus of Strain Model

The system where three independent reservoirs were superimposed to modelt the Ekofisk Field is sketched in Figure 4.7. The model consists of one large reservoir undergoing a pore pressure change, and two smaller reservoirs within the large reservoir with independent pore pressure changes. In addition, Figure A.2 in section A.4 in the Appendix was an alternative model that had three bordering reservoirs next to each other so the boundaries were in contact. The details and results from this method is presented in Section A.4. In practice it required multiple simulations and testing to conclude on a model that could be used to estimate strain in the overburden.

5.5.2 Strain and Displacement from Model 1

The displacement field from model 1 in the overburden, underburden and sideburden is demonstrated in Figure 5.14, the figure is turned sideways to make it larger and easier to study. A close-up of the displacement field in the overburden is given in Figure 5.15. Notice that these plots have different color map scales. It is clear that the displacement field is not symmetric above and below the reservoir, but larger above the reservoir than below it. The subsidence of the sea floor clearly manifests itself around the center of reservoir 1, implying that this reservoir is causing the subsidence bowl. This correlates well to the observations of subsidence evident in Figure 5.7; that the subsidence is hardly noticeable for small reservoirs, but can be quite substantial for large reservoirs. In other words, subsidence is very sensitive to reservoir radius.

The subsidence also fits the observed subsidence at the Ekofisk Field, Figure 5.5, where the subsidence is at its largest in the center of the field. But the compaction around the top reservoir is larger for reservoir 2 than for reservoir 1, see Figure 5.15. Moreover, the compaction right above reservoir 3 is close to 0, yet the sea floor is subsiding because of reservoir 1. This implies that the overburden is shrinking above reservoir 3, stretching above reservoir 1 and stretching even more above reservoir 2. Safe to say multiple effects take place in the overburden.

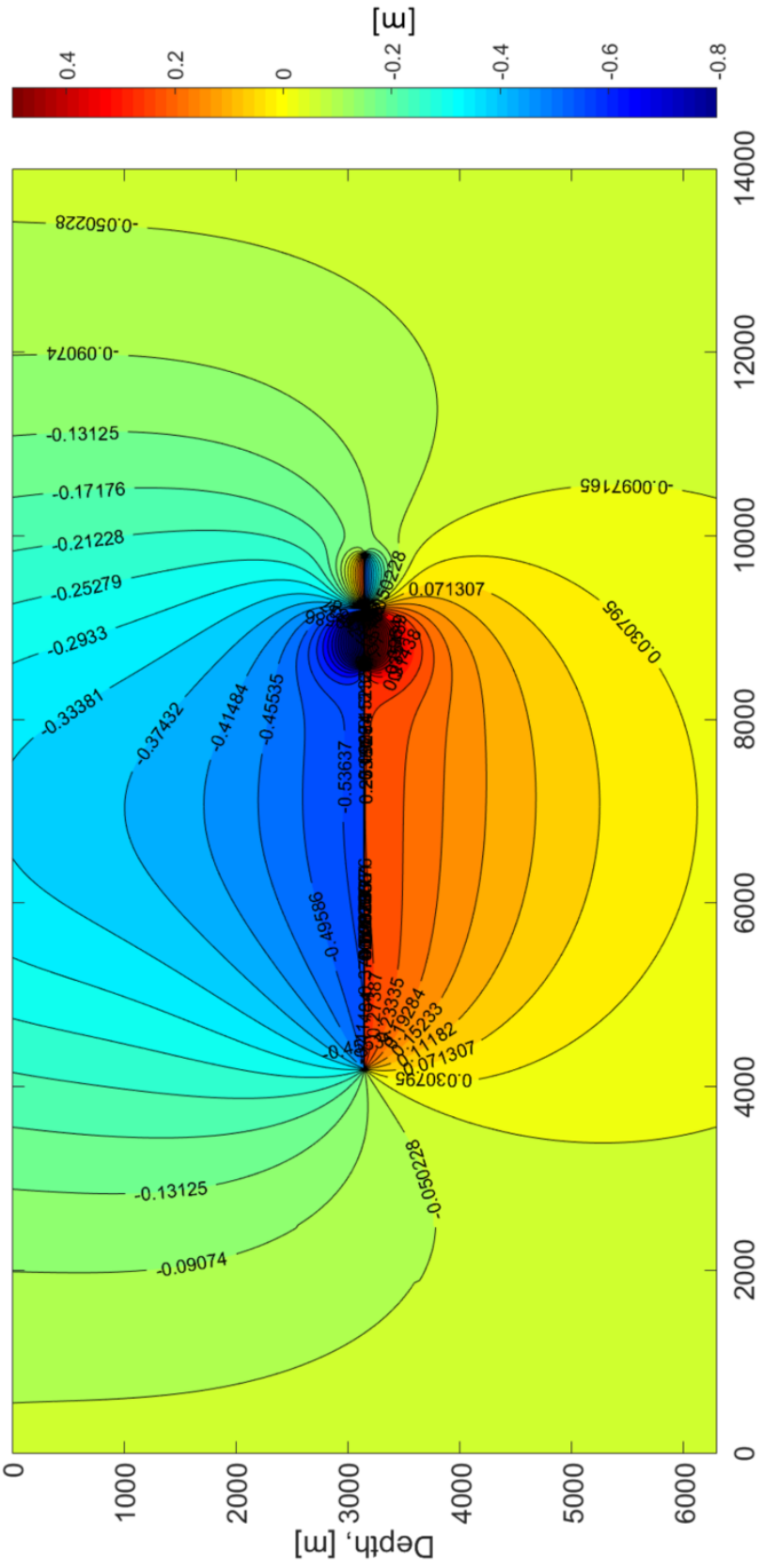

Figure 5.14: Displacement field from model 1, limit of the y axis is at 6200 m. The contour labels are in the unit meter.

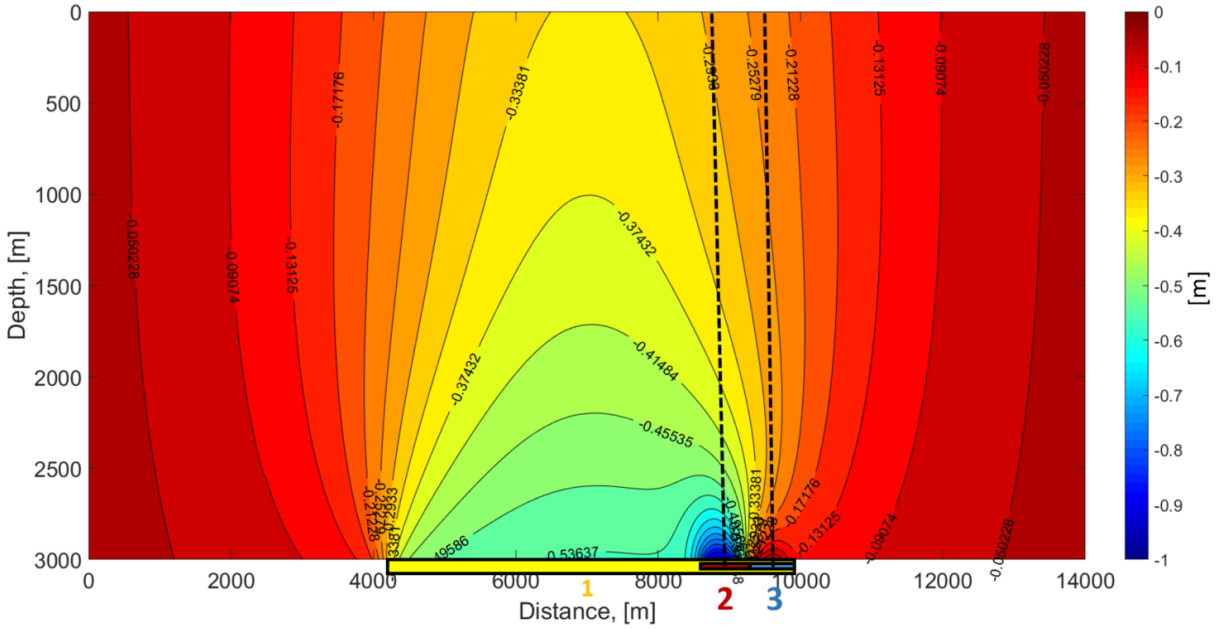

Figure 5.15: Displacement field from model 1, limit of the y axis is at 3000 m. The contour labels are in the unit meter. Reservoir 1, 2 and 3 are marked in the colors yellow, red and blue, respectively. Dotted lines show the profile where displacement and strain was extracted.

Displacement and strain are extracted along the center line of reservoir 2 and 3, as demonstrated by the dotted lines in Figure 5.15. They are presented in Figures 5.16 and 5.17 for reservoir 2 and 3, respectively. Notice the difference in scale for the plots. The displacement at 0 depth represents the subsidence of the sea floor, which is approximately -0.28 m in Figure 5.16a. The displacement at 3000 m represents the compaction at top reservoir, which is around -0.94 m for reservoir 2 in model 1. Subsidence at sea floor, compaction at top reservoir and thickness change of the overburden is presented in Table 5.4 for model 1. The overburden thickness change is estimated from equation 3.16.

Table 5.4: Subsidence of the sea floor, compaction at top reservoir and total thickness change of the overburden from simulations of Geertsma's nucleus of strain model above injection and depletion zones.

Reservoir in simulation	Focus area being simulated	Subsidence, [m]	Compaction, [m]	Thickness change, [m]
2	Depletion zone	-0.28	-0.94	0.66
3	Injection zone	-0.24	-0.04	-0.20

The strain above the depletion zone (reservoir 2), Figure 5.16b, is distinctly larger closer to the reservoir; shallower than 1800 m the strain is microscopic. This suggests that majority of the deformation of the overburden takes place within around 500 m of the top reservoir. Moreover, the strain is quite large. Both displacement and strain in Figure 5.16 have a uniformly increasing trend with depth and are escalating rapidly close to the top of the reservoir, which was also observed for the time shift in the depletion zone from Figure 5.3.

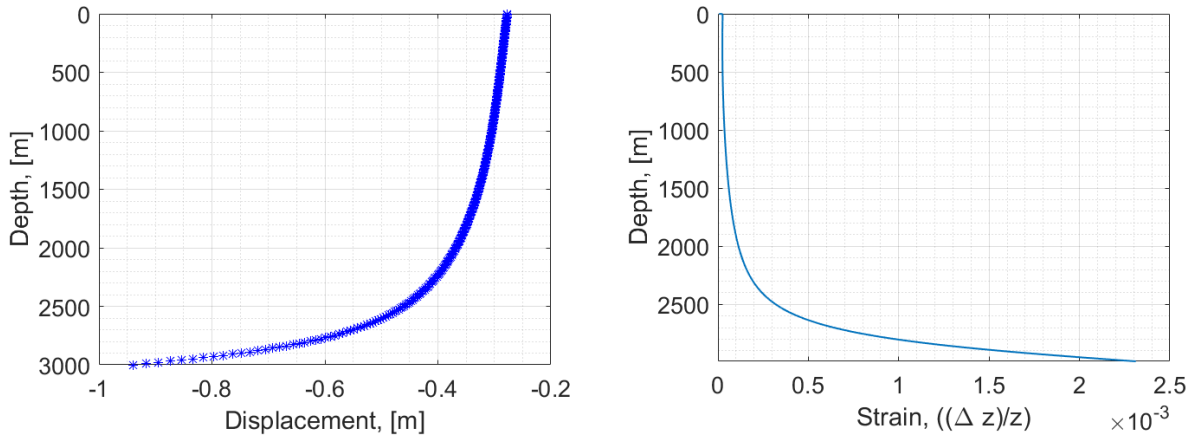

(a) Displacement above the center of reservoir 2. **(b)** Strain above the center of reservoir 2.

Figure 5.16: Displacement and strain above the center of reservoir 2 from model 1.

Reservoir 3 represents the injection zone. The displacement and strain are displayed in Figure 5.17. From the strain displayed in Figure 5.17b it is clear that the overburden is compacting deeper than 2500 m, while shallower than this the rock is stretching marginally. The strain becomes slightly more negative from sea floor until 2250 m, where it has the largest negative value. An important observation is that the strain above the injection zone is much smaller than the strain above the depletion zone (Figure 5.16b). Correspondingly, the thickness change above the injection zone is much smaller than above the depletion zone, see Table 5.4.

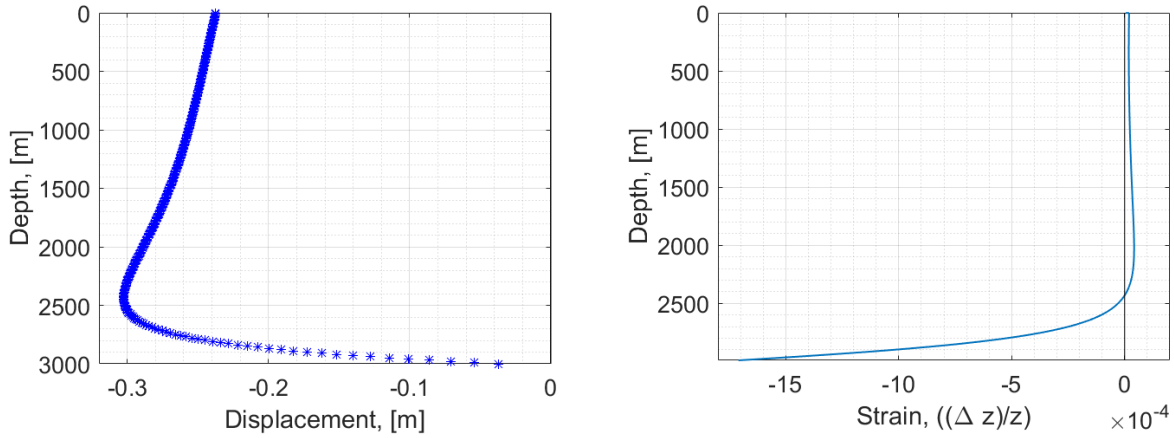

(a) Displacement above the center of reservoir 3. **(b)** Strain above the center of reservoir 3.

Figure 5.17: Displacement and strain above the center of reservoir 3 from model 1.

5.5.3 Synthetic Time Shifts

Vertical strain (ε_z) in Figures 5.16b and 5.17b were used to calculate synthetic time shifts. The former represents strain above a depleting reservoir and the latter models strain above a repressurization zone. The synthetic time shifts were compared to the observed time shifts using equation 4.3. The time shifts are presented in each interval and as a cumulative time shift. The synthetic time shift is plotted for R factors between 1 and 15, in increments in R of 2, and are displayed with the observed time shift. More R values were tested, but are not demonstrated in the figures for illustrating purposes. The cumulative time shift is established by a cumulative sum for the intervals downward in depth. Figure 5.18 is the time shift in each interval in the depletion zone. From the plot it is clear that near the top of the reservoir the best fit is an R factor of 2 and 3, while shallower the optimal R is considerably larger. The synthetic time shifts for each interval have some small fluctuations around 2800 m, see Figures 5.18 and 5.21, which is caused by the estimated velocity in each interval. From the velocity curve in depth, Figure 5.6, it is clear that the velocity is very varying for the deepest 100 m above the reservoir.

The cumulative time shift is shown in Figure 5.19 for reservoir 2 simulating the depletion zone. Shallower than 2000 m there is no R that fit the observed time shift, which is marked as a thicker black line, as the observed time shift is negative this shallow, which was discussed in Figure 5.3. From Figure 5.19 the best match to the time shift at top reservoir is from $R = 2$.

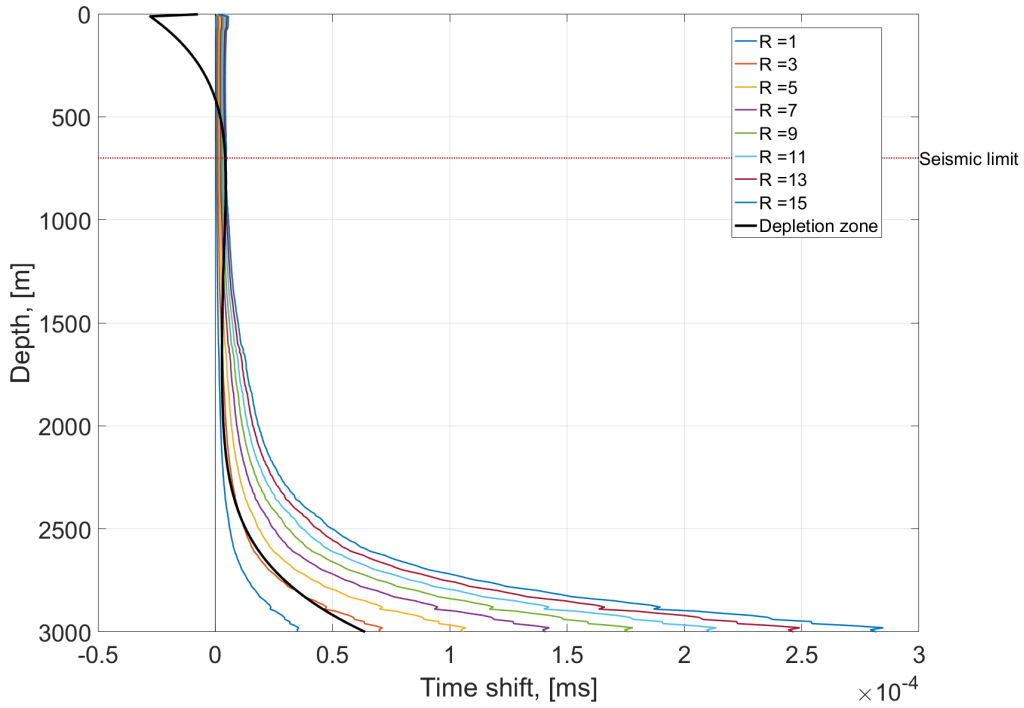

Figure 5.18: Synthetic time shift in each interval, from strain in Figure 5.16b. The black line is the observed time shift in each interval in the depletion zone.

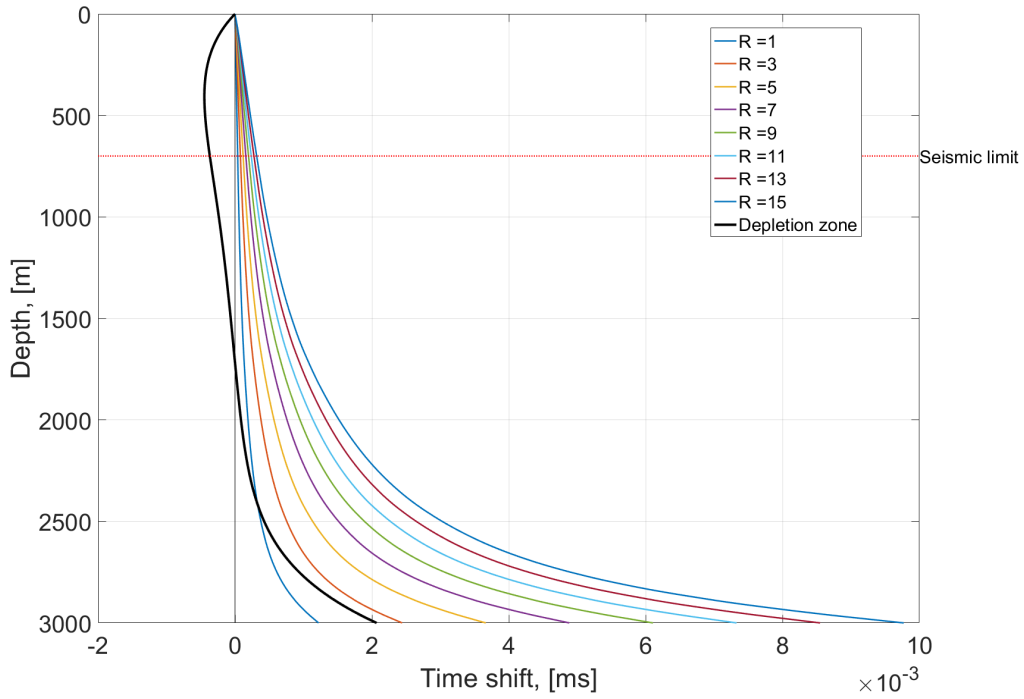

Figure 5.19: Cumulative synthetic time shift, from strain in Figure 5.16b. Black line is the observed time shift in the depletion zone.

The R factor that give a synthetic time shift that matches best with the observed time shift in the depletion zones is presented as the optimal R in the given interval in Figure 5.20. From the figure it is clear that R is depth-dependent, with decreasing values in depth. R ranges from 14 shallow to 2 closer to the reservoir. $R = 2$ from 1700 m to 2300 m and then increases to 3. The range in R around 2-3 for top reservoir was also clear from the synthetic time shift in each interval in Figure 5.18. The 4D seismic is not trusted shallower than the seismic limit, therefore the R values are not assumed to be correct here. Within the depth where seismic is trusted (deeper than 700 m), the average R in the overburden from the depth-dependent R is estimated to $R_{Avg} = 5$.

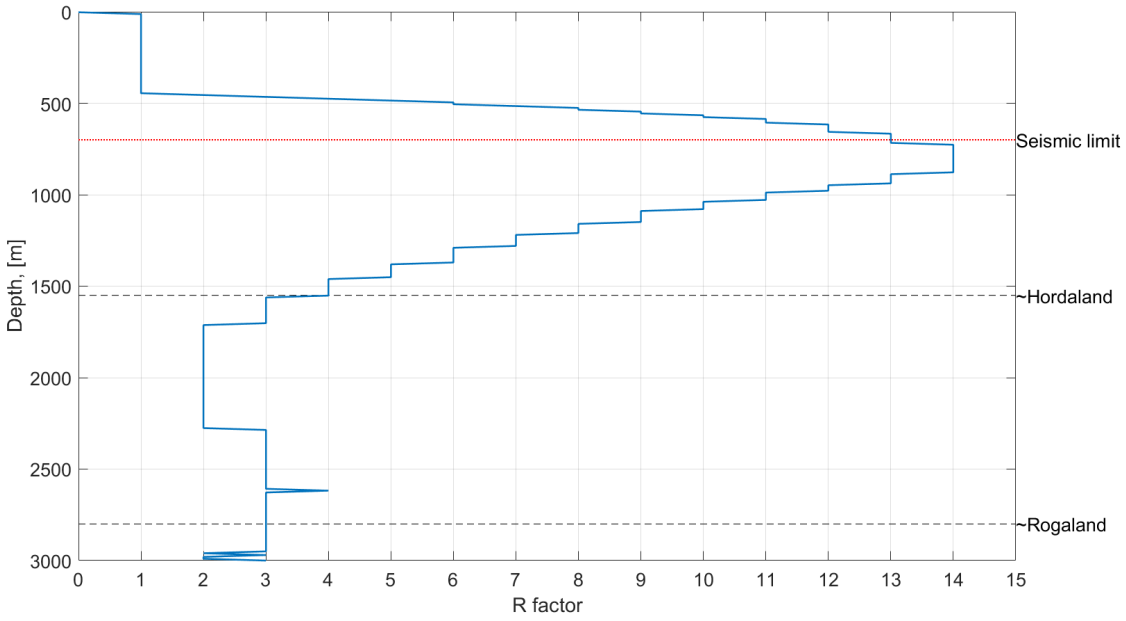

Figure 5.20: R factors from synthetic and observed time shift in each interval. The red dotted line marks where seismic is too shallow to trust because of poor imaging. The top of lithological groups are marked as black dotted lines.

Figures 5.21 and 5.22 displays the synthetic time shifts estimated from the strain in Figure 5.17b representing overburden above an injection zone (reservoir 3). The thicker red and black lines are the observed time shifts in injection zone 1 and 2, respectively. The match between the observed time shifts (black line) and synthetic time shifts (colored lines) is very poor. The strain in the injection zones, Figure 5.17b, demonstrates that most of the overburden is stretching, but the time shift indicates that most of the overburden is indeed compacting. To match R factors between the observed and modelled time shift would require negative R values; as overburden

is stretching from modelling, yet the observed time shift implies a speed-up. Hence, no depth-dependent R is established in the overburden of the repressurization zones from the simulations using the Geertsma model.

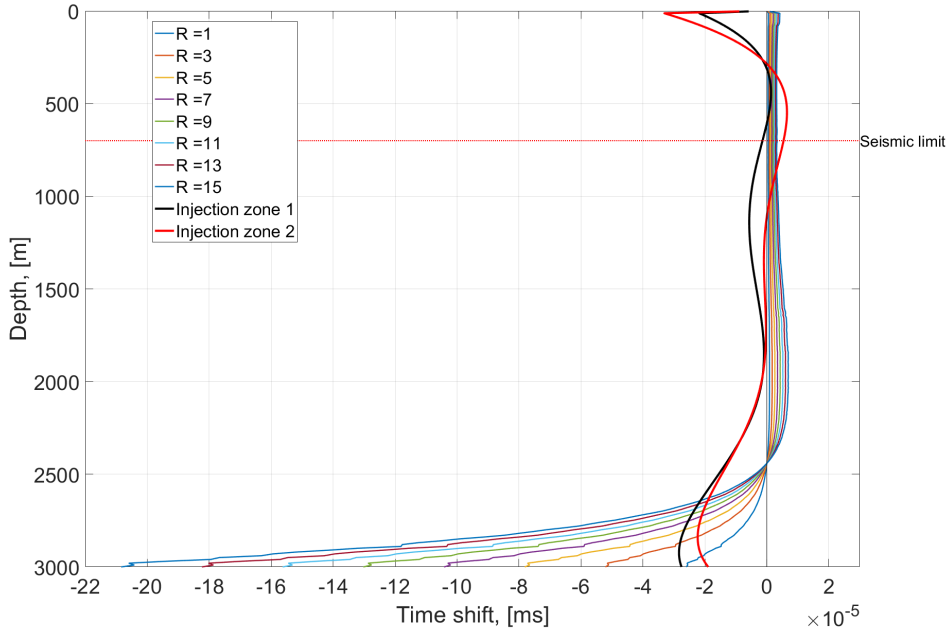

Figure 5.21: Synthetic time shift in each interval, from strain in Figure 5.17b. Black and red lines are the observed interval time shift in the injection zones.

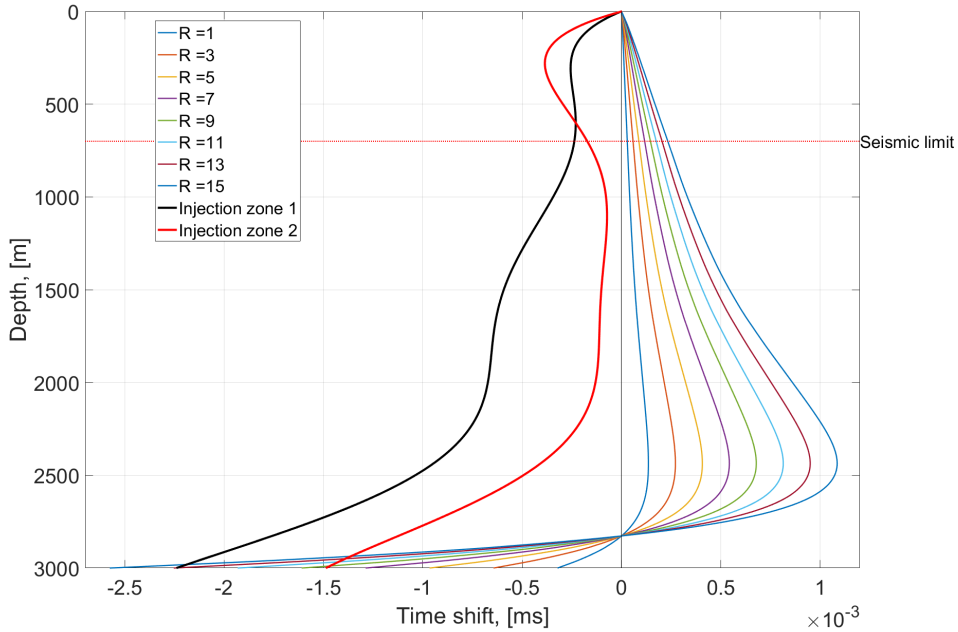

Figure 5.22: Cumulative synthetic time shift, from strain in Figure 5.17b. Black and red lines are the observed time shift in the injection zones.

5.6 Constant R Factor

Equation 3.12 calculates the R factor for one layer given the time shift, interval velocity and thickness change. Overburden is treated as one layer, where the thickness change is estimated from the sea floor subsidence and reservoir compaction, equation 3.16. The subsidence of the sea floor for each focus area is given in Table 5.2. In the injection zones, the reservoir compaction is 0 from ConocoPhillips' reservoir model (Figure 4.5) and -0.04 m from modelling Geertsma's nucleus of strain model, hence, very similar. In the depletion zone, the compaction is most likely around 1 m, based on Geertsma modelling and the compaction map in Figure 4.5. Then the thickness change in each focus area from equation 3.16 is;

$$\sum \Delta z_{DepZone} = -(-1m - (-0.33m)) = 0.67m \tag{5.1}$$

$$\sum \Delta z_{InjZone1} = -(0 - (-0.24m)) = -0.24m \tag{5.2}$$

$$\sum \Delta z_{InjZone2} = -(0 - (-0.29m)) = -0.29m \tag{5.3}$$

This means that the overburden above the depletion zone has expanded and the overburden above the injection zone has compacted, which correlates to the negative time strains here. The interval velocity is averaged from sonic logs to be approximately $2000m/s$. From equation 3.12 the estimated R factors for the focus areas and thickness change estimations are given in Table 5.5. From the table it becomes clear that R is much smaller in the depletion zone than in the injection zones. This is because the time shift values are similar in all areas, but the thickness change is much larger in the depletion zone, despite that a compaction of 1 m is quite modest from the modelled reservoir compaction presented in Figure 4.5.

The estimation of R is very sensitive to Δz. If the modelled compaction at top reservoir in the injection zones is incorrect and compaction is not 0 but has increased, then Δz becomes smaller and R will be larger. However, compaction cannot be larger than the subsidence of the sea floor (Table 5.2) because the time shift indicate speed-up, which means that the overburden cannot have stretched. If the top reservoir has been lifted because of repressurization in injection zone 1 and 2, Δz will be larger as the overburden has compacted even more, and R will

correspondingly be smaller. This is plotted in Figure 5.24.

Table 5.5: R factors from equation 3.12 by treating overburden as one layer; with one thickness change and one time shift.

Focus area	**Time shift at top reservoir, [ms]**	**Thickness change, [m]**	R
Injection zone 1	-2.26	-0.24	8.4
Injection zone 2	-1.48	-0.29	4.1
Depletion zone	2.07	0.67	2.1

The constant R factor can also be estimated from considering the time shift curve in depth and the total stretch of the overburden, which is given in equations 5.1, 5.2 and 5.3 for the three focus areas. The flow chart is presented in Figure 4.10. The basic idea is to test different R factors to see which give a total stretch equal to the observed stretch, based on equation 3.13. The thickness change is then summed for all intervals, but the thickness change shallower than 700 m is excluded from the summation because the shallow seismic time shifts are not trusted. From theory and from simulations using Geertsma's nucleus of strain model, the thickness change should be very small this shallow. Henceforth, removing it seems acceptable. Plots of the thickness change in depth from the time shift curve and R factors between 1 and 10 are given in Section A.6 in the Appendix. The R values that fit best are given in Table 5.6 with the corresponding thickness change. In the depletion zone, the best fit was $R = 3$, for injection zone 1 the best fit was $R = 8$ and it was $R = 4$ in injection zone 2. These R factors correlate very well to the values estimated in Table 5.5, indicating a substantial difference in R for depleting and repressurization zones.

Table 5.6: R factors from equation 3.13, compared to the total thickness change of the overburden presented in equations 5.2, 5.2 and 5.1.

Focus area	**Best fit R factor**	**Thickness change from R, [m]**
Injection zone 1	8	-0.239
Injection zone 2	4	-0.284
Depletion zone	3	0.665

Equation 4.4 gives the compaction at top reservoir as a function of different R factors and the time shift curve in depth. Hence, one function for each focus area. Figure 5.23 demonstrates

the correlation between R and reservoir compaction in the depletion zone from equations 4.4 and 3.12. From the plot it is clear that the equations provide very similar R trends, despite that equation 3.12 only considers the time shift at top reservoir and not the time shift curve. It is also clear that R decreases when compaction is larger. Moreover, based on these time shift values it is not possible to match compaction larger than around -2.5 m for equation 3.12 and -3 m for equation 4.4.

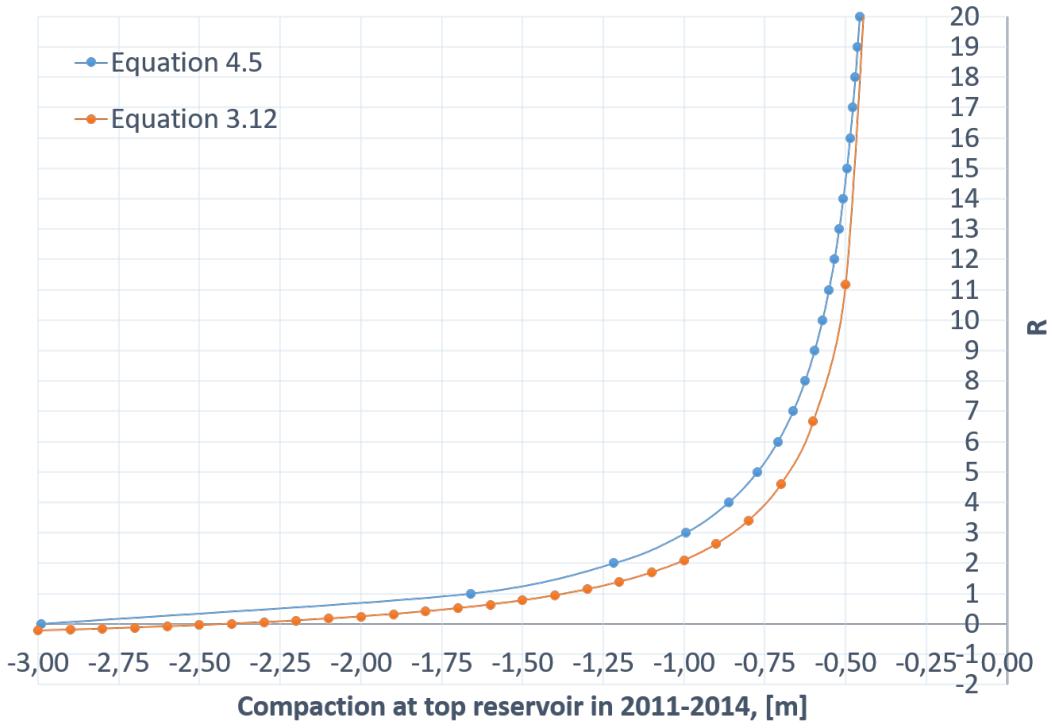

Figure 5.23: R factor in the depletion zone as a function of reservoir compaction in 2011-2014, from equations 3.12 and 4.4. Negative values means compaction has increased.

Figure 5.24 displays the R factor in injection zone 1 and 2 as a function of reservoir compaction from equations 4.4 and 3.12. The equations give similar trends for the correlation between R and reservoir compaction in these regions as well. Here, positive compaction means that the top reservoir has been lifted. In the injection zones it is also evident that R is increasing for smaller thickness changes, but smaller thickness change here is related to continued reservoir compaction (negative values). R will be smaller if the reservoir has been uplifted because of injection, because Δz becomes larger. It is obvious from Figure 5.24 that R is larger in injection zone 1 than injection zone 2 for the same reservoir compaction.

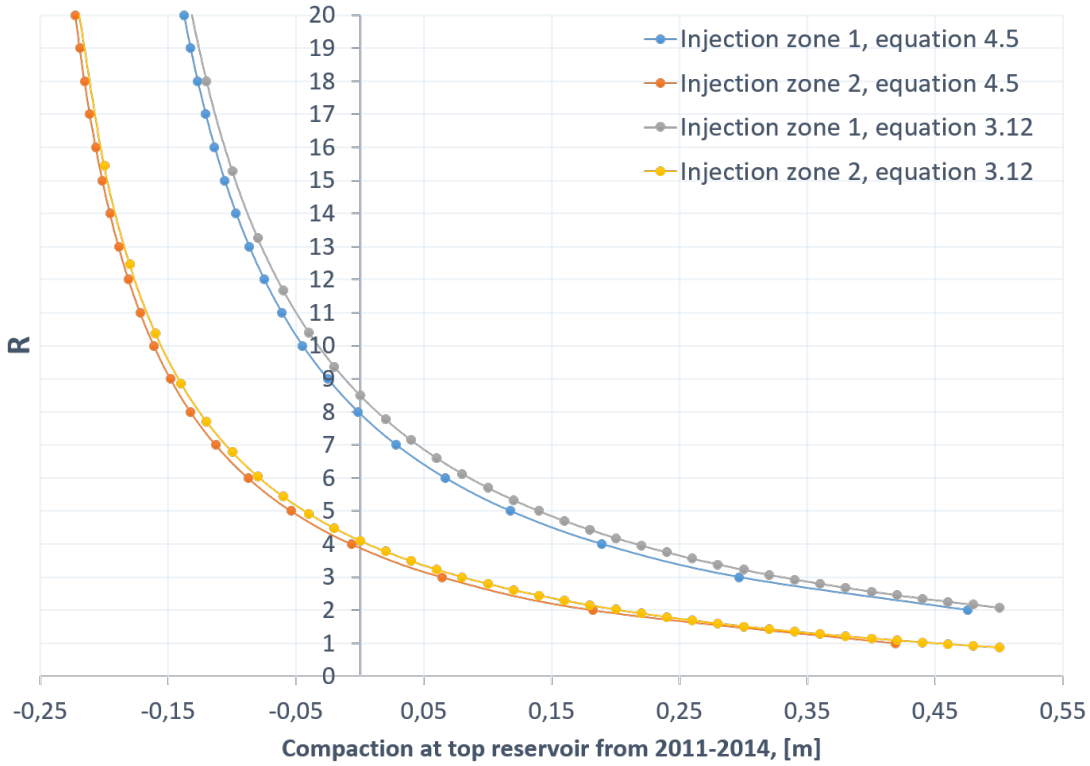

Figure 5.24: R factor in the injection zones as a function of reservoir compaction in 2011-2014, from equations 3.12 and 4.4. Negative values means compaction has increased, positive compaction means that the reservoir has been uplifted.

Chapter 6

Discussion

6.1 Overburden Time Shifts

The time shift curve in the overburden for the three focus areas; depletion zone, injection zone 1 and injection zone 2 are displayed in Figure 5.3. The magnitude of the time shifts at top reservoir was similar in all focus areas. The time shift curves are believed to be somewhat robust, since they are averaged between 6-7 traces within the area and should therefore represent each region. Therefore the consistent leap in time shift right below sea floor might indicate an actual speed-up in the shallow overburden. The time shifts are affected by the horizontal P-wave velocity because of the shallow depth and corresponding large offsets. A speed-up in the horizontal velocity might be induced by a large-scale arch covering the Ekofisk Field and reaching up to the shallow overburden, but this is simply a theory based on the consistency of the time shift leaps in the shallow overburden. A more likely explanation is that the negative time shift leap is caused by poor imaging in the shallow section, which could provide further artifacts. It certainly does not seem realistic that it is a speed-up in the vertical P-wave velocity, as there are no indication of the overburden being compacted directly below sea floor.

Time strain was estimated from 4D time shifts. The time strain curves, Figure 5.4, reveal that in the depletion zone there is a slight slow-down continuously in overburden. Figure 6.1 displays the time strain in the injection zones and velocity trend of the overburden. The grey area is where 4D seismic is not trusted. In the injection zones the time strain curves indicates that the overburden is contracting between $700m$ and $1700m$ (speed-up), that there are approximately no changes between $1700m$ and $2000m$, but is again contracting strongly from $2000m$ to top

reservoir. This is most clear in injection zone 1, which is plotted in red in the time strain curve. Velocity and strain follow the same trend in the part marked A, where they increase to a peak and then decrease again. In B, time strain and velocity are both at a minimum. Time strain and velocity both increase in C. Hence, it is possible that the in-situ velocity trend in the overburden might explain the time strain above the injection zone, where strain is small. There is no correlation between time strain curve and velocity curve in the depletion zone. A possible explanation might be that the strain is very small in the overburden of the repressurization zones, therefore the time shift is primarily caused by a change in velocity, while in the depletion zones the time shift is dominated by change in thickness.

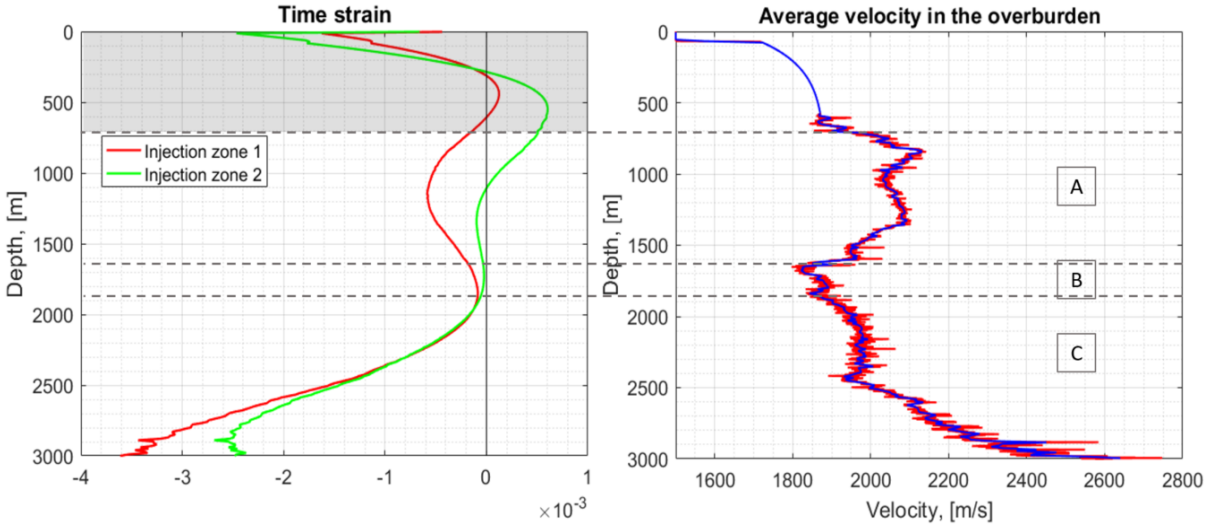

Figure 6.1: Time strain in the injection zones compared to the average velocity in the overburden. Grey zone is where seismic is not trusted due to poor imaging.

Furthermore, the primary lithology of the overburden is shale. Several studies conclude that velocities in shale are quite stress insensitive at larger stress, which was demonstrated in Figure 3.2b, (Lo et al., 1986; Bathija et al., 2009). This means that $\frac{\Delta v_p}{v_p}$ will be small in shale, which further indicates that thickness change does not need to be very large to control the time shift in shale from equation 3.3. However, at shallow burial depths the stress will be low and the velocities more sensitive (see Figure 3.2b), which might have implications on the R factor this shallow.

The additional two-way traveltime caused by stretching or contraction of the overburden can be estimated if the thickness change of the overburden is known and an average velocity of the overburden is used. This is presented in section A.8 in the Appendix. From the estimation it

was clear that the thickness change accounts around 32% of the time shift in the depletion zone, and around 11% in injection zone 1. Hence, the strain appears to have a greater influence on the time shift in the depletion zone, although this is a very rough estimate.

6.2 R Factor

6.2.1 Depth-Dependent R Factor

The depth-dependent R factor was estimated based on strain modelling from Geertsma's nucleus of strain model. It has been presented for one model of the Ekofisk Field referred to as model 1, where it varied from $R = 14$ to $R = 2$. Model 2 is an alternative method of modelling the Ekofisk Field using superposition of Geertsma's nucleus of strain model, the details and the calculations are presented in section A.4 in the Appendix. Figure 6.2 compares the depth-dependent R for both models. The grey zone shallower than $700m$ is where 4D seismic is not trusted. It is clear that the depth-dependent R factor from model 2 demonstrate the same trend as model 1; that R is decreasing in depth, although there is a larger variation i R values in model 2 (from 2 to 21) than in model 1 (from 2 to 14). The interval A is marked in Figure 6.2 from $700m$ to $1700m$, for both models this is the interval with the highest variation in R and the largest absolute value of R. This interval shows a clear decrease in R as a function of increased depth. The interval from $1700m$ to $2300m$ is referred to as interval B, here R is certainly more stable than in A. R is constant at $R = 2$ for model 1, and decrease from $R = 4$ to $R = 3$ for model 2. In C, R is predominantly 3 for both models, except some smaller segments close to the reservoir where it decreases to $R = 2$. For model 1, the average R deeper than 700 m is $R_{Average} = 5$, while for model 2 it is $R_{Average} = 7.3$. Model 2 predicts 0.2 m larger overburden thickness change than model 1. Despite this, the strain distribution is very similar in model 1 and model 2, which means that the strain distribution above a depleting reservoir does not vary drastically with superposition. Thus, the depth-dependent R trend is quite robust in depletion zones at the Ekofisk Field. To clarify, the values in the shallow overburden ($\approx 750m$) show a substantial variation, but the values close to the reservoir and the overall depth-dependent trend is clear.

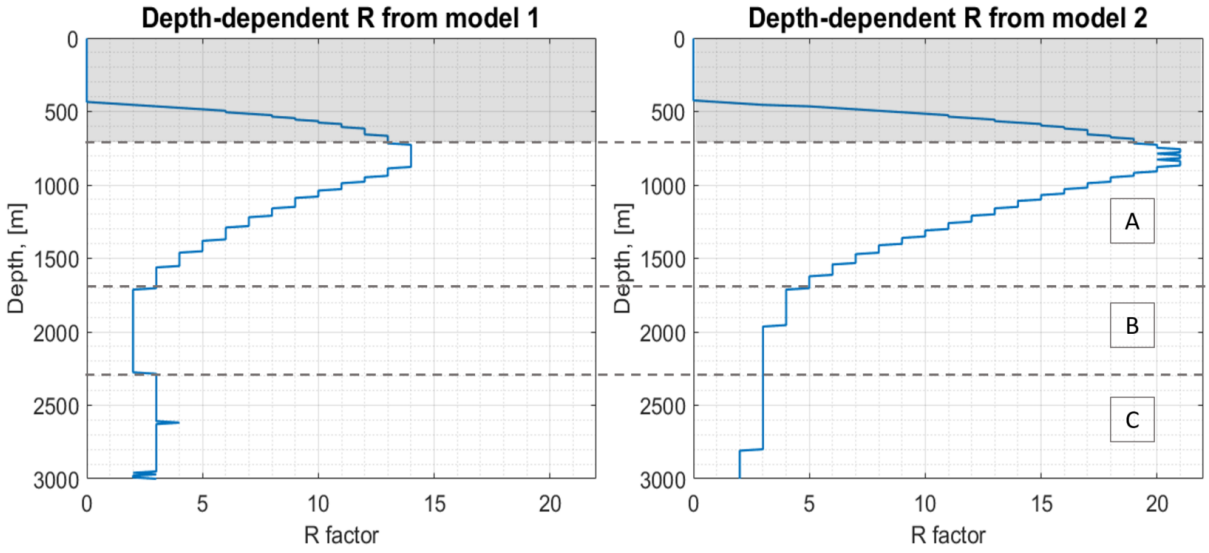

Figure 6.2: Depth-dependent R from model 1 and model 2. Grey zone is where 4D seismic is not trusted because of poor imaging.

(Røste and Ke, 2017) estimated the depth-dependent R for the sandstone fields Snorre, Heidrun and Statfjord, all located at the Norwegian Continental Shelf. It was concluded that R was larger in part of the shallow overburden, which correlates well to these findings on the R factor trend of the Ekofisk Field. R was also found to be layer-dependent. For these fields suitable values were estimated to be $R = 100$ in shallow overburden and $R_{Average} = 15$, which is considerably larger than what has been found here. This might be caused by the clear difference in the magnitude of the strain, and is discussed further in Section 6.2.5. A depth-dependent R factor was also required to match 4D time shifts with compaction data at the HP/HT reservoir Elgin in the North Sea. R was 5 or less for the majority of the overburden, but reached 40 closerin a thick layer of hard Cretaceous Chalk to the reservoir, (Hawkins, 2008). This implies a layer-dependent R factor, as was suggested by (Røste and Ke, 2017). However, it should be mentioned that there is no observed sea floor subsidence at the Elgin Field and that the time shifts are believed to be caused by velocity changes alone. Hence, there is a clear difference in both overburden lithology and strain magnitude compared to the Ekofisk Field, which might explain the variation in estimated R factor.

6.2.2 Lateral Variation in the R Factor

Furthermore, (Røste and Ke, 2017) established that R has a strong variation vertically, yet a small lateral variation based on the data from the Heidrun, Snorre and Statfjord fields. But from analyzing the overburden of depletion and injection zones in this study, it appears that R indeed has a lateral difference at the Ekofisk Field, see Figures 5.23 and 5.24 and Table 5.5. The lateral variation in R is believed to be triggered by repressurization, because this causes localized compaction. Thickness change is clearly different above injection and depletion zones, which is evident from Geertsma's nucleus of strain model for displacement, Figure 5.15. The difference in thickness change above injection and depletion regions is an explanation to why R varies too. An important observation is that the strain above the injection zone is considerably smaller than the strain above the depletion zone from both model 1 and 2 for the majority of the overburden, see Figures 5.16b and A.6b.

In the calculations it is assumed that the compaction at top reservoir is the same in injection zone 1 and injection zone 2, which comes from the reservoir model by ConocoPhillips (Figure 4.5) because Geertsma's nucleus of strain model was not representative of an injection zone. However, the time shift curve in depth and the time shift at top reservoir is very different in injection zone 1 and 2. Therefore, the compaction at top reservoir should probably be different too. The flow chart in Figure 6.3 describes how the lateral variation in R is affected if the modelled reservoir compaction in the injection zones is incorrect. The plot is based on the observed R trend in the injection zones as a function of reservoir compaction, Figure 5.24. If the real reservoir compaction ($C(real)$ in Figure 6.3) is negative, meaning continued compaction, Δz will be smaller and R in the injection zones ($R(inj)$) will be larger. This means that the difference between R in depletion and injection regions will be larger, and the lateral variation in R at the field is greater. If the reservoir compaction is positive, the injection has caused uplift of the top reservoir. This would lead to smaller R in the injection zones and an overall smaller lateral variation between depleted and repressurized regions.

Since reservoir uplift caused by injection is considered rather unlikely, this further confirms a lateral variation in R at the Ekofisk Field. That being said, stretching of the overburden rocks may cause horizontal fractures, which may reduce the strength of the rock (see Section 3.3). From the time shift curve in the overburden (Figure 5.3) it was clear that most of the deformation takes place a few hundred meters above the reservoir. Through decades of depletion of the

Ekofisk Field, it might be possible that these rocks have been stretched to a degree where the strength is reduced enough for reservoir uplift of a couple cm to be possible, but this is just speculation.

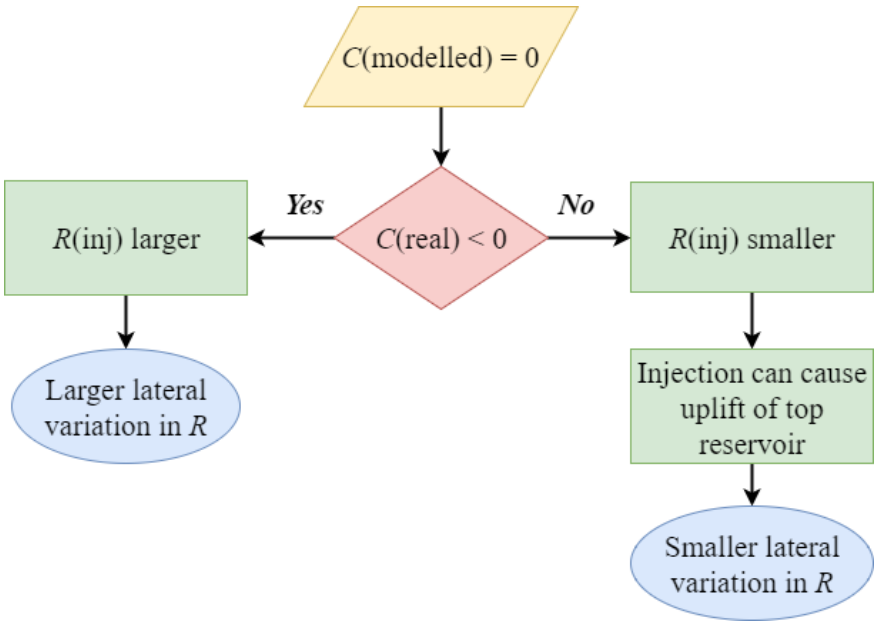

Figure 6.3: Flow chart describing how R in the injection zone ($R(inj)$) will change if the modelled reservoir compaction ($C(modelled)$) in the injection zone is not representative of the real compaction ($C(real)$), and how this will affect the overall lateral variation in R at the Ekofisk Field.

Another factor contributing to the lateral variation in R is the difference in stress path around the field. Strain and stress sensitivity depends strongly on stress path, (Holt et al., 2008, 2009). R was measured for different stress paths; $R = 6 - 7$ during hydrostatic loading, while $R = 1.5 - 1.8$ when applying a constant mean stress path, where the latter is believed to be representative for the overburden above a depleting reservoir, (Holt et al., 2009). From a measurement presented in (Holt et al., 2008) performed on a field shale core; $R \approx 13$ in the overburden above the center of a depleting reservoir, and $R = 6$ in the overburden near the edge of the reservoir was estimated. This shows how fluctuating and complex R is.

But more importantly, for all types of cores, both synthetic and real, and for all stress paths, the R factor decreased with increasing axial strain, (Holt et al., 2008). Moreover, the R factor proved to be especially sensitive at small stress and strain changes. This correlates well with the observations for R factors above depletion and injection zones; namely that R is larger in regions being repressurized, where strain is considerably smaller than above the depletion zones. What is more, this also agrees with the observations of the depth-dependent R in Figure

6.2, where the R factor is much larger further from the reservoir where stress and strain is smaller. This is all reasonable from the definition of R; $R = -\frac{\Delta v}{v \cdot \varepsilon_z}$, that R is small when strain is large. Hence; R is smaller in the depletion zones since strain is very large here, and smaller close to the reservoir where strain is at its largest.

6.2.3 Estimating Velocity and Thickness Changes from Time Shifts and Constant and Depth-Dependent R Factor

Based on this study it seems clear that R varies in depth as the strain and time shift do not appear to vary equally throughout overburden. The best fit for a depth-dependent R curve based on 4D data and geomechanical modelling in the depletion zone was presented in Figure 5.20. R had a range from 2 to 14, and the average R deeper than 700 m was $R_{Average} = 5$. However, from estimations of a constant R in Section 5.6, R was estimated to be in the interval of $R_{Constant} = 2-3$. The velocity change in each interval has been estimated to interpret which constant R appears optimal (2, 3 or 5) and to understand the effects of choosing a constant R versus a depth-dependent R in the estimation of velocity from 4D. The latter analysis was only possible to perform in the depletion zone since the depth-dependent R was only established in this region and not in the injection zones, because the simulations using Geertsma's nucleus of strain model did not appear reasonable here. The velocity change is estimated from the observed time shift and R, using equation 3.14. Figure 6.4 displays the velocity change for the tree different values of a constant R (2, 3 and 5) and for the depth-dependent R for the overburden between $2000m-3000m$. The velocities are only displayed for these depths because the estimated velocity changes are very much alike for all R trends, which is clear from the estimated velocities in around $2000m$ Figure 6.4. The calculations are especially similar for $R = 3$ and the depth-dependent R, which give the exact same calculation for most of the depths. The difference in velocity change is largest in the intervals closest to the reservoir. Nevertheless, the differences in the approximated Δv_p are so small that it seems fair to neglect them. Thus, estimation of velocity change from time shifts is not very sensitive to the choice of R.

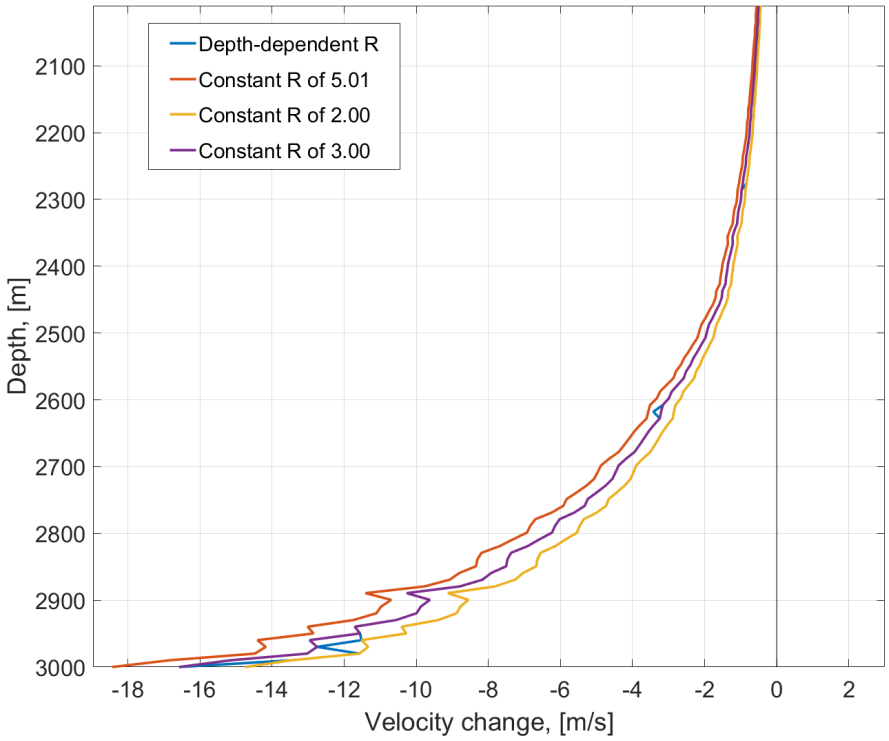

Figure 6.4: Velocity change in depth above the depletion zone estimated by depth-dependent R and constant R, displayed in the depth $2000m - 3000m$. Calculated from 4D data by equation 3.14.

In Figure 6.5; thickness change was estimated in the overburden from the observed time shift and R in the depletion zone from equation 3.13, both depth-dependent and constant R. The thickness change estimated from Geertsma's nucleus of strain model (Figure 5.16b) is included and marked in green. It is clear from the plot that the difference in strain estimation from constant and depth-dependent R is larger than for the estimations of velocity, Figure 6.4. In Figure 6.5 the thickness change from the depth-dependent R and the modelled strain are practically overlapping deeper than 500 m. Deeper than 1500 m $R = 3$ is a good fit to these curves as well. This means that the depth-dependent R is the optimal fit to the data, but choosing a constant R can also match the observed thickness change. From both Figure 6.5 and Table 6.1; it is essential to choose the correct value when applying a constant R. Based on estimation of changes in velocity and thickness change, the constant R that appears best is $R_{Constant} = 3$. By summing the thickness change deeper than 700 m; the estimations are noticeably different for each R, which is clear from Table 6.1. This indicates that R has larger effect on the estimation of changes in thickness than estimation of velocity changes from 4D seismic data.

Table 6.1: Estimation of total thickness change of the overburden of the depletion zones from equation 3.13, given the time shift curve,velocity in depth and testing different R factors.

R	**Total overburden thickness change, [m]**
Depth-dependent R	0.654
Constant R of 5	0.443
Constant R of 3	0.665
Constant R of 2	0.887

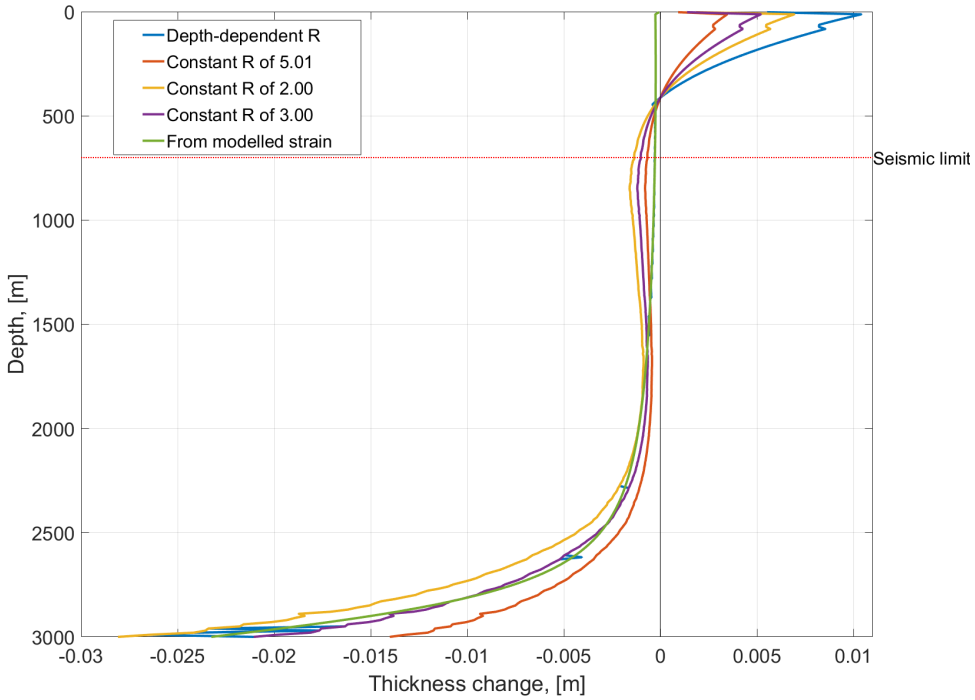

Figure 6.5: Thickness change in each interval in the overburden of the depletion zone from assuming depth-dependent R and constant R in equation 3.13. The thickness change from Geertsma's nucleus of strain model above a depleting reservoir (reservoir 2 in model 1) is included.

Assuming a constant R when approximating velocity changes from 4D time shifts seems acceptable from Figure 6.4, where the estimation of velocity change for different R factors are overlapping most of the overburden. But the estimation of thickness changes is more sensitive to the choice of R (Figure 6.5) and it is therefore important to apply an appropriate constant R when thickness change is estimated directly from 4D time shifts. The constant R cannot match the time shift in all of overburden since R appears to be depth-dependent. But it is important that the choice of $R_{Constant}$ matches R in the deeper part of overburden, because this is where

time shift is largest and will have the most influence on estimation of thickness change. This is clear from Table 6.1; thickness change from the depth-dependent R and $R_{Constant} = 3$ are very alike. Using the average of the depth-dependent R, $R_{Average} = 5$, did not give very good estimates of the thickness change.

As presented in Table 5.6, the optimal R factors were $R = 8$ in injection zone 1, and $R = 4$ in injection zone 2. The estimations of velocity change and thickness change for the focus areas based on these R values are given in Figures 6.6 and 6.7. It is clear than the changes in both thickness and velocity are largest in the depletion zone. In the injection zones; thickness change is largest in injection zone 2, but velocity changes are largest in injection zone 1. Also, from the estimation of velocity change, Figure 6.6, it is clear that the data does not suggest any slow-down in injection zone 1 in the intervals where time shift data is trusted. Around 700-800 m depth the calculation predicts the same velocity change in injection zone 2 and the depletion zone. This might indicate that the repressurization in injection zone 2 is not large enough to induce speed-up in the shallow overburden. The same observation is clear from the thickness change in Figure 6.7; that thickness change shallow is similar for injection zone 2 and the depletion zone. In general, these constant R values appear to predict reasonable changes in thickness and velocity.

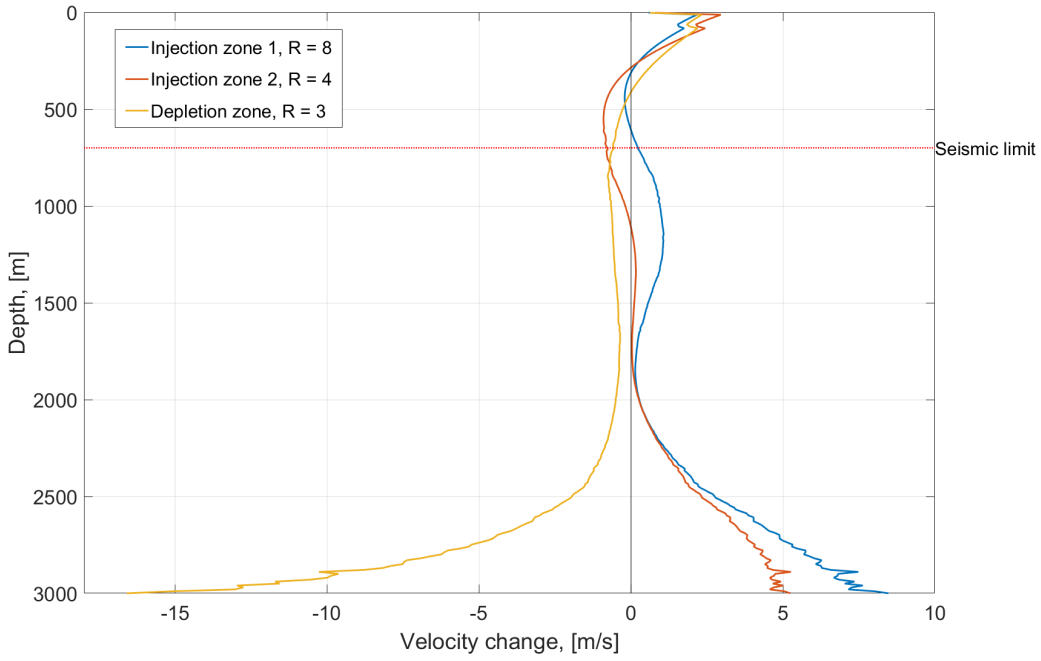

Figure 6.6: Velocity change in depth for each focus area from equation 3.14 by assuming constant R.

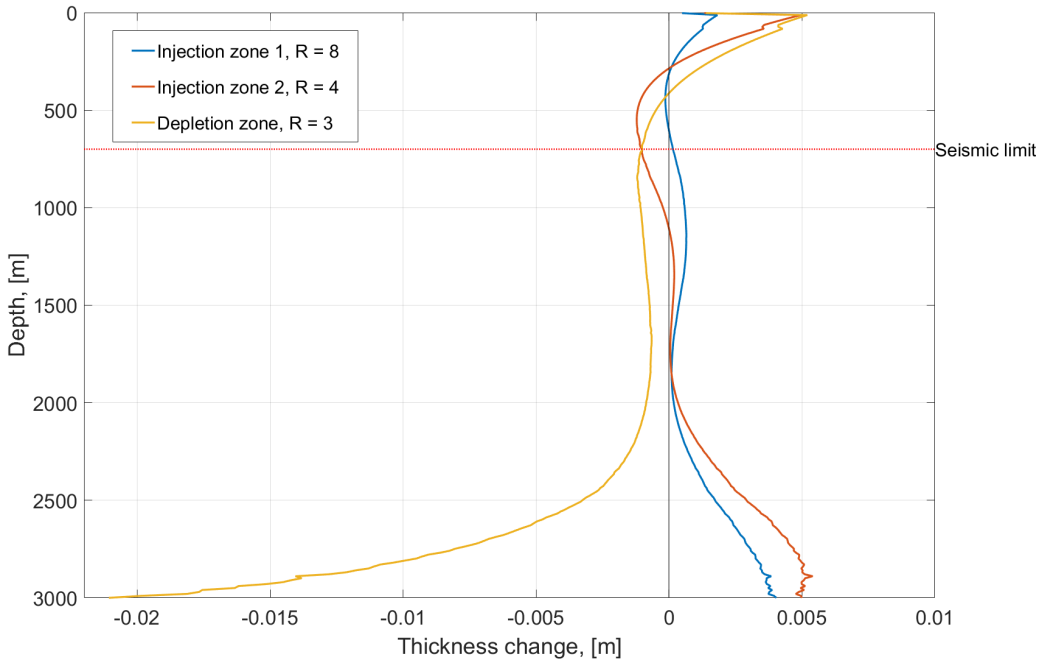

Figure 6.7: Thickness change in depth for each focus area from equation 3.13 by assuming constant R.

It is a curious observation that an average of the three optimal R factors in the focus areas (3, 4 and 8) give an average of $R_{average} = 5$. An R of 5 is well established from (Hatchell and Bourne, 2005), and it appears to be a the average R on a field scale of the overburden of the Ekofisk Field. Although it should be used with care, if it should be applied at all.

6.2.4 R Factor from Analysis of Overburden Core from the Ekofisk Field

Two cores from the overburden of the Ekofisk Field have been acquired by ConocoPhillips and analysed by SINTEF Petroleum AS, Formation Physics Laboratory. The first was cored in September 2007 at 1649.9 m TVDBSF and is referred to as shale 1. The second was cored in October 2011 at 1738 m TVDBSF and is referred to as shale 2. Both cores had high porosity, low quartz content and were dominated by smectite. The sensitivity of P-wave velocities at different inclinations have been measured at ultrasonic frequencies. By a triaxial-loading step the sample is brought to in situ stress. In situ stress path simulations (ISSP) mimic different stress paths. The ISSP sequence is divided into three undrained segments; ISSP 1, ISSP 2 AND 122P 3, which are performed both fast and slow for shale 2. Details from the analysis is presented in section A.7.

The resulting R is demonstrated for both cores in Table 6.2. It is clear that R is very small

for all stress paths; maximum being 2. ISSP 1 represents the overburden above a depleting reservoir. An R of 2 was also a good fit in the depletion zone close to the reservoir, from Figure 6.2, and the constant R was also estimated to $R = 2 - 3$, see Tables 5.5 and 5.6. ISSP 3 is the stress path that reflects increasing axial load above in situ level, simulating a stress path at the edge of a depleting reservoir. Here, R factors are 0 or close to 0 for both Shale 1 and Shale 2, which means that $v_{p,z}$ seems to be rather stress insensitive in this scenario. The R factors from these experiments are not very similar to the relatively large constant R factors measured in the injection zones, see Tables 5.5 and 5.6. This might indicate that R is not uniform and will vary depending on many unpredictable factors. It might not be possible to represent an entire field from a small core sample, but a valulable insight to the understanding of the R factor might come from lab experiments using different stress paths, (Holt et al., 2016).

Table 6.2: R factors measured on overburden cores from the Ekofisk Field by SINTEF Petroleum AS, Formation Physics Laboratory.

Core	**R factor during unloading (ISSP 1)**	**R factor during loading (ISSP 2)**	**R factor during loading (ISSP 3)**
Shale 1	2	2	0
Shale 2 (Fast cycle)	1.55 to 1.70	1.37 to 1.49	X
Shale 2 (Slow cycle)	1.14	1.17	-0.04

6.2.5 Nature of the R Factor

It is generally established that the absolute value of R will increase in sandstone and decrease in shale with decreasing effective stress, which is the stress situation expected in the overburden above depleting zones, (Carcione et al., 2007; Bathija et al., 2009). This was discussed from the sensitivity of velocity and strain in shale and sandstone, figures 3.2 and 3.3. Figure 6.8 demonstrates the correlation between lithology and depth-dependent R in the overburden. The lithology is estimated from the average volume of shale from the gamma ray log, equation A.5 in Section A.2 in the Appendix. In Figure 6.8 the overburden is divided into three intervals; A, B and C. B covers the lowest R values of the overburden and corresponds well to the highest shale content. The overall correlation between R factor and lithology is not very clear; by simple evaluation of the lithology the R factor should increase more around in the interval C as the volume of shale is decreasing. Hence, there are other factors that are more dominating

for the R factor than lithology. But there is a certain correlation to the depth-dependent R and effective stress, velocity and lithology, since they all depend on each other.

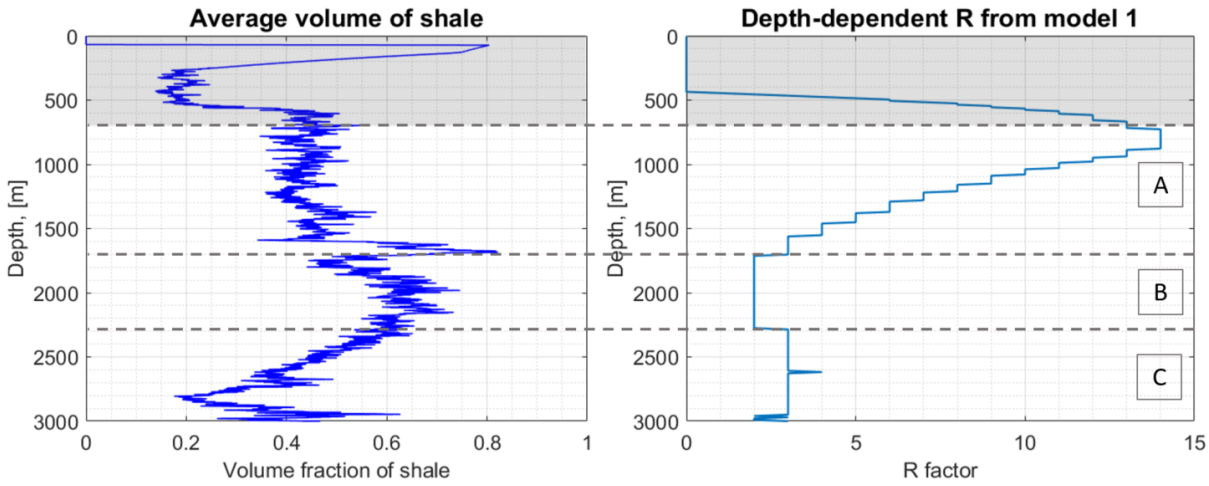

Figure 6.8: Average volume of shale in the overburden correlated with the depth-dependent R factor.

As presented in Table 1.1 in Chapter 1, there has been published numerous different values of R. However, the estimation of R might vary depending on method of measurement; since lab measurement apply waves at ultrasonic frequency this, while 4D seismic use larger wave lengths. Using 4D seismic data; (Hatchell and Bourne, 2005), (Røste et al., 2005), (Janssen et al., 2006), (Røste et al., 2015) and (Røste and Ke, 2017) conclude with a variety of overburden R values from 2.6 to 20, thus, the variation in R cannot simply be explained by a difference in measuring approach.

(Hatchell and Bourne, 2005) found $R = 5$ based on different fields worldwide; chalk reservoirs, HPHT sandstone reservoir and deepwater turbidite field. (Røste et al., 2015) and (Røste and Ke, 2017) have larger values of $R = 15 - 20$. A possible explanation is that the studied data are from the overburden of sandstone reservoirs. These fields experience little compaction in contrast to the chalk reservoirs Valhall and Ekofisk that are discussed in (Røste et al., 2005), (Janssen et al., 2006) and this study. This might also explain why (Røste and Ke, 2017) found R not to vary laterally; because compaction does not vary much laterally, while data and methods from this study implies that R indeed varies laterally at the Ekofisk Field as reservoir compaction cause varying overburden thickness change. This emphasizes that the R factor is unique for each field.

In summary; lab experiments has confirmed that R is highly stress dependent, henceforth, a constant and well-defined R is not realistic, (Bathija et al., 2009). Additionally, the R factor

varies with stress path, (Holt et al., 2008, 2016). Not to mention that experiments have found R to differ for stress loading and stress unloading. This further supports a lateral and vertical variation in R. Working with real data further complicates the situation, because the zones now being repressurized were previously depleted, therefore the rocks in the overburden have first been stretched and are now being compacted. The depth-dependent R factor has not been presented in the overburden of injection zone 1 and 2, because the modelling from Geertsma's of strain model was not good enough during repressurization. But from the discussion and from the depth-dependency of R in the depletion zone (Figure 6.2) it appears reasonable that R should vary above repressurization zones as well as depletion zones, as factors as strain and stress path changes. However, this needs to be investigated further. From the discussion above, R correlates somewhat with lithology, effective stress, and velocity in the overburden. Yet, it appears that strain is the controlling factor of the R factor trend in the overburden and time shifts are only dominated by velocity when strain is very small, which is seen in the overburden of the repressurized regions in Figure 6.1. Stress and strain in the overburden are mainly induced by compaction of the reservoir, which leads to stretching of the overburden rocks. However, the overburden rocks may be compacted during repressurization. The magnitude of reservoir compaction depends on production activity, but a chalk field and sandstone field experience compaction in completely different magnitudes during the same pore pressure depletion. Roughly, the nature of R (magnitude and variation) is therefore controlled by reservoir properties. This implies that R will have a stronger variation laterally at fields where compaction is large and heterogeneous. Moreover, R will be much smaller in fields where compaction is large. Additionally, R will change through time and vary both laterally and vertically as strain and stress path changes. Hence, the overburden R factor is principally a function of;

$$R_{Overburden}(x, y, t, ReservoirProperties) \tag{6.1}$$

6.3 Assumptions and Critique

From the estimations of synthetic time shifts (Figures 5.18 and 5.21), velocity change (Figure 6.4) and thickness change (Figure 6.5) it is clear that the calculations are noticeably sensitive to the overburden velocity. It has been assumed that the velocity averaged between six sonic logs could be representative of the in situ velocity. The thickness of each interval was set to $z = 10$, which might be too large to estimate of the constant velocity for the layer, and to apply equation 3.3. The time shift has been estimated at clear horizons to minimize the error of the time shift values. The time shift is more accurately measured at distinct horizons when comparing seismic surveys. But the time shift value at each horizon for all wells was manually interpreted and then averaged, which might lead to errors. Moreover, the depth of each horizon was averaged between all six pseudo wells for every surface. Further, it was assumed that the time shift curve in depth could be represented by an interpolation based on the picked time shifts. The time shifts shallower than 700 m were excluded in the estimations of thickness change of the overburden because of poor imaging. From simulations using Geertsma's nucleus of strain model the strain appeared to be minimal in the shallow overburden, therefore the assumption of excluding the shallowest 700 m from the thickness estimation seems reasonable. It is assumed that the total thickness change is known from sea floor subsidence and reservoir compaction. This is further used to estimate the constant R from equation 3.13. However, the reservoir compaction is modelled and not measured, leading to uncertainties. Based on the time shift curve and magnitude of time shift at top reservoir in injection zone 1 and 2, it does not seem reasonable that compaction is the same. Nevertheless, from Figure 6.3 it is clear that the lateral variation in R is observed as long as the reservoir is not uplifted due to injection. Reservoir uplift because of injection would be a sensational observation in itself, as it is quite established as being an improbability.

Vertical ray propagation has been assumed for all calculations involving interval traveltime. This implies that t can be replaced by equation 3.2, where z is the interval in depth. Noise-free zero-offset traveltimes would be optimal, but is unfortunately not realistic. Anisotropic effects on the time shifts have also been disregarded.

It has been assumed that there has been no change in pore pressure in the overburden, which is probably untrue, (Bauer et al., 2008). Additionally, that the overburden rocks above the repressurization zones have stretched and are then compacted have not been taken into

account. Everything is assumed elastic and no plastic deformation is considered, although the modelled strain above the depletion region (Figure 5.17b) indicates strain might be large enough for plastic deformation to occur.

The interval from 1400 m to 2400 m is believed to represent an overpressured zone, where pore pressure is high and effective stress is low, see the definition of effective stress, equation A.3 presented in section A.1 in the Appendix. The effective stress curve in the overburden is demonstrated in Figure A.1 in section A.3 in the Appendix. Velocity in this interval is also low, as seen in Figure 6.1. The overpressured zone will affect the time shift, but have not been included in the gemomechanical model used to estimate strain and R. The same interval of no (or small) velocity changes is estimated from time strains from the Snorre Field for lower Nordland and Upper Hordaland, (Røste et al., 2015).

The subsidence in each focus area established from bathymetry data is assumed to be representative of the studied region, this is despite poor bathymetry from 2014.

6.3.1 Application of Geertsma's Nucleus of Strain Model

Geertsma's nucleus of strain model was applied to model the displacement field surrounding a reservoir. This is a very simplified 1D model, and a more complex model would likely give more realistic results. Further, the Ekofisk Field was modelled by utilizing the superposition principle with several reservoirs, assuming that superposition is acceptable. Two alternative models using superposition were presented, referred to as model 1 and model 2. The actual pore pressure change of the Ekofisk Field is not known, and the upper and lower limits were estimated from ConocoPhillips' reservoir model, assuming that this is a somewhat correct approximation of the pore pressure of the Ekofisk Field. From simulations of the analytic Geertsma solution in one reservoir (Section 5.4); it is critical to apply an appropriate reservoir radius to estimate strain distribution in the overburden. The radius of each reservoir in model 1 was established from the area extent of the time shifts at top reservoir.

In general, subsidence of the sea floor and reservoir compaction was decently modelled by Geertsma's nucleus of strain model. Moreover, the strain above the depleting region indeed appeared reasonable. However, it was not possible to use the strain above the repressurization zones from Geertsma's nucleus of strain model to create synthetic time shifts matching the observed time shifts in injection 1 and 2. A possible reason for the poor fit between the modelled

strain and the observed time shift might be because of the assumption of perfect elasticity in the model, hence, gravity is not taken into account when a reservoir is being repressurized. Additionally, Geertsma's nucleus of strain model assumes constant mean stress or constant volume. This is believed to be a good approximation of the overburden above a depleting reservoir, but perhaps not ideal to simulate the overburden above repressurization zones. Although this is further complicated by superposition, it might contribute to the poor modelling of strain above the injection zones. Furthermore, the assumption of no contrast in elastic properties between the reservoir and the surroundings simplifies the results and make them perhaps unfit to model strain used in estimation of R. (Røste and Ke, 2017) estimated the depth-dependent R factor from the sandstone fields Heidrun, Snorre and Statfjord and found it to be layer dependent. If this is indeed the case then the assumption of no elastic contrasts within the overburden makes Geertsma's nucleus of strain model unfit to measure strain and corresponding R in the overburden because it is not possible to distinguish the layer dependence. From the discussion above it was also clear that there is an overpressured zone in the overburden (Figure A.1) that is not taken into account in the geomechanical modelling using Geertsma's nucleus of strain model.

The reservoir is assumed disk-shaped and horizontal during the simulations. As presented earlier; the Ekofisk Field is in reality an elongated anticline. The assumption of a disk-shaped reservoir makes the approach unfit for precise calculations, (Fjær et al., 2008). Further, the elastic moduli in the calculation, E, C_m and ν are based on a database for chalk created and presented by (Havmøller and Foged, 1996), and α on a study by (Engstrøm, 1992). Both studies contained Ekofisk core samples, but elastic properties may vary greatly within the reservoir. Further, difference in measurement may lead to diversity in the estimates of elastic moduli. The elastic moduli proposed in (Havmøller and Foged, 1996) are a bit low compared to other studies, yet, they are applied since 197 data sets were from the Ekofisk Field.

Geertmsa's nucleus of strain model is not assumed to model the Ekofisk Field pefectly. However, the superposition principle describes many of the effects that are experienced in the overburden and most of the observed data. For instance how the effects from different sources at reservoir level are evened out in the overburden by the averaging effect, (Andersen, 1995).

Chapter 7

Conclusion

4D seismic data at the Ekofisk Field from 2011 to 2014 has been analyzed to understand the spatial variation in the overburden R factor. The depth-dependent R factor has been estimated in the overburden of a depleting region using 1D geomechanical modelling and 4D seismic data. An overview of the lateral variation of the constant R factor has been obtained with respect to depleting and repressurized regions, where a constant R factor refers to a fixed R in the vertical direction. The conclusions are as follow;

- Time shifts in the overburden have a strong lateral variation, and the uniform increase in time shifts towards top reservoir is only observed above the depleting zone. This implies that the geomechanical effects in the overburden of injection zones are complex, and Geertsma's nucleus of strain model may not be applied in repressurization regions.
- R is strongly depth-dependent with decreasing values with depth from $R = 14$ to $R = 2$ in the depleting region. This trend appears robust from considering alternative strain models.
- R has a clear lateral variation. This is likely caused by localized reservoir compaction at the Ekofisk field, which is triggered by regional depletion and repressurization. This leads to varying thickness change of the overburden across the field.
  - R is larger above injection regions than depleting regions, this follows from the overburden thickness change being much smaller above the repressurized zones. Suitable values for constant R in the focus areas are;
    - Depletion zone; $R_{constant} \approx 2 - 3$.

    - Injection zone 1; $R_{constant} \approx 8$.
    - Injection zone 2; $R_{constant} \approx 4$.
  - In injection zones, R appears to have a large variation in absolute value, and the magnitude increases with larger repressurization.
  - Both time shifts and the R factor are dominated by velocity changes when strain is small (e. g. overburden of injection zones).

- It is crucial to apply a suitable R factor when estimating thickness change from 4D time shifts. But the estimation of velocity changes from time shifts is not very sensitive to the choice of R.

- R is unique for each field. The general magnitude of overburden R factor is controlled by the thickness change of the overburden, which depends on reservoir compaction and sea floor subsidence. In turn, this is roughly controlled by production activity and reservoir properties.

Chapter 8

Further Work

The 4D seismic in the first $600 - 700m$ of the overburden is not trusted due to poor imaging. This leads to many unanswered questions regarding the nature of R in the shallow overburden. The estimated time shifts are negative and very large, which is clear from the cross-section of the 4D seismic along inline 560 in Figure 5.2. To study shallow time shifts in the future, one possibility is to work with prestack seismic data, which might reveal the effects potentially causing speed-up or slow-down this shallow. It is interesting whether the observed negative time shifts shallow are caused by a real effect or if it simply caused by processing and acquisition artifacts, because of poor imaging. However, because of the consistency of the negative time shift leap it might indicate actual events. This is recommended to study further.

From this study, a general trend of constant R as a function of reservoir compaction was established in the depletion zone and for the injection zones, Figures 5.23 and 5.24, respectively. These plots are based on the time shift curve in each region, which was averaged between 6-7 traces. If more regions of the Ekofisk Field are studied, it would be possible to make a general plot of R for injection and depletion zones at the Ekofisk Field. In combination with the modelled reservoir compaction, a map similar to 4.5, a map of R would be established for the Ekofisk Field field. Though it should be noted that this would be a constant R, and not depth-dependent.

Further recommendations include to study whether it is possible to establish a correlation between the R factor and production data. It should be examined if it would be possible to establish a relationship between a parameter in the reservoir, like pore pressure, and the R factor at different depths and positions in the overburden. This would simplify the operation of

understanding time shifts in overburden and get an increased understanding of how overburden is affected by reservoir changes.

Additionally, the R factor should be determined in depth in other regions of the reservoir. This would provide an R that is more representative of the field as a whole and give an increased understanding of how sensitive R is laterally. In the depletion zones, the same workflow as presented in this report could be applied. However, an effort to model the overburden above the injection zones is necessary to establish the depth-dependent R in these regions. It should be an objective to understand the depth-dependent R trend above the injection zones.

Last but not least; to understand the R factor better one should estimate it from different 4D data surveys, both from different times and of various production lengths.

Bibliography

Andersen, M. A., 1995. Petroleum research in North Sea chalk. RF-Rogaland Research.

Arts, R., Eiken, O., Chadwick, A., Zweigel, P., Van der Meer, L., Zinszner, B., 2004. Monitoring of co 2 injected at sleipner using time-lapse seismic data. Energy 29 (9), 1383–1392.

Barkved, O., Heavey, P., Kjelstadli, R., Kleppan, T., Kristiansen, T. G., et al., 2003. Valhall field-still on plateau after 20 years of production. In: Offshore Europe. Society of Petroleum Engineers.

Bathija, A. P., Batzle, M. L., Prasad, M., 2009. An experimental study of the dilation factor. Geophysics 74 (4), E181–E191.

Bauer, A., Lehr, C., Korndorffer, F., van der Linden, A., Dudley, J., Addis, T., Love, K., Myers, M., 2008. Stress and pore-pressure dependence of sound velocities in shales: Poroelastic effects in time-lapse seismic. In: SEG Technical Program Expanded Abstracts 2008. Society of Exploration Geophysicists, pp. 1630–1634.

Berg, P. W., MacGregor, J. L., 1969. Elementary partial differential equations. Holden-Day.

Byerley, G., Pedersen, J., Roervik, K. O., Ranaweera, K., Janssen, A., 2006. Reducing risk and monitoring water injection using time-lapse (4d) seismic at the ekofisk field. In: SEG Technical Program Expanded Abstracts 2006. Society of Exploration Geophysicists, pp. 3210–3214.

Carcione, J. M., Landrø, M., Gangi, A. F., Cavallini, F., 2007. Determining the dilation factor in 4d monitoring of compacting reservoirs by rock-physics models. Geophysical Prospecting 55 (6), 793–804.

Davis, R. O., Selvadurai, A. P., 2005. Plasticity and geomechanics. Cambridge University Press.

Engstrøm, F., 1992. Rock mechanical properties of danish north sea chalk.

Fjær, E., Holt, R. M., Raaen, A., Risnes, R., Horsrud, P., 2008. Petroleum related rock mechanics. Vol. 53. Elsevier.

Garcia, A., MacBeth, C., 2013. An estimation method for effective stress changes in a reservoir from 4d seismics data. Geophysical Prospecting 61 (4), 803–816.

Geertsma, J., 1973. A basic theory of subsidence due to reservoir compaction: the homogeneous case. Verhandelingen Kon. Ned. Geol. Mijnbouwk. Gen 28, 43–62.

Guilbot, J., Smith, B., 2002. 4-d constrained depth conversion for reservoir compaction estimation: Application to ekofisk field. The Leading Edge 21 (3), 302–308.

Hatchell, P., Bourne, S., 2005. Rocks under strain: Strain-induced time-lapse time shifts are observed for depleting reservoirs. The Leading Edge 24 (12), 1222–1225.

Havmøller, O., Foged, N., 1996. Review of rock mechanics data for chalk–. In: Proc. 5th North Sea Chalk Symposium, Reims, France. pp. 7–9.

Hawkins, K., 2008. Defining the extent of the compacting elgin reservoir by measuring stress-induced anisotropy. First Break 26 (10).

Hermansen, H., Thomas, L., Sylte, J., Aasboe, B., et al., 1997. Twenty five years of ekofisk reservoir management. In: SPE Annual Technical Conference and Exhibition. Society of Petroleum Engineers.

Holt, R., Bauer, A., Bakk, A., Szewczyk, D., 2016. Stress-path dependence of ultrasonic and seismic velocities in shale. In: SEG Technical Program Expanded Abstracts 2016. Society of Exploration Geophysicists, pp. 3159–3163.

Holt, R., Fjær, E., Nes, O.-M., Stenebraten, J., et al., 2008. Strain sensitivity of wave velocities in sediments and sedimentary rocks. In: The 42nd US Rock Mechanics Symposium (USRMS). American Rock Mechanics Association.

Holt, R., Kolstø, M., Stenebråten, J., Sønstebø, E., 2009. Use of compacted claystone to understand in-situ stress sensitivity of overburden shales. In: 71st EAGE Conference and Exhibition incorporating SPE EUROPEC 2009.

Holt, R. M., Nes, O.-M., Fjaer, E., 2005. In-situ stress dependence of wave velocities in reservoir and overburden rocks. The Leading Edge 24 (12), 1268–1274.

Janssen, A. L., Smith, B. A., Byerley, G. W., et al., 2006. Measuring velocity sensitivity to production-induced strain at the ekofisk field using time-lapse time-shifts and compaction logs. In: 2006 SEG Annual Meeting. Society of Exploration Geophysicists.

Kenter, C., Van den Beukel, A., Hatchell, A., Maron, P., Molenaar, K., Molenaar, M., Stammeijer, J., et al., 2004. Geomechanics and 4d: Evaluation of reservoir characteristics from timeshifts in the overburden. In: Gulf Rocks 2004, the 6th North America Rock Mechanics Symposium (NARMS). American Rock Mechanics Association.

Kommedal, J. H., Barkved, O. I., Howe, D. J., et al., 2004. Initial experience operating a permanent 4c seabed array for reservoir monitoring at valhall. In: 2004 SEG Annual Meeting. Society of Exploration Geophysicists.

Landrø, M., 2010. Anvendt Geofysikk. NTNU.

Landrø, M., Solheim, O. A., Hilde, E., Ekren, B. O., Strønen, L. K., 1999. The gullfaks 4d seismic study. Petroleum Geoscience 5 (3), 213–226.

Landrø, M., Stammeijer, J., 2004. Quantitative estimation of compaction and velocity changes using 4d impedance and traveltime changes. Geophysics 69 (4), 949–957.

Landrø, M., Strønen, L., 2003. 4d study of fluid effects on seismic data in the gullfaks field, north sea. Geofluids 3 (4), 233–244.

Lo, T.-w., Coyner, K. B., Toksöz, M. N., 1986. Experimental determination of elastic anisotropy of berea sandstone, chicopee shale, and chelmsford granite. Geophysics 51 (1), 164–171.

Mahi, A., 2003. Stress path of depleting reservoirs. Ph.D. thesis, MSc Thesis, NTNU (Norwegian University of Science and Technology).

Mes, M. J., Gustavsen, K., Landau, H., Luttenberger, C., 1995. Ekofisk automatic gps subsidence measurements. In: OCEANS'95. MTS/IEEE. Challenges of Our Changing Global Environment. Conference Proceedings. Vol. 1. IEEE, pp. 178–186.

Mulders, F. M. M., 2003. Modelling of stress development and fault slip in and around a producing gas reservoir. Ph.D. thesis, TU Delft, Delft University of Technology.

Nagel, N. B., 1998. Ekofisk field overburden modelling. In: SPE/ISRE Eurock '98, Trondheim. Society of Petroleum Engineers.

Olsen, C., Christensen, H. F., Fabricius, I. L., 2008. Static and dynamic youngs moduli of chalk from the north sea. Geophysics 73 (2), E41–E50.

Rider, M. H., 1986. The geological interpretation of well logs.

Røste, T., Dybvik, O. P., Søreide, O. K., 2015. Overburden 4d time shifts induced by reservoir compaction at snorre field. The Leading Edge 34 (11), 1366–1374.

Røste, T., Ke, G., 2017. Overburden 4d time shifts indicating undrained areas and fault transmissibility in the reservoir. The Leading Edge 36 (5), 423–430.

Røste, T., Stovas, A., Landro, M., 2005. Estimation of layer thickness and velocity changes using 4d prestack seismic data: 67th annual conference and exhibition, eage. In: Extended Abstracts C. Vol. 10.

Schwall, G., Denney, C., et al., 1994. Subsidence induced casing deformation mechanisms in the ekofisk field. In: Rock Mechanics in Petroleum Engineering. Society of Petroleum Engineers.

Soltanzadeh, H., Hawkes, C., McLellan, P., Smith, S., 2009. Poroelastic modelling of production and injection-induced stress changes in a pinnacle reef. Proceedings of the RockEng09: rock engineering in difficult condition, 1–12.

Sulak, R., et al., 1991. Ekofisk field: the first 20 years. Journal of Petroleum Technology 43 (10), 1–265.

Teufel, L. W., Warpinski, N. R., 1990. Laboratory determination of effective stress laws for deformation and permeability of chalk. Tech. rep., Sandia National Labs., Albuquerque, NM (USA).

Wang, F., Li, X., Couples, G., Shi, J., Zhang, J., Tepinhi, Y., Wu, L., 2015. Stress arching effect on stress sensitivity of permeability and gas well production in sulige gas field. Journal of Petroleum Science and Engineering 125, 234–246.

Wang, Z., 2001. Fundamentals of seismic rock physics. Geophysics 66 (2), 398–412.

Appendix A

Appendix

A.1 Poroelasticity

A brief introduction to poroelasticity is necessary in order to recognize the importance of understanding stress in the overburden when interpreting 4D seismic. This introduction is based on the theory of Maurice A. Biot presented in (Fjær et al., 2008) and is here limited to a porous medium that is isotropic and homogeneous, henceforth fulfilling the Gassmann limit. Many of the equations are established trough lab experiments with two components; fluid and solid framework. In drained experiments, where the fluid is allowed to escape, the following stress-strain relation is established:

$$\sigma_p = K_{fr}\varepsilon_{vol} \tag{A.1}$$

Where K_{fr} is the bulk modulus of the framework, σ_p is the total external stress and ε_{vol} is the volumetric strain. However, in the overburden the pore fluid is shut in, therefore an undrained experiment is more accurate in demonstrating this situation. A change in external stress, compression or expansion, will lead to variation in pore pressure, p_f. The stress-strain correlation is now expressed as:

$$\sigma_p - \frac{C}{M}p_f = K_{fr}\epsilon_{vol} \tag{A.2}$$

Here C and M are elastic moduli. Hence, by introducing α as the Biot coefficient depending on the bulk modulus of the solid framework and bulk modulus of the fluid, the effective stress

is defined as:

$$\sigma'_p = \sigma_p - \alpha p_f \tag{A.3}$$

Thus, the strain or deformation is proportional to the effective stress and not the total stress. This is an important concept to grasp since the R factor is a function of strain and velocity change. However, it should be noted that pore pressure depletion of a reservoir leads to changes in both total stress and effective stress in the overburden, (Fjær et al., 2008). The parameter α is called the Biot coefficient and is defined as:

$$\alpha = \frac{C}{M} = 1 - \frac{K_{fr}}{K_s} \tag{A.4}$$

If $\alpha = 1, \sigma'_p$ is usually referred to as net stress. While in the case of $\alpha \leq 1, \sigma'_p$ is called differential or effective stress. For the overburden of Ekofisk $\alpha \approx 0.8$ has by lab experiments proven to be the best fit, therefore the term effective stress will be used throughout this report.

A.2 Lithology from Gamma Ray Log

From studying strain and velocity in different rocks it is apparent that the R factor will vary depending on lithology. It is perhaps possible that based on lithology one can get an idea if the R factor should be very small or really large, or at least a realistic interval. However, the differences in R values might be so small that it is impossible to distinguish it based on seismic data. Moreover, the formations can be too thin to capture the seismic signature. The absolute value of the R factor might be more dominated by the magnitude of the induced stress changes, than the lithology. To indicate lithology in the overburden one can estimate the volume of clay based on well logs, (Rider, 1986);

$$V_{Clay} = \frac{GR_{log} - GR_{min}}{GR_{max} - GR_{min}} \tag{A.5}$$

GR_{log} is the value of the gamma ray log at each specific depth, while GR_{min} and GR_{max} are the minimum and maximum values of the gamma ray log, respectively. The two latter parameters are individual for each well.

A.3 Effective Stress in the Overburden of the Ekofisk Field

In Figure A.1 the red curve is the averaged smoothed effective stress curve. The effective stress is from ConocoPhillips' model of reservoir and overburden, based on well measurements, well logs and geomechanical modelling. The stress is extracted along wells 2/4-2, 2/4-3, 2/4-4 and 2/4-5 to further be averaged and smoothed in MATLAB. From the plot it is observed that approximately the shallowest 800 m is modeled and shows a "normal" hydrostatic trend where 10 MPa is found at approximately 1000 m burial. Effective stress decreases and increases from 700 m to around 1300 m, where it sinks drastically and stays low until around 2400 m. The interval of critically sinking effective stress is recognized as an overpressured zone, meaning a zone where the pore pressure is extremely high, referring to equation A.3. From 2400 m until top of the reservoir, at around 2985 m, the stress gradient with depth is similar as for the hydrostatic section in the shallowest overburden. Overall, the effective stress is low.

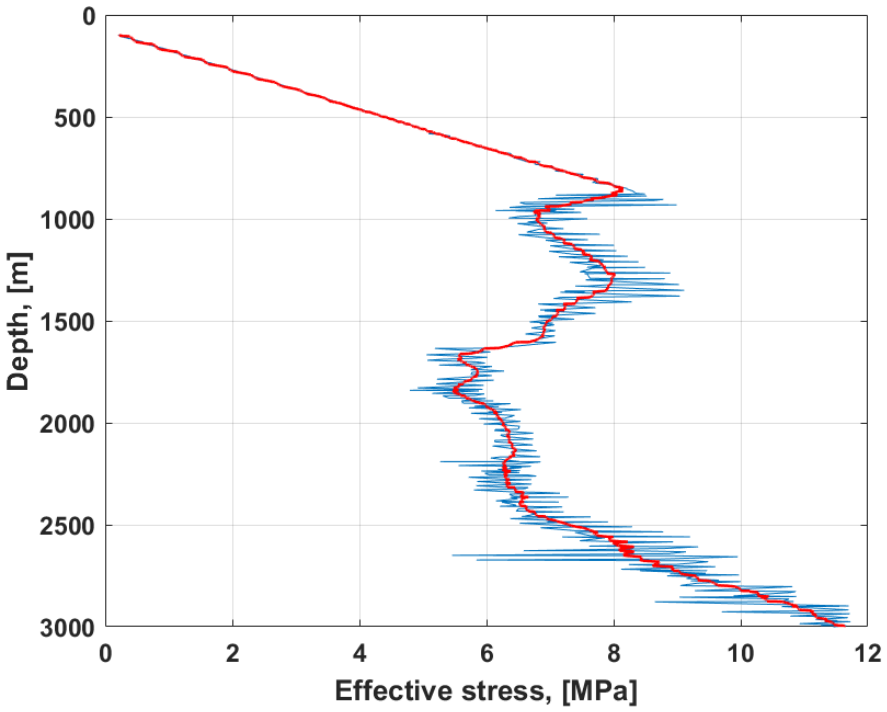

Figure A.1: Effective stress trend in the overburden of the Ekofisk Field.

A.4 Depth-Dependent R Factor for Model 2 using Geertsma's Nucleus of Strain Model

A.4.1 Description of Model 2

Model 2 consists of three bordering reservoirs. Figure A.2 shows the displacement field surrounding the reservoirs. r_1, r_2 and r_3 is the radius of each the deformation fields, and;

$$r_1 = r_2 = r_3 \tag{A.6}$$

The reservoirs are all placed next to each other and are in contact at the reservoir boundary. The superposition principle sketched in Figure A.2 is simulating the system at the Ekofisk Field demonstrated in Figure A.3. Here, R_1 consists of the majority of the field, including the crest, and accounts for the greater part of the subsidence bowl. R_2 represents the depletion zone and R_3 is a small injection zone bordering the depletion zone. Table A.1 shows the reservoir radius used for the three reservoirs in the Geertsma modelling. Consequently, the pore pressure change in reservoir 1, Δp_{f1}, needs to be representative of the area marked by R_1 in Figure A.3, which is the majority of the field.

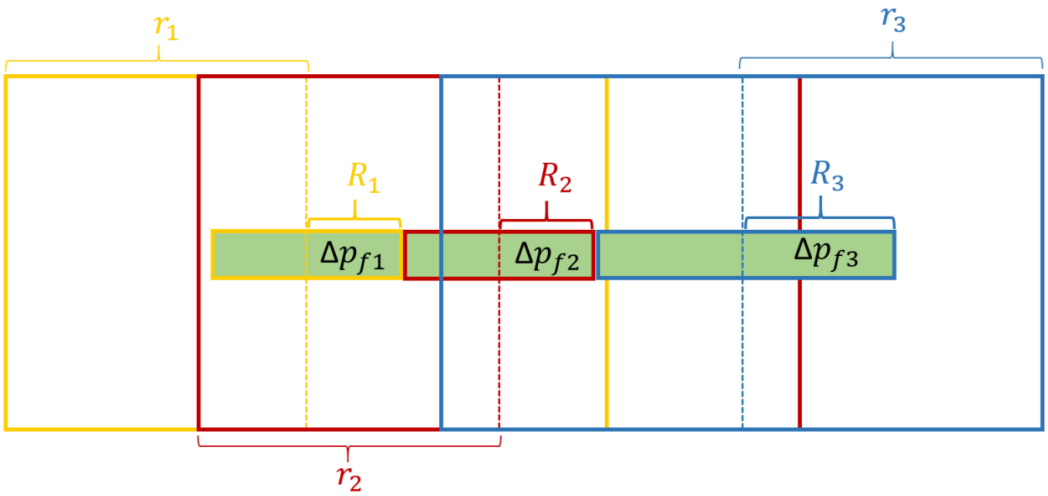

Figure A.2: Sketch of the displacement field from superposition in model 2 for the three reservoirs.

Table A.1: Radius and pore pressure change in the simulations of the three reservoirs in model 2 using Geertsma's nucleus of strain model.

Reservoir	Radius, [m]	Pore pressure, [Mpa]
1	2600	2
2	300	5
3	300	-0.5

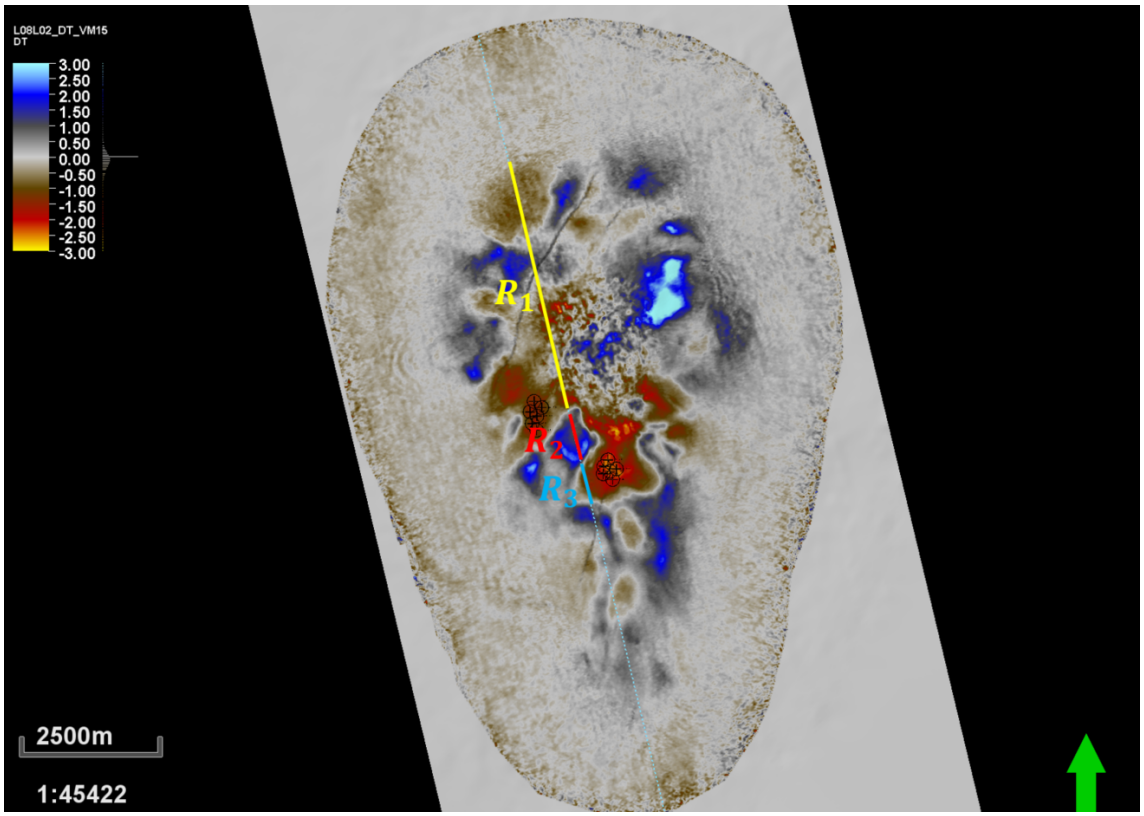

Figure A.3: Radii of three reservoirs during superposition in model 2.

A.4.2 Displacement and Strain

The reservoir radius and pore pressure change for model 2 is shown in Table A.1. The pore pressure increase in the injection zone is only 0.5 MPa in the simulation, which is a result of the discussion above on how gravity is not taken into account, therefore the displacement field would be unrealistic with a larger pore pressure change. The displacement field surrounding the reservoirs in the overburden, sideburden and underburden is shown in Figure A.4. A close-up of the displacement field is shown in Figure A.5 of the overburden and sideburden. The colormap scale is different for the figures. The reservoir center is at 3150 m, from equation 4.2. The

vertical scale is measured is in meter TVDSS. The horizontal scale is in meter, where 0 is a set point at the left side.

In Figure A.4 the displacement geometry below and above the three reservoirs become evident. The contour lines are densely packed, so the reservoir appears to be marked in black. From Figure A.5 the details of the displacement in the overburden is given in more details, including sketches of the reservoirs. The dotted black lines above the reservoirs marked 1 and 2 represents the path were displacement and strain was extracted, which can be seen in Figure A.6.

The displacement field from model 2, Figure A.5, has a larger displacement above reservoir 1 than from model 1, Figure 5.15. This is caused by applying a larger pore pressure change in reservoir 1 in model 2 than in model 1. The pore pressure applied in model 1 is believed to be more representative of the overall pore pressure depletion at Ekofisk in the period 2011 to 2014. Consequently, the compaction at top reservoir above reservoir 1 is also different for the two models. Despite this, the displacement above reservoir 2, which represents the depletion zone, is comparable between the two models.

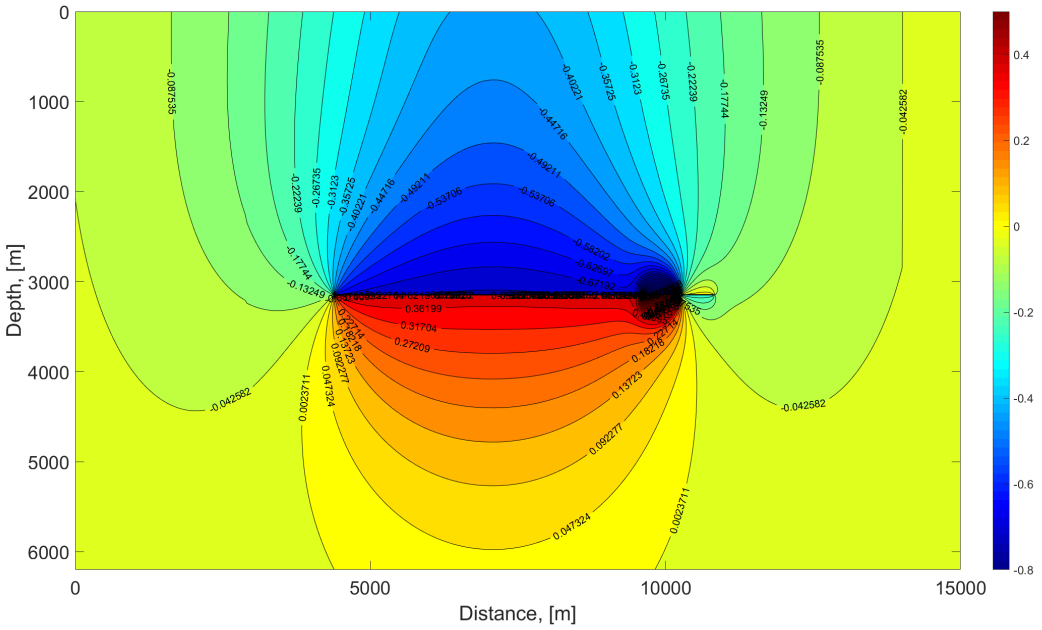

Figure A.4: Displacement field from model 2, limit of the y axis is at 6200 m. The contour labels are in the unit meter.

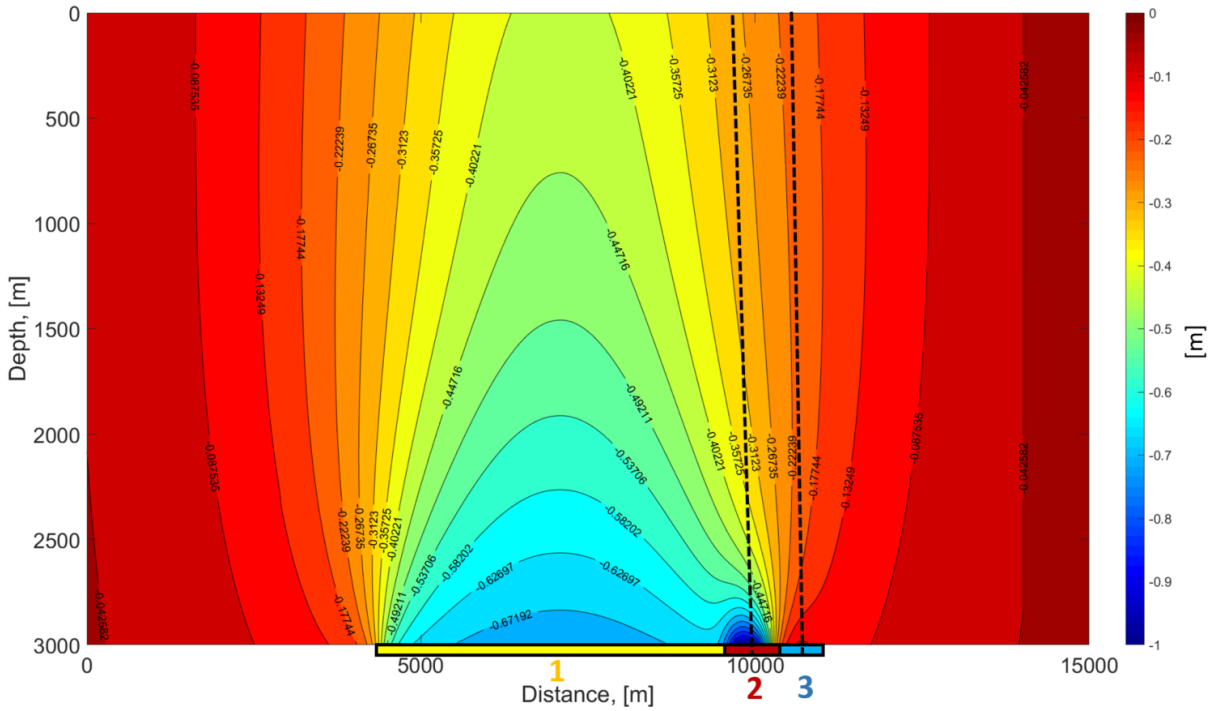

Figure A.5: Displacement field from model 2, limit of the y axis is at 3150 m. The reservoirs from model 2 sketched in Figure A.2 are marked. The contour labels are in meter.

The displacement and strain is extracted along the center-line of reservoir 2, marked as a dotted black line on the figure above. Reservoir 2 is depleting with a large pore pressure change. The plots are displayed in Figure A.6. The displacement at 0 depth represents the subsidence of the sea floor, which is approximately -0.28 m in Figure A.6a. The displacement at 3000 m represents the compaction at top reservoir, which is around -0.97 m for this model. The displacement and strain along the center-line of reservoir 3 is presented in Figure A.7.

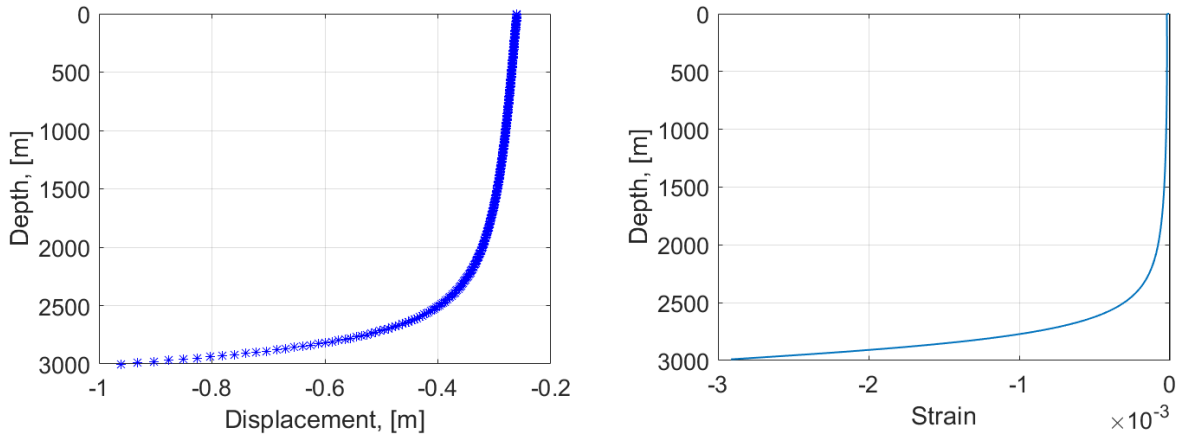

(a) Displacement above the center of reservoir 2. **(b)** Strain above the center of reservoir 2.

Figure A.6: Displacement and strain above the center of reservoir 2

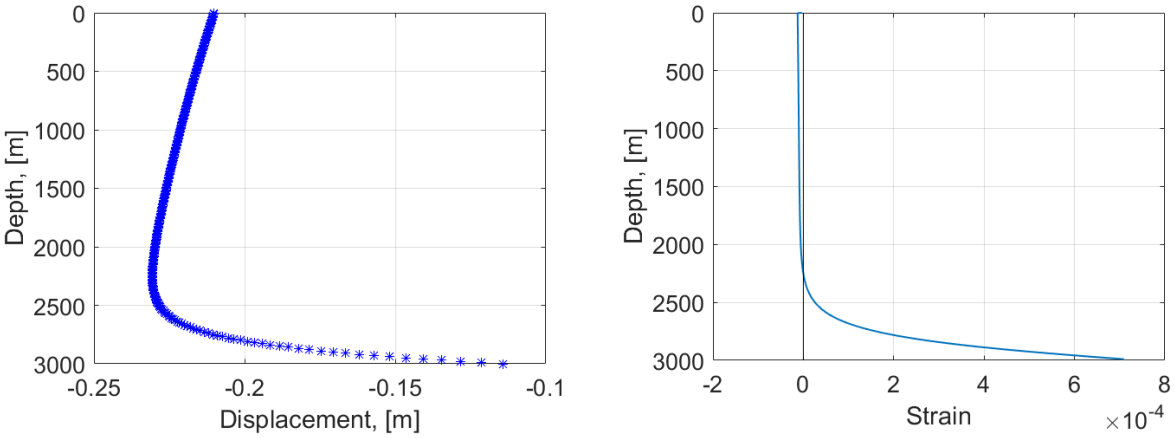

(a) Displacement above the center of reservoir 3. **(b)** Strain above the center of reservoir 2

Figure A.7: Displacement and strain above the center of reservoir 3.

Estimated strain above reservoir 2 and 3 from model 1 and 2 are demonstrated in Figure A.8. It is clear that the strain is most similar above reservoir 2 for the models.

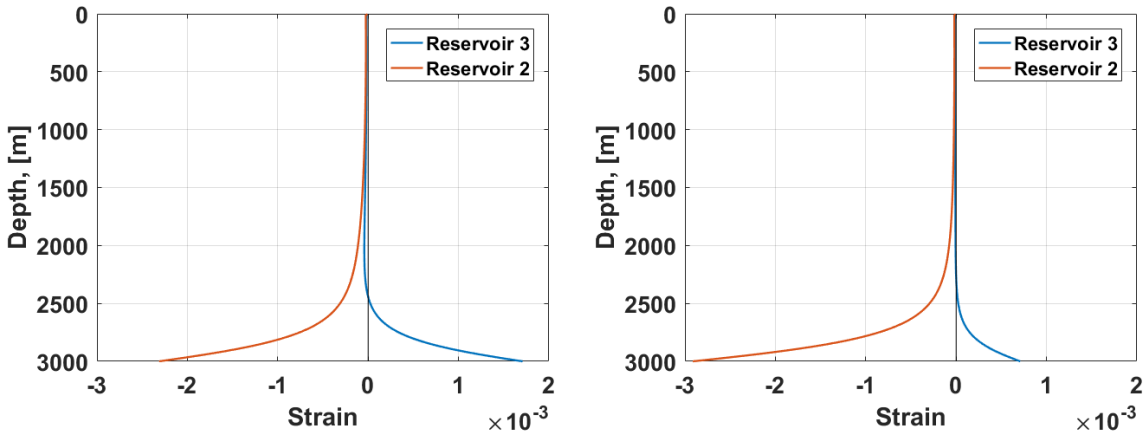

(a) Strain from model 1. **(b)** Strain from model 2.

Figure A.8: Strain from model 1 and model 2 above depletion zones and injection zones.

A.4.3 Synthetic Time Shifts and Depth-Dependent R Factor

Figure A.9 below presents the time shift calculated from the strain using model 2 above a depleting reservoir, Figure A.6b. R values from 1 to 20 are tested. The resulting time shift and R factors are similar to the values observed for model 2. For the time shift in each interval; small R values match the observed time shift close to the reservoir, while larger R factors are observed shallower. For the cumulative time shift, the best fit for the time shift at top reservoir is from $R = 2$. The black line in the plots is the observed 4D data. Figure A.10 shows the

estimated synthetic time shifts for reservoir 3. From the observed time shifts (marked in red and black in the plot) it is clear that there is a poor correlation between observed and synthetic time shifts. Figure A.11 is the depth-dependent R above the depletion zone.

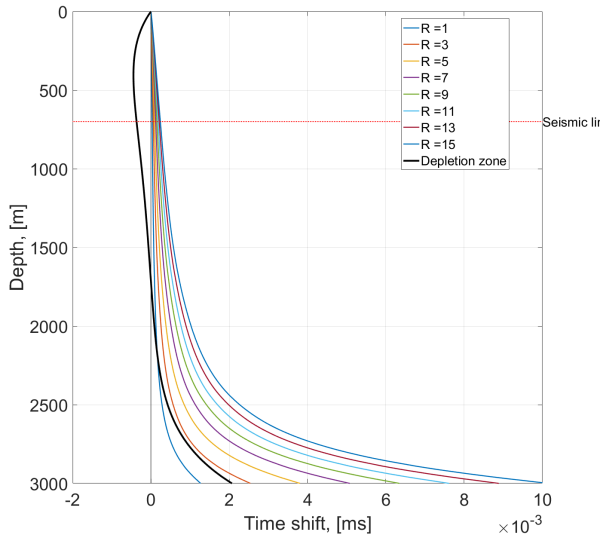

(a) Synthetic time shift in each interval, from strain in Figure A.6b. The black line is the observed time shift in each interval in the depletion zone.

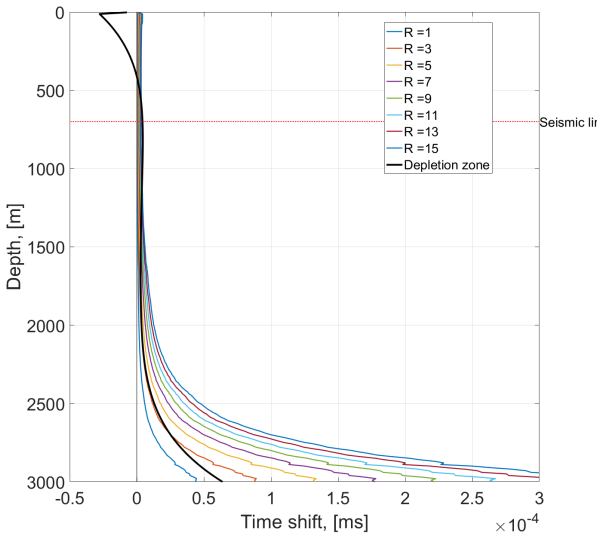

(b) Cumulative synthetic time shift, from strain in Figure A.6b. Black line is the observed time shift in the injection zone.

Figure A.9: Synthetic time shifts for each interval and cumulative time shift using model 2

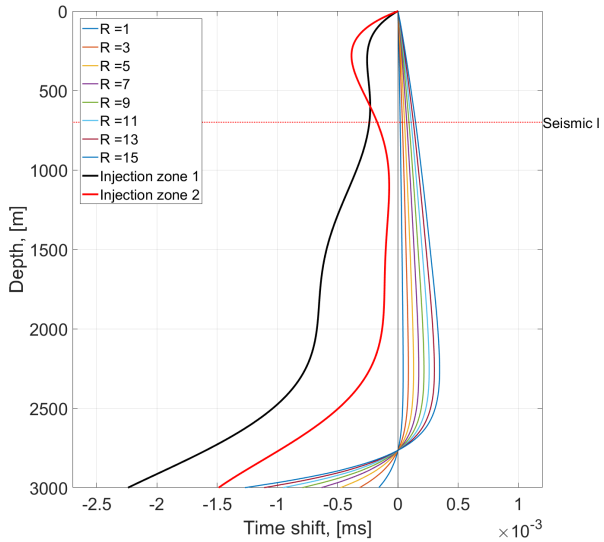

(a) Synthetic time shift in each interval, from strain in Figure A.6b. The black line is the observed time shift in each interval in the depletion zone.

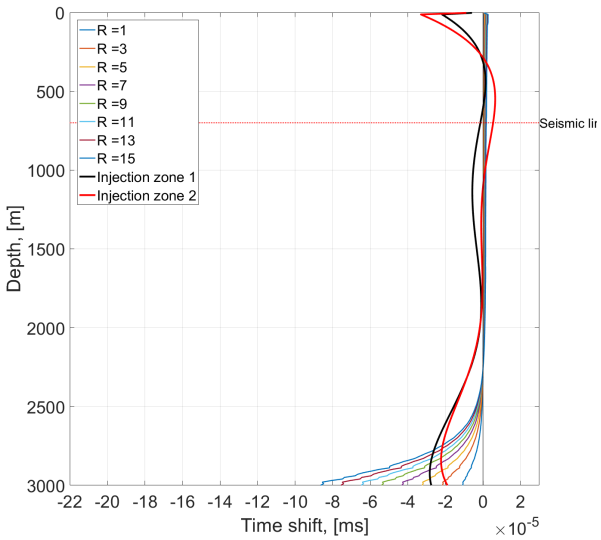

(b) Cumulative synthetic time shift, from strain in Figure A.6b. Black line is the observed time shift in the injection zone.

Figure A.10: Synthetic time shifts for each interval and cumulative time shift using model 2

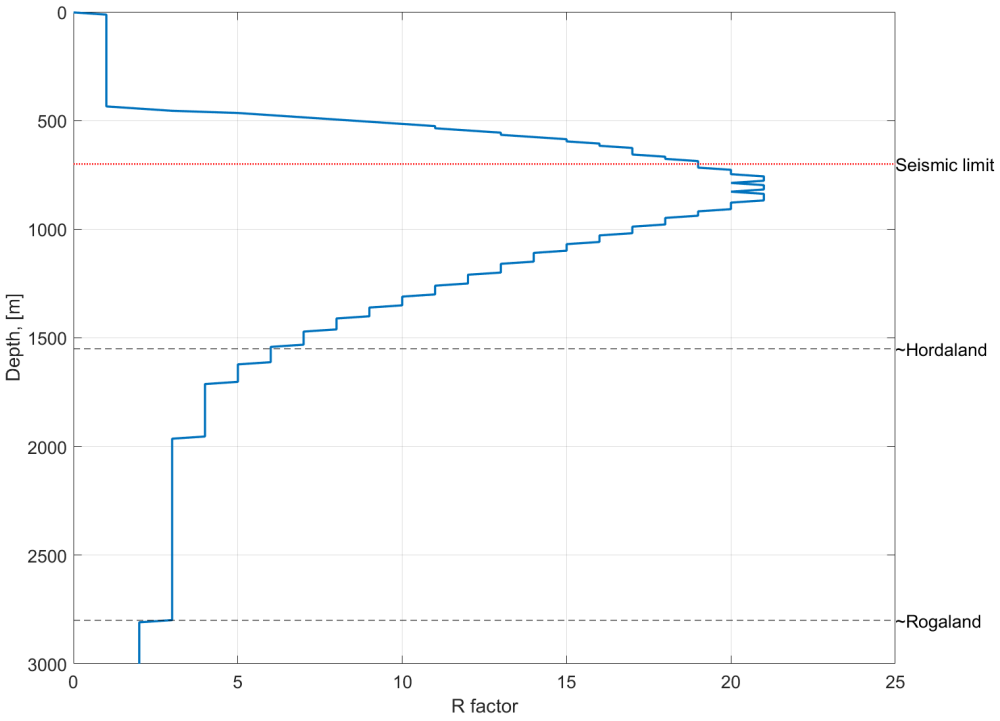

Figure A.11: Depth-dependent R above the dpeltion zone from model 2.

A.5 Quality Checking the Subsidence

GPS data from the center of the Ekofisk field below the hotel platform is studied in order to quality check the subsidence from the 2014 bathymetry data. Figure A.12 shows the subsidence of the sea floor at region 20 and region 14. Region 20 is where the depletion zone is located, while region 14 is in the center of the field. The sea floor measurement from 1986 is here used as base when estimating the subsidence as the first bathymetry was measured this year. Subsidence data for region 20 is only known from bathymetry data, which is rather sparse, while the GPS measures subsidence approximately once a month. The difference in subsidence for region 20 and 14 is demonstrated in the lowermost plot. From year 2000 until 2014 the difference in subsidence at region 14 and 20 has kept rather constant at 1 m. From the GPS data there are no indications that the bathymetry subsidence map between 2011 and 2014 is not reasonable, given that the difference between subsidence in region 14 and 20 in 2014 does not stand out. Hence, the estimated subsidence in Table 5.2 will be used further.

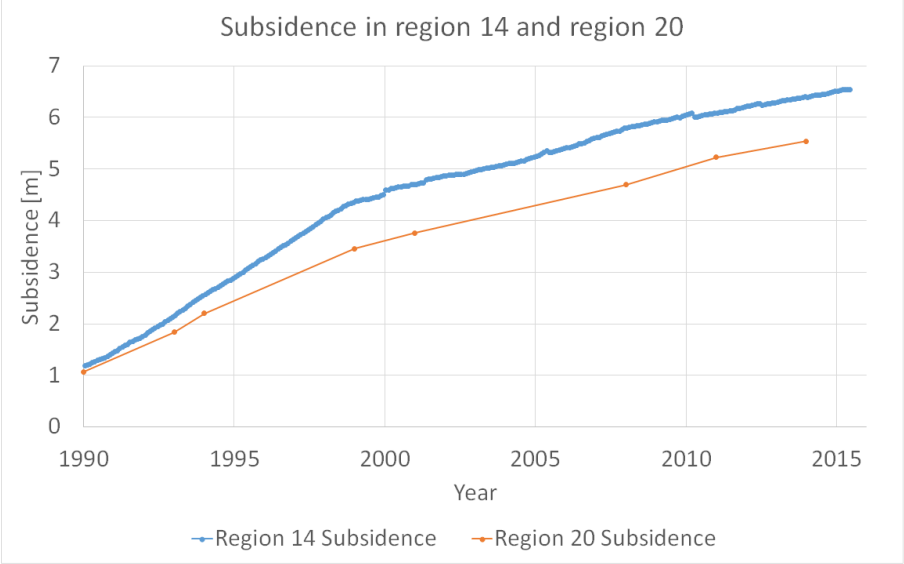

Figure A.12: Plot of measured subsidence in region 14 and region 20.

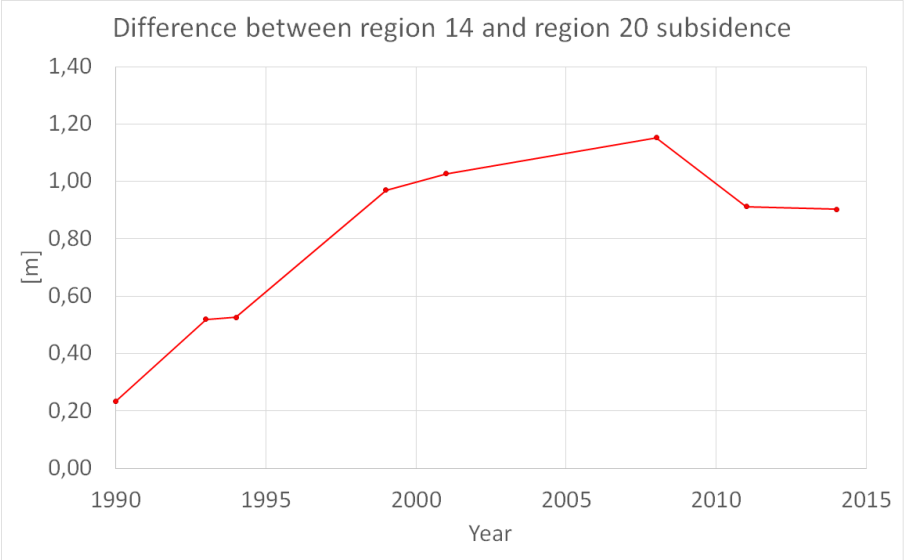

Figure A.13: Plot of difference in subsidence between region 14 and region 20.

A.6 Constant R Factor from Thickness Consideration

Figure A.14 displays the thickness change from equation 3.11 for different R factor values between 1 and 10. From Figure A.14 it is clear which R factor gives a total thickness change like the expected value in the injection zones.

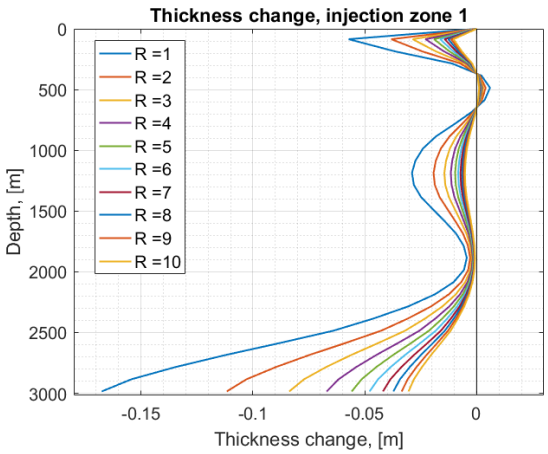

(a) Thickness change in injection zone 1

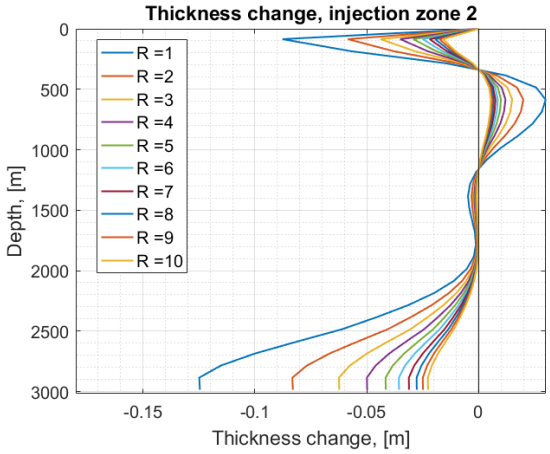

(b) Thickness change in injection zone 2

Figure A.14: Thickness change above injection zone 1 and injection zone 2 for different R factors with the relative time shift curve as input

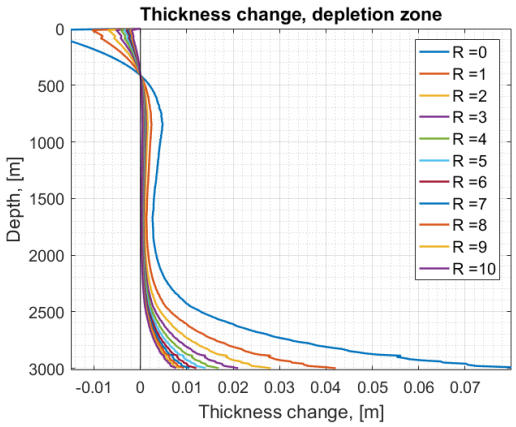

(a) Thickness change in injection zone 1

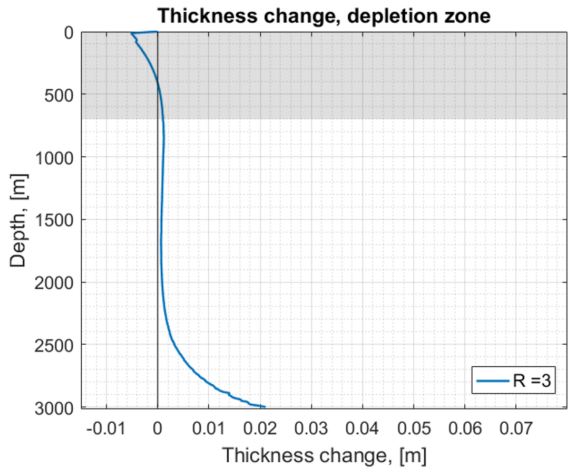

(b) Thickness change in injection zone 2

Figure A.15: Thickness change above the depletion zone. $R = 3$ was the best fit to the modelled total thickness change. Grey zone marks where 4D seismic is not trusted and where thickness change is not included in the calculation.

A.7 Analysis of Core Cata from Ekofisk Overburden

Two cores from the overburden of Ekofisk have been acquired by ConocoPhillips and analysed by SINTEF Petroleum AS, Formation Physics Laboratory. Shale 1 was cored in September 2007 at 1649.9 m TVDBSF, it is from the upper Miocene period and belongs to the Nordland lithological group. It is characterized by porosity between 39-41 %, low quartz content and with clay content around 50 % dominated by smectite. The core referred to as shale 2 was cored in

October 2011 at 1738 m TVDBSF. This is a late Miocene field shale core from the Hordaland lithological group, characterized by porosity around 34 % and significant content of smectite and illite (45 % - 51 %).

By a triaxial-loading step the sample is brought to in situ stress. In situ stress path simulations (ISSP) are supposed to mimic two different stress paths. The ISSP sequence is divided into three undrained segments; ISSP 1, ISSP 2 AND 122P 3, which are performed both fast and slow for shale 2:

- ISSP 1: axial stress decrease, radial stress increase
- ISSP 2: axial stress increase, radial stress decrease back to original in situ stress level
- ISSP 3: axial stress increase, radial stress decrease

Some of the main objectives of these core analysis were improved characterization and modelling of overburden rocks, as well as improved 4D seismic interpretation by accounting accounting for depletion-induced stress changes in the reservoir affecting overburden. By a triaxial-loading step the sample is brought to in situ stress. Stress paths are based on generic geomechanical simulations (Geertsma, 1973) and may differ depending on the geometry of the depleting zone and on the elastic properties between reservoir and its surroundings.

As presented earlier; the assumptions behind Geertsma's simulations are linearly elastic and isotropic rock, indicating that conditions in the overburden are close to constant mean stress or constant volume (Fjær et al., 2008). The stress paths were chosen guided by a simplified model derived from finite element modelling (Mahi, 2003).

A.8 Evaluation of Velocity and Thickness Change Influence on Time Shift

In order to understand whether the time shifts found for the overburden will be influenced mostly by strain or velocity changes, the additional traveltime caused by the thickness change is estimated from equation 3.2. Δz is the total stretch of the overburden and v_p is the average velocity of the overburden, which is estimated from sonic logs to be 2000 m/s. The additional traveltime caused by stretching or compaction in each study area is presented in Table A.2. The

percentage of the time shift being caused by thickness change is estimated based on the total time shift at top reservoir. From the table it is clear that the thickness change has been most important in the depletion zone, where it stands for around 32 % of the total time shift. The thickness change is least important in injection zone 1, which here corresponds to the smallest thickness change of the overburden. However, Table A.2 is only a rough estimate intended to give an overall indicator of the influence off thickness change on time shift. From 4D analysis on the Snorre field, the maximum time shift caused by thickness change was estimated to be 10 % from the same approach as applied to calculate Table A.2, (Røste et al., 2015).

Table A.2: Percentage of time shift caused by overburden thickness change.

Study area	**Thickness change, [m]**	**Additional traveltime, [s]**	**Time shift, [s]**	**Time shift caused by thickness change, [%]**
Depletion zone	0.66	0.00066	0.00207	31.9
Injection zone 1	-0.24	-0.00024	-0.00226	10.6
Injection zone 2	-0.29	-0.00029	-0.00148	19.6